High Resolution CMB Physics

Thibaut Louis

Physics Department and Christ Church College, Oxford

A thesis submitted for the degree of Doctor of Philosophy
in the University of Oxford.

Trinity Term 2014

Declaration

I declare that no part of this thesis has been accepted, or is currently being submitted, for any degree or diploma or certificate or any other qualification in this University or elsewhere.

Chapter 2 is based on work presented in Das, Louis, Nolta et al., published 14 April 2014 in the Journal of Cosmology and Astroparticle physics (JCAP): "The Atacama Cosmology Telescope: temperature and gravitational lensing power spectrum measurements from three seasons of data". I led the power spectrum analysis and produced all the results for this Chapter except for: the derived CMB-only power spectrum (2.7.2) led by Jo Dunkley and Erminia Calabrese, the Galactic dust analysis (2.5.1) that I have co-led with Amir Hajian and the null test analysis (2.7.3) which has been co-led with Renée Hlozek.

Chapter 3 is based on work presented in Louis et al., published 8 July 2014 in JCAP: "The Atacama Cosmology Telescope: cross correlation with Planck maps". This works was performed solely by me, with minor edits reflecting comments and suggestions from collaborators and the referee.

Chapter 4 is based on work presented in Louis et al., published 27 August 2013 in the Monthly Notices of the Royal Astronomical Society (MNRAS): "Lensing simulation and power spectrum estimation for high-resolution CMB polarization maps". This work was performed solely by me, with minor edits reflecting comments and suggestions from collaborators and the referee.

Chapter 5 is based on work presented in Naess et al. which is currently under review: "The Atacama Cosmology Telescope: CMB Polarization at $200<\ell<9000$". The power spectrum analysis that is the main scientific result of this chapter was performed solely by me.

Thibaut Louis *(July 2014)*

High Resolution CMB Physics

Thibaut Louis

Christ Church College

Submitted for the Degree of Doctor of Philosophy

Trinity 2014

Abstract

This thesis presents the measurement of the cosmic microwave background (CMB) power spectrum for the Atacama Cosmology Telescope (ACT) experiment and its polarized upgrade, ACTPol. I present the tools that I have developed for constructing unbiased and nearly optimal statistical estimators. I discuss how to separate the cosmological and the astrophysical signal and how to characterize instrumental systematics. The goal of this work is to obtain accurate power spectra measurement that can be used for cosmological parameter estimation.

I first present the analysis of the complete ACT data set. The high resolution of the telescope allows us to recover power spectra to $\ell = 10000$. I report the measurement of the power spectra at 148 GHz and 218 GHz, as well as the cross-frequency spectrum between the two channels. The power spectrum measurement is consistent with the ΛCDM model and a basic foreground model.

I then present the cross correlation of maps from the Atacama Cosmology Telescope with maps from the Planck satellite in two overlapping regions covering 592 square degrees. I find excellent agreement between the two datasets at both frequencies, quantified using the variance of the residuals between the ACT power spectra and the ACT$\times$*Planck* cross-spectra.

The next generation of CMB experiments are focused on measuring its polarization. I present efficient algorithms for CMB lensing simulation and power spectrum estimation for flat-sky CMB polarization maps.

Finally, I discuss the first temperature and polarization power spectra measurement from the ACTPol experiment. They are the first attempt to measure the polarization of the CMB at high resolution.

Acknowledgements

Les vrais remerciements ne peuvent s'écrire que dans sa langue natale, je céderai donc à la tentation d'utiliser le français.

D'abord à Gaël St Antoine, le premier des professeurs. Celui qui a su parler de relativité générale et de dilatation du temps à un gamin un peu paumé. Celui qui a su transmettre sa passion pour la beauté de la physique. Ensuite à Olivier Binder, quelle source de motivation que tous ces kebabs pariés !

Un grand merci au Pr Wax de l'Université de Metz sa confiance et son soutien ont été inestimables. Au BDE et ses étudiants: Tatare, le Roux, Vaness, La Mel, le Gros, Zigon, Simon, Flavien et tant d'autres.

A L'ENS Paris et ses conscrits qu'agressent. Merci à Mussard, à Reys, à Chatoune, à Mesmay, à Benoit, à Iza, à la boun's, à Valon, à Vlib, à la mère Coin-Coin et à tout ceux que j'oublie. Une mention spéciale pour le répondeur téléphonique de Bastien Mussard, et son soutien indéflectible.

Et puis il y a Oxford. Un grand Merci à Henri Tillson pour m'avoir assimilé. A mon colocataire mi-frère mi-sociopathe Richard. A mon compatriote Jean et ses astuces de cuisine. A Tom pour avoir comblé certaines de mes lacunes en géographie. A Shravan, Ed, Kiz, Ruth, Ricarda et Eleanor, pour tout le temps délicieusement perdu. Aux Postdocs du groupe, et particulièrement à Erminia, Graeme et à Sigurd, merci aussi à Rupert. A Danielle et à Phil pour avoir accepté de relire une partie de ce manuscrit, ils iront loin ces petits.

A Pedro pour avoir formé un groupe formidable, et pour sans cesse le redynamiser à coup d'idées originales. A Sudeep, Anze Slosar, Julien Lesgourgues et Lyman Page qui m'ont beaucoup appris.

A Joanna pour son soutien, sa confiance, ses intuitions et toutes nos discussions scientifiques. Quel plaisir ce fut de travailler sous sa direction !

A mes parents pour tout, à mon frère Romain et ma soeur Laure. A mon grand père et ma grand mère pour l'exemple, et à Jean Marc. Au Zinc, ça aurait été salaud de l'oublier, il sera toujours le premier à tout tenter!

Enfin à Amélie, ici, même le français s'essouffle, disons que nous regardons depuis toujours dans la même direction.

Un poète ça sent des pieds !
On lave pas la poésie !
Ça se défenestre ! et ça crie
Aux gens perdus des mots feries
Des mots oui des mots comme le Nouveau Monde
Des mots venus de l'autre côté clé la rive
Des mots tranquilles comme mon chien qui dort
Des mots chargés des lèvres constellées dans le dictionnaire des constellations de mots
Et c'est le Bonnet Noir que nous mettrons sur le vocabulaire
Nous ferons un séminaire, particulier avec des grammairiens particuliers aussi
Et chargés de mettre des perruques aux vieilles pouffiasses Littéromanes
Il importe que le mot amour soit rempli de mystère et non de tabou, de péché, de vertu, de carnaval romain des draps cousus dans le salace
Et dans l'objet de la policière voyance ou voyeurie
Nous mettrons de longs cheveux aux prêtres de la rue pour leur apprendre à s'appeler dès lors monsieur l'abbé Rita Hayworth monsieur l'abbé BB fricoti fricota et nous ferons des prières inversées
Et nous lancerons à la tête des gens des mots
Sans Culotte !
Sans bande à cul !
Sans rien qui puisse jamais remettre en question
La vieille la très vieille et très ancienne et démodée querelle du qu'en diront-ils Et du je fais quand même mes cochoncetés en toute quiétude sous prétexte qu'on m'a béni Que j'ai signé chez monsieur le maire de mes deux mairies
Alors que ces enfants sont tout seuls dans les rues et s'inventent la vraie galaxie de l'amour instantané
Alors que ces enfants dans la rue s'aiment et s'aimeront
Alors que cela est indéniable
Alors que cela est de toute évidence et de toute éternité
Je parle pour dans 10 siècles et je prends date
On peut me mettre en cabane !
On peut me rire au nez ! ça dépend de quel rire...
Je provoque à l'amour ! et à l'insurrection !
Léo Ferré, Le Chien.

Conventions

The following conventions are used in this thesis:

- The space-time metric used to describe the background evolution of the Universe is the FLRW metric, the space-time interval is given by: $ds^2 = -c^2dt^2 + a^2(t)\delta_{ij}dx^i dx^j$. The scale factor evolves following the Friedman equations.

- To include perturbations, we use the perturbed FLRW metric in the Newtonian gauge:

$$ds^2 = -(1+2\psi)c^2dt^2 + a^2(t)(1-2\Phi)\delta_{ij}dx^i dx^j$$

  ψ corresponds to the Newtonian potential and Φ is the spatial curvature perturbation. In a Universe without anisotropic stress, the Einstein equation sets $\Phi = \psi$. To discuss the effect of gravitational waves, we extend this metric to include tensor perturbations.

- The Hubble parameter is defined as $H = \frac{\dot{a}}{a}$, and the conformal time as $\eta = \int_{t_e}^{t} \frac{dt'}{a(t')}$, where t_e is the time at the end of inflation.

- We will denote by $\mathbf{k}$ the three dimensional Fourier wavevector and by $\boldsymbol{\ell}$ the two dimensional Fourier wavevector.

- We work in the context of the ΛCDM model. We take as a baseline a flat Universe with baryons, cold dark matter, cosmological constant, photons and neutrinos, and will discuss extensions to this model.

Contents

List of Figures

Chapter 1

Introduction

Cosmological measurements, in particular the cosmic microwave background (CMB), allow us to place tight constraints on fundamental physics. High energy phenomena which can not be observed in particle accelerators have left traces in its statistical properties. If the recent claim of the gravitational wave detection by the BICEP2 experiment (BICEP2 Collaboration I 2014) is confirmed by other teams, the CMB will become an extremely cheap window on the physics at the 10^{16} GeV energy scale. The statistical properties of primordial gravitational waves might be mapped with exquisite precision in the next 10 years and will restrict dramatically the size of the parameter space for high-energy physics theories. But this is only a specific example of the constraining power of this observable. In the past decade, the measurement of the CMB anisotropies have placed tight constraints on the energy content and geometry of the Universe, leading to a better understanding of its evolution.

The primordial CMB is very well approximated as a two dimensional Gaussian field. Departure from Gaussianity of the primordial CMB, which would have been a powerful tool for inflation model selection, has not been observed yet (Planck Collaboration XXIV 2013). The properties of a Gaussian field are fully encompassed in its two point correlation function. Specifically the quantity of interest is the power spectrum of CMB fluctuations, the Fourier transform of the two-point correlation function. In the linear regime, and with the assumption of homogeneity and isotropy, the different Fourier modes corresponding to different physical scales are uncorrelated, allowing us

to trivially disentangle different physical effects.

In 2007, the Atacama Cosmology Telescope and the South Pole Telescope (Fowler et al. 2010, Shirokoff et al. 2011) started to map the microwave sky at arc minute resolution. The CMB power at small scale is attenuated due to the Silk damping effect but does contain some important cosmological information. As an example, observations of the CMB at high resolution allow us to measure the number of relativistic species in the Universe, a possible variation of the fine structure constant, and the primordial helium fraction (Sievers et al. 2013).

On the smallest scale, the microwave sky is dominated by astrophysical foreground emission (Dunkley et al. 2011), such as dusty and radio extragalactic point sources. While the study of these foregrounds is of interest by itself, they act as a contaminant to the cosmological signal and need to be characterized in order to be subtracted. One way of separating the CMB and the different foreground emissions is to exploit their different frequency spectra. Multi frequency observations are very powerful tools to break the degeneracy between cosmological and astrophysical signals. Another way is to model their contribution to the angular power spectrum, and to constrain this model based on observations of the CMB at high resolution.

The beginning of my DPhil coincided with the first direct detection of the gravitational lensing of the CMB made by the Atacama Cosmology Telescope collaboration (Das et al. 2011b). The bending of the light due to large scale structures in the Universe imprints a distinct statistical signature in the CMB fluctuations. A high precision measurement of the statistical properties of CMB lensing will place a direct constraint on the sum of the neutrino masses (Abazajian et al. 2011). This, in combination with particle physics measurements which are sensitive to the difference in the masses of the different neutrinos flavors, will impact on our understanding of the standard model of particle physics.

It is worth mentioning that while the combination of the CMB and CMB lensing allows us to constrain cosmological parameters by itself, the best measurement requires combining with other cosmological probes, including type Ia supernovae and Baryon Acoustic Oscillations in the galaxy two point correlation function.

In this thesis I will discuss in detail how power spectra can be estimated efficiently and how to

build an unbiased and nearly optimal estimator for realistic data. I will present the power spectrum analysis for the ACT 3-year data set in Chapter 2. There are mild tensions between measurements made by different collaborations; I present a comparison analysis between *Planck* and ACT data in Chapter 3. The new generation of CMB experiments is now targeting the measurement of the polarization of the microwave sky; I present a new analysis pipeline for the ACTPol collaboration (Chapter 4) and the first power spectra analysis for ACTPol in Chapter 5.

In the remainder of this introduction, I will discuss the physics of the CMB temperature and polarization anisotropies. I will also discuss how the CMB secondary anisotropies are generated and the physics of CMB lensing. I will finally report the state of the art of CMB observations and describe the ACT and ACTPol experiments.

1.1 High resolution CMB temperature power spectrum

The present Universe is expanding: when we extrapolate back into the past, we expect a Universe denser and hotter than at present. At some point, the Universe was hot enough for most of the electrons to be ionized and the Compton scattering of the photons with the free electrons drove the two fluids into thermal equilibrium. Photons in thermal equilibrium with matter follow a black body distribution. The subsequent expansion of the Universe can alter this distribution only by the redshifting of the temperature of the radiation. The fact that the Universe should be filled with black body radiation was first realized in the 1940s by George Gamov, Ralph Alpher and Robert Herman. Based on cosmological nucleosynthesis, they predicted its temperature to be of order 5 K. The first measurement of the cosmic microwave background was made by Penzias and Willson in 1965, who reported an antenna temperature of 3.5 ± 1.0 K at 4 GHz (Penzias & Wilson 1965). The isotropy of the signal and its temperature were consistent with the expected cosmological signal. The black body nature of the cosmic microwave background was firmly established by the COBE satellite in the 90s, in the frequency range 60 to 600 GHz, with a temperature of 2.725 ± 0.002K (Mather et al. 1994). COBE also detected small anisotropies in the CMB, of order $\delta T/T \approx 10^{-5}$ (Smoot et al. 1992). The study of these anisotropies has become the main goal of CMB experiments. We will now discuss how these anisotropies have been generated, how they evolved and how to use

their statistical properties to constrain cosmological parameters.

1.1.1 Generation of primordial perturbations

In the current cosmological model, the initial perturbations are thought to be the result of quantum fluctuations of a scalar field. The stress energy tensor of a scalar field can be written:

$$T^{\alpha}_{\beta} = g^{\alpha\nu}\frac{\partial\phi}{\partial x^{\nu}}\frac{\partial\phi}{\partial x^{\beta}} - g^{\alpha}_{\beta}\left[\frac{1}{2}g^{\mu\nu}\frac{\partial\phi}{\partial x^{\nu}}\frac{\partial\phi}{\partial x^{\mu}} + V(\phi)\right]. \tag{1.1}$$

The pressure and energy density of the field are then given by:

$$T^{0}_{0} \equiv \rho = \frac{1}{2}\left(\frac{d\phi(t)}{dt}\right)^{2} + V(\phi) \tag{1.2}$$

$$T^{i}_{i} \equiv P = \frac{1}{2}\left(\frac{d\phi(t)}{dt}\right)^{2} - V(\phi) \tag{1.3}$$

Under certain conditions on its potential, this field can satisfy $\rho + 3P < 0$. Using the Friedman equation: $\ddot{a} = -\frac{4\pi aG}{3}\left(\rho + \frac{3P}{c^2}\right)$ we see that this will give rise to an accelerated expansion of the Universe. The simplest model for inflation is a field slowly rolling down its potential well. The energy density of such a field is nearly constant. When the field reaches its minimum of potential, inflation ends. This period of inflation has been proposed to solve different problems in cosmology, namely: the flatness problem, the horizon problem and the monopole problem (Linde 1982). It is also a natural framework for the generation of the first inhomogeneities. The inflaton field ϕ can be expanded into a homogeneous part and a perturbation $\phi(\mathbf{x}, t) = \phi^{(0)}(t) + \delta\phi(\mathbf{x}, t)$. The time component of the conservation of the stress energy tensor of the perturbations translates into a differential equation on $\delta\phi$ (Dodelson 2003). In Fourier space:

$$\ddot{\delta\phi} + 2\frac{\dot{a}}{a}\dot{\delta\phi} + k^2\delta\phi = 0 \tag{1.4}$$

where $\cdot$ denotes derivative with respect to the conformal time η[1]. This equation can be rewritten as an evolution equation for a set of harmonic oscillators (defining $\tilde{\delta\phi} = a\delta\phi$):

$$\frac{1}{a}\left[\ddot{\tilde{\delta\phi}} + \left(k^2 - \frac{2}{\eta^2}\right)\tilde{\delta\phi}\right] = 0. \tag{1.5}$$

This can then be easily quantized: $\hat{\tilde{\delta\phi}} = v(k,\eta)\hat{a}_{\mathbf{k}} + v^*(k,\eta)\hat{a}^\dagger_{\mathbf{k}}$, with $v(k,\eta) = \frac{e^{-ik\eta}}{\sqrt{2k}}\left[1 - \frac{i}{k\eta}\right]$. The power spectrum of the inflaton fluctuations is defined as the variance of the Fourier modes $\langle\hat{\tilde{\delta\phi}}^\dagger(\mathbf{k},\eta)\hat{\tilde{\delta\phi}}(\mathbf{k}',\eta)\rangle = |v(k,\eta)|^2(2\pi)^3\delta^3(\mathbf{k}-\mathbf{k}') = (2\pi)^3\delta^3(\mathbf{k}-\mathbf{k}')P_{\delta\phi}(k)$. At the end of inflation, all the modes of interest are super-horizon ($k|\eta| \ll 1$) and $P_{\delta\phi}(k) = \frac{H^2}{2k^3}$.

In this computation, we have neglected the effect of scalar metric perturbations. They are coupled to the perturbation in the inflaton field, and become dominant on super horizon scales. The post inflation power spectrum in the metric perturbations[2] can be related to the horizon-crossing spectrum of $\delta\phi$:

$$P_\psi = P_\Phi = \frac{4}{9}\left(\frac{aH}{\dot{\phi}^0}\right)^2 P_{\delta\phi}\Big|_{aH=k}. \tag{1.6}$$

This equation is of great importance: the quantum fluctuations in the scalar field driving inflation leaves an imprint on the scalar perturbation of the metric. These perturbations in the metric are related to the post inflation energy content of the Universe (photons, baryons, neutrinos, dark matter), so a theory of inflation sets up the initial conditions for the evolution of perturbations in the Universe. To conclude we will express the primordial power spectrum as a function of the slow-roll parameters[3] : $\epsilon = \frac{d}{dt}\left(\frac{1}{H}\right)$ and $\delta = \frac{1}{H}\frac{d^2\phi^{(0)}/dt^2}{d\phi^{(0)}/dt}$; these parameters vanish in the limit where ϕ is constant and are small compare to unity if the field is slowly rolling. Using the Friedmann equations for the background, we can express epsilon as $\epsilon = \frac{4\pi G(\dot{\phi^0})^2}{a^2H^2}$ and the power spectrum for

[1]The conformal time during inflation is defined as $\eta = \int_{a_e}^{a}\frac{da}{a^2H} \approx -\frac{1}{Ha}$ given that H is nearly constant during inflation, and that a_e the scale factor at the end of inflation is large, note that the conformal time is defined to be negative during inflation. At the end of inflation $\eta = 0$.

[2]Some authors prefer to parametrize the scalar perturbation with the curvature perturbation $\mathcal{R}$ defined as the perturbation of the spatial curvature radius $R^{(3)}$ on comoving hypersurfaces, it's a useful quantity because it is conserved for super horizon adiabatic perturbations. We rather use the Bardeen potentials in order to avoid unnecessary definition. The relation between the two quantities during radiation domination and matter domination is trivial $\mathcal{R} = (3/2)\Phi^{RD}$, $\mathcal{R} = (5/3)\Phi^{MD}$.

[3]There are many different conventions for the definition of the slow roll parameters, all of them are equivalent.

the scalar metric perturbation becomes:

$$P_\psi(k) = \frac{8\pi G}{9k^3}\frac{H^2}{\epsilon}\bigg|_{aH=k}. \tag{1.7}$$

It is conventional to parametrize the primordial power spectrum as a function of a scalar tilt n_s:

$$k^3 P_\psi(k) = A\left(\frac{k}{k_0}\right)^{n_s-1}, \tag{1.8}$$

where[4] $n_s = 1 + \frac{d}{d\ln(k)}[\ln(H^2) - \ln(\epsilon)]\big|_{aH=k} = 1 - 4\epsilon - 2\delta$. A prediction of single-field slow roll inflation is that n_s should be close to one but not exactly one. The current best constraints on n_s comes from the measurement of the temperature power spectrum of the *Planck* satellite: $n_s = 0.9603 \pm 0.0073$ (Planck Collaboration XVI 2013), a 5σ detection of deviation from scale invariance ($n_s = 1$). For single field models such that the slow roll condition is well satisfied, the previous calculation is accurate. However it is possible to build models in which the slow-roll conditions are only marginally satisfied, and it might be necessary to extend the computation to second order in the slow roll parameters. Going to second order is equivalent to introducing a running of the tilt:

$$k^3 P_\psi(k) = A\left(\frac{k}{k_0}\right)^{n_s-1+(1/2)(dn_s/d\ln k)\ln(k/k_0)}, \tag{1.9}$$

where the primordial power spectrum depart from a simple power law. *Planck* 's 95 % limit on the running of the tilt is $dn_s/d\ln k = -0.0125 \pm 0.018$ (Planck Collaboration XVI 2013), with no significant running detected.

1.1.2 Evolution of perturbations

Inflation generates primordial fluctuations which are the seed of the observed CMB anisotropies. The CMB is observed on a sphere and the anisotropies are a function of the position on this sphere: $\delta T(\hat{n})/\bar{T}$. The analogue on the sphere of the Fourier decomposition on a Euclidian space is given

[4]The interested reader will notice that $\frac{d\ln H}{d\ln k}\big|_{aH=k} = \frac{k}{H}\frac{dH}{d\eta}\frac{d\eta}{dk}\big|_{aH=k}$, with $\dot{H} = -aH^2\epsilon$ and $\frac{d\eta}{dk}\big|_{aH=k} = -\frac{d(Ha)^{-1}}{dk}\big|_{aH=k} = \frac{1}{k^2}$, it can also be shown that $\frac{d\ln\epsilon}{d\ln k}\big|_{aH=k} = -2(\epsilon+\delta)$.

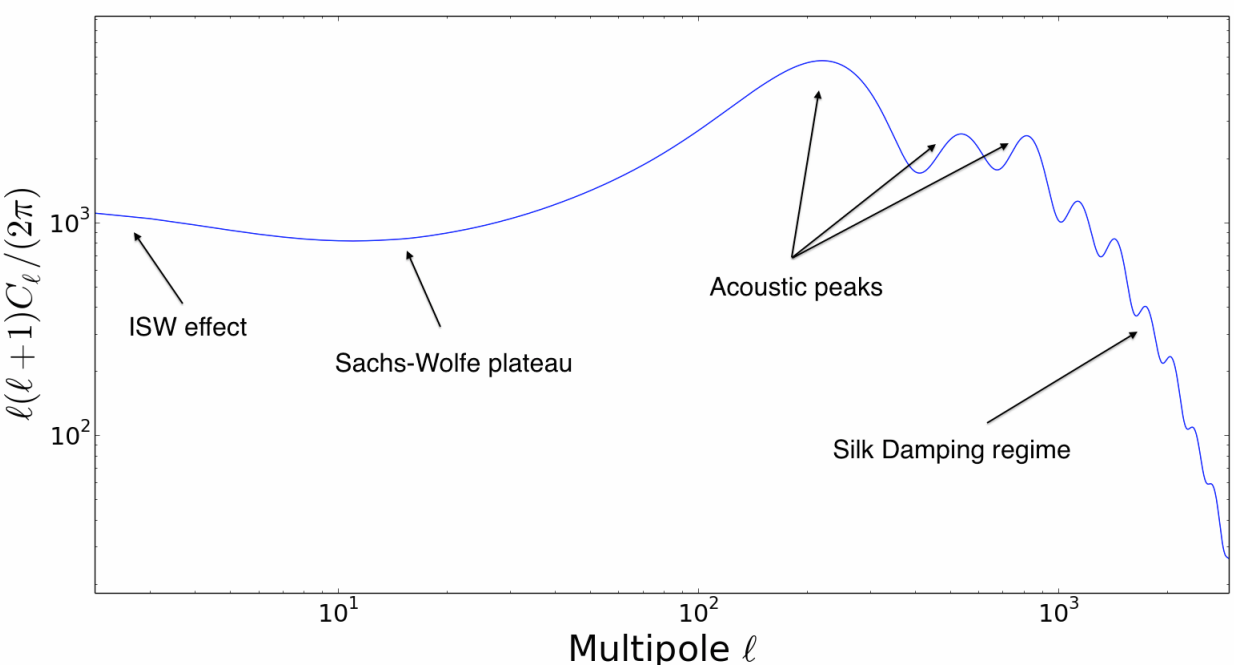

Figure 1.1: The Cosmic Microwave background power spectrum. The multipole ℓ corresponds to the inverse of an angular scale $\ell \approx \pi/\theta$; the different regimes enlightened in the figure are discussed in detail in the text.

by the spherical harmonic decomposition:

$$\delta T(\hat{n})/\bar{T} = \sum_{\ell=0}^{\infty} \sum_{m=-\ell}^{\ell} a_{\ell m} Y_{\ell m}(\hat{n}). \tag{1.10}$$

The CMB anisotropies are well approximated by a Gaussian field, where all statistical information is encoded in its two-point correlation function. In harmonic space, the two point correlation function is given by the variance of the $a_{\ell m}$: $\langle a_{\ell m} a^*_{\ell' m'} \rangle = \delta_{m,m'} \delta_{\ell,\ell'} C_\ell$. The goal of this section is to relate the angular power spectrum of the CMB fluctuations (which can be measured), C_ℓ, to the primordial power spectrum generated by inflation, $P_\psi(k)$.

At the end of inflation, during reheating, the inflaton field decays into the different components observed today in the Universe: baryons, photons, dark matter and neutrinos. We need to describe the evolution of these fluids as they interact together and with the gravitational field. A systematic way to describe their evolution is the Boltzmann equation, an equation of conservation of the phase

space density f of each of the species

$$\frac{df}{dt} = C[f]. \tag{1.11}$$

The physical interpretation of this equation is trivial: the time derivative of the phase space density is equal to a collision term accounting for the interactions of a given fluid with the other components in the Universe. The time derivative here needs to be computed in a fully relativistic context[5] and will depend on the metric perturbation, while the expression for the collision term is specific for the different physical interactions. The phase space density of the photons is given by a perturbed Bose-Einstein distribution:

$$f(\mathbf{x}, p, \hat{p}, t) = \left[\exp\left(\frac{p}{\bar{T}(t)[1+\theta(\mathbf{x},\hat{p},t)]}\right) - 1\right]^{-1}. \tag{1.12}$$

The Boltzmann equation for the photon perturbations translates into an evolution equation for temperature inhomogeneities: $\theta(\mathbf{x},\hat{p},t) = \delta T(\mathbf{x},\hat{p},t)/\bar{T}(t)$. Solving the full set of Boltzmann equations, using the initial conditions set up by inflation, allows us to predict the statistical properties of the CMB anisotropies[6]. In practice the Boltzmann equations are solved numerically using one of the publicly available codes: CMBFAST, CAMB, CLASS (Seljak & Zaldarriaga 1996; Lewis et al. 2000; Lesgourgues 2011); these codes relate the power spectrum of the fluctuations generated by inflation $P_\psi(k)$ to the power spectrum of the CMB fluctuations C_ℓ :

$$C_\ell = (4\pi)^2 \int k^2 dk P_\psi(k) |\Delta_\ell(k, \eta = \eta_0)|^2. \tag{1.13}$$

Here $\Delta_\ell(k, \eta = \eta_0)$ is the transfer function, which can be decomposed into a source term and a geometrical term:

$$\Delta_\ell(k, \eta = \eta_0) = \int_0^{\eta_0} S(k,\eta) j_\ell[k(\eta_0 - \eta)] d\eta. \tag{1.14}$$

[5]For the photons we have $\frac{df}{dt} = \frac{\partial f}{\partial t} + \frac{\partial f}{\partial x^i}\frac{dx^i}{dt} + \frac{\partial f}{\partial p}\frac{dp}{dt} + \frac{\partial f}{\partial \hat{p}^i}\frac{d\hat{p}^i}{dt}$ using the geodesic equation and the fact that the norm of the quadri-impulsion vanishes $g_{\mu\nu}P^\mu P^\nu = 0$ we get at first order in perturbations:
$\frac{df}{dt} = \frac{\partial f}{\partial t} + \frac{\hat{p}^i}{a}\frac{\partial f}{\partial x^i} - p\frac{\partial f}{\partial p}[H + \frac{\partial \Phi}{\partial t} + \frac{\hat{p}^i}{a}\frac{\partial \psi}{\partial x^i}]$.

[6]We also need evolution equations for the gravitational potentials ψ and Φ, given by the Einstein equations.

The source term encodes the physics of the evolution of the temperature inhomogeneities; it is a solution to the Boltzmann equation. The geometrical term project the Fourier modes k into multipoles ℓ.[7]

In the following we will focus on a qualitative discussion of the different physical phenomena that affect the photon perturbations. The goal is to provide an intuition for the expression of the transfer function. The most relevant interactions for CMB physics are Compton scattering of photons with free electrons, and the Coulomb interaction between protons and electrons. The Compton scattering kept photons and electrons in thermal equilibrium and the Coulomb interaction acted as glue between protons and electrons, so that the cosmological plasma was a tightly coupled photon-baryon fluid. As the Universe expanded and cooled down, this process became less efficient, the probability for a photon to collide with a free electron decreased and electrons and protons combined to form neutral hydrogen, an event known as recombination. When the mean free path of a photon became of order the size of the horizon, the Universe went from opaque to transparent and the cosmic microwave background was emitted. We can then distinguish three different regimes in the evolution of the perturbations:

1. In the tight coupled limit, the photon-baryon plasma can be described as a simple fluid: the photon (or temperature) perturbation $\theta(\mathbf{x}, \hat{p}, t)$ can be entirely characterized with only two moments, a monopole $\theta_0(\mathbf{x}, t)$ and a dipole $\theta_1(\mathbf{x}, t)$[8]. All others moments are washed out by the constant interaction with the electrons. The particles of the photon-baryon plasma fell into gravitational potential wells, resulting in a compression of the fluid. The compressing plasma up-scattered photons to higher energies. The increased radiation pressure opposed the compression, resulting in a rarefaction. These two phenomena resulted in temperature oscillations. Physically, the temperature oscillations represent the heating and cooling of a fluid that is compressed and rarefied by acoustic waves (Hu et al. 1996, Hu & Dodelson 2002). The waves froze at recombination, when the photons decoupled with the baryons. The modes that reached their extrema at that time exhibit enhanced temperature fluctuations. The wave

[7] There is no one-to-one relationship between a given multipole ℓ and a Fourier mode k, but the Bessel function $j_\ell[k(\eta_0 - \eta)]$ peaks at $\ell = k(\eta_0 - \eta)$.

[8] This is equivalent to say that a fluid can be characterized by a density field $\rho(\mathbf{x}, t)$ and a velocity field $\mathbf{v}(\mathbf{x}, t)$.

numbers of these extrema are given by: $k_n = \frac{n\pi}{r_s(\eta_*)}$ (n=1, 2, ...), where $r_s(\eta_*) = \int_0^{\eta_*} d\eta' c_s(\eta')$ is the sound horizon at the time of recombination[9]. In harmonic space, this gives rise to a coherent series of acoustic peaks in the anisotropy spectrum, located at $\ell_n = n\ell_p \approx \frac{n\pi(\eta_0 - \eta_*)}{r_s(\eta_*)}$ known as the baryon acoustic oscillations[10].

2. During the recombination epoch, the amount of photon scattering decreased dramatically. The description of the photon-baryon plasma as a fluid is incomplete and we need to account for photon diffusion. A photon traveled a mean distance of $(n_e\sigma_T)^{-1}$ between each scatter. The trajectory of a photon during recombination can be modeled as a random walk. If the random walk takes the photons across a wavelength of the perturbation, then the hot and cold photons mix and average out. This resulted in the damping of the acoustic oscillation on scales smaller than the distance photons travel during recombination. This is known as the Silk damping effect (Silk 1968): the photon perturbations are exponentially damped (θ_0, $\theta_1 \propto \exp\left(-\frac{k^2}{k_D^2}\right)$). Measuring the Silk damping effect was one of the primary goals of high resolution CMB experiments, since the damping scale k_D depends on the recombination history which depends on cosmological parameters (Hu & White 1997b). It also allows us to test extensions of the ΛCDM model. One example is a temporal variation of the fine structure constant $\Gamma = \alpha(t_*)/\alpha(t_0)$. The mean free path of a photon depends on the Thomson scattering cross section which in turn depends on the fine structure constant at the time of recombination $\sigma_T(t_*) \propto \alpha(t_*)^2$. A possible temporal variation of the fine structure constant is disfavored by the ACT damping tail measurement, with $\Gamma = 1.004 \pm 0.005$ (Sievers et al. 2013). The recombination history is also sensitive to the amount of primordial helium: the ionization energy of helium is larger than that of hydrogen and it therefore recombines earlier, lowering the density of free electron in the Universe and increasing the mean free path of the photons. The mass fraction of helium has been constrained by ACT to be $Y_p = 0.225 \pm 0.034$ (Sievers et al. 2013).

[9]The sound speed of the acoustic waves is given by $c_s = \sqrt{\frac{1}{3\left(1+\frac{3\rho_b}{4\rho_\gamma}\right)}}$, the baryons make the fluid heavier, lowering the speed of the acoustic waves.

[10]The extrema of the oscillatory density field correspond to a turnover in the velocity field. The monopole is then out of phase with the dipole, which makes the troughs less accentuated in the CMB power spectrum.

3. After decoupling, the CMB photons traverse the Universe from the last scattering surface to us and have thus interacted with matter along their path through the Universe. One important effect is the gravitational lensing of the CMB, the gravitational deflection of the photons due to the large scale structures of the Universe (see Section 1.1.3). Another contribution to anisotropies is given by the late time integrated Sachs Wolfe (ISW) effect (Sachs & Wolfe 1967). When photons are falling into potential wells they gain energy and the loss of energy to climb out of the potential is equal to the gain if the potential is static. During dark energy domination, potential wells decay and the time variation of the gravitational potential when photons are traveling through them induces an imprint on the photons' statistical properties, enlarging the large scale anisotropies. Finally the thermal and kinematic Sunyaev-Zel'dovich effect (Sunyaev & Zeldovich 1980), the interaction of CMB photons with hot electron gas in galaxy clusters, will be discussed in Section 1.1.4.

The description above is far from being complete, but helps one understand the shape of the CMB power spectrum. Finally we should mention that the size of the causal horizon at recombination is of order a degree (or $\ell \approx 120$) so that when we observe the full sky CMB, we observe many causally disconnected regions. The observed CMB fluctuations are also redshifted due to potential wells on the last scattering surface. This effect dominates so a cold spot on a CMB map actually corresponds to an overdensity and a hot spot to an underdensity.

The modes on scales bigger than the causal horizon at the time of recombination are insensitive to the effect of baryon acoustic oscillations and Silk damping; their statistical structure is unchanged since their generation by inflation. The angular power spectrum of these modes can be computed by simply projecting the inflationary power spectrum in multipole space, resulting in $C_\ell \sim \frac{1}{\ell(\ell+1)}$, this is one of the historical reason for plotting the angular power spectrum as $\ell(\ell+1)C_\ell$. This part of the spectrum that is not affected by causal processes is called the Sachs-Wolfe plateau (Sachs & Wolfe 1967). The power spectrum of the CMB fluctuations is displayed in Fig. 1.1, highlighting the different features discussed above.

1.1.3 Lensing of the Cosmic Microwave Background

In the previous sections, we used the fact that different Fourier modes (or different multipoles) are uncorrelated. This property comes from the assumption that the Universe is statistically homogeneous: the perturbations in one part of the sky share the same statistical properties as the perturbations in another part of the sky. To prove it, let us consider a perturbation $\delta(\mathbf{x})$ and its Fourier transform $\delta(\mathbf{k})$, and compute:

$$\begin{aligned} \langle \delta(\mathbf{k})\delta(\mathbf{k}')^* \rangle &= \int d\mathbf{x} \int d\mathbf{x}' e^{-i(\mathbf{k}.\mathbf{x}-\mathbf{k}'.\mathbf{x}')} \langle \delta(\mathbf{x})\delta(\mathbf{x}') \rangle \\ &= \int d\mathbf{x} \int d\mathbf{x}' e^{-i(\mathbf{k}.\mathbf{x}-\mathbf{k}'.\mathbf{x}')} \xi(\mathbf{x},\mathbf{x}') \end{aligned} \tag{1.15}$$

where $\xi(\mathbf{x},\mathbf{x}') = \langle \delta(\mathbf{x})\delta(\mathbf{x}') \rangle$ is the two-point correlation function of the fluctuation. The homogeneity of the Universe is defined as a translational symmetry, that is, the correlation function can not depends on the specific position of the two points, only on their separation $\xi(\mathbf{x},\mathbf{x}') = \xi(\mathbf{x}-\mathbf{x}') = \xi(\mathbf{r})$. Then

$$\langle \delta(\mathbf{k})\delta(\mathbf{k}')^* \rangle = \int d\mathbf{x} e^{-i(\mathbf{k}-\mathbf{k}').\mathbf{x}} \int d\mathbf{r} e^{-i\mathbf{k}'.\mathbf{r}} \xi(\mathbf{r}) = \delta^3(\mathbf{k}-\mathbf{k}')P(\mathbf{k}'). \tag{1.16}$$

Here we also used the fact that the power spectrum is defined as the Fourier transform of the correlation function. The product is non-zero only if $\mathbf{k} = \mathbf{k}'$, the modes are uncorrelated. The Universe is also assumed to be isotropic, so the correlation function can only depend on the norm of $\mathbf{r}$, $\xi(\mathbf{r}) = \xi(r)$; the power spectrum then only depends on the norm of $\mathbf{k}$. This small introduction is relevant for discussing the gravitational lensing of the cosmic microwave background because, as we will shortly see, one effect of the lensing is to couple different Fourier modes. Measuring the mode-to-mode coupling translates directly into a measurement of the lensing field.

The effect of the weak gravitational lensing of the CMB photons by the large scale structure of the Universe can be described as a remapping of the temperature by a deflection angle $\boldsymbol{\alpha}$ (Lewis & Challinor 2006), $\tilde{T}(\hat{n}) = T(\hat{n} + \boldsymbol{\alpha})$ where $\tilde{T}$ is the lensed temperature field. The deflection angle can be computed by solving the geodesic equation for photons in a perturbed FLRW Universe.

Assuming a flat Universe ($\Omega_k = 0$) we have

$$\boldsymbol{\alpha} = -2\int_0^{\chi_*} d\chi \frac{(\chi_* - \chi)}{\chi_* \chi} \boldsymbol{\nabla}_{\hat{n}} \psi(\chi\hat{n}; \eta_0 - \chi) \tag{1.17}$$

where χ is the comoving distance[11]. We can rewrite the deflection angle as the gradient of the lensing potential, $\boldsymbol{\alpha} = \boldsymbol{\nabla}_{\hat{n}}\Psi$. The lensing potential has a simple physical meaning: along their path from the last scattering surface to us, photons are going to be deflected by the gravitational potential wells and the distance at which the deflection occurs affects the observed deflection angle. The typical size of the deflection angle is a few arcminutes, smaller than a typical CMB fluctuation. We can expand the lensed temperature field in term of the unlensed field and the deflection angle:

$$\begin{aligned} \tilde{T}(\hat{n}) &= T(\hat{n} + \nabla\Psi) \\ &= T(\hat{n}) + \partial^c\Psi\partial_c T(\hat{n}) + \partial^c\Psi\partial^d\Psi\partial_c\partial_d T(\hat{n}) + ... \end{aligned} \tag{1.18}$$

Before starting the discussion on the effect of the lensing in harmonic space, let's introduce a convenient approximation widely used in the rest of this thesis: the flat sky approximation. It has the advantage of simplifying the maths and is valid for high resolution experiments such as ACT and ACTPol. These experiments have only observed a small part of the sky. Instead of decomposing the temperature field in spherical harmonics $T(\hat{n}) = \sum_{\ell,m} a_{\ell m} Y_{\ell m}(\hat{n})$, we will assume that on the region of observation, the effect of the curvature of the sky can be neglected. The temperature field becomes a function on a two-dimensional plane, and can be expanded in Fourier modes $T(\mathbf{x}) = \int T(\boldsymbol{\ell}) e^{i\boldsymbol{\ell}.\mathbf{x}} d\boldsymbol{\ell}$. The Fourier analogue to the Taylor expansion in Eqn. 1.18 is[12]. :

$$\begin{aligned} \tilde{T}(\boldsymbol{\ell}) &= T(\boldsymbol{\ell}) - \int d\boldsymbol{\ell}'\boldsymbol{\ell}'.(\boldsymbol{\ell} - \boldsymbol{\ell}')\Psi(\boldsymbol{\ell} - \boldsymbol{\ell}')T(\boldsymbol{\ell}') \\ &- \frac{1}{2}\int d\boldsymbol{\ell_1}\int d\boldsymbol{\ell_2}\,(\boldsymbol{\ell_1}.[\boldsymbol{\ell_1} + \boldsymbol{\ell_2} - \boldsymbol{\ell}])\,(\boldsymbol{\ell_1}.\boldsymbol{\ell_2})T(\boldsymbol{\ell_1})\Psi(\boldsymbol{\ell_2})\Psi^*(\boldsymbol{\ell_1} + \boldsymbol{\ell_2} - \boldsymbol{\ell}). \end{aligned} \tag{1.19}$$

From this expression we see that the lensed Fourier mode $\tilde{T}(\boldsymbol{\ell})$ gets a contribution from other

[11] $\chi = \eta_0 - \eta$.

[12] Using the convolution theorem and the fact that $\mathcal{F}[\partial_c T] = i\ell_c\mathcal{F}[T]$.

multipoles $\boldsymbol{\ell}'$. At first order in the lensing potential Ψ, we have[13]:

$$\begin{aligned}\langle\tilde{T}(\boldsymbol{\ell})\tilde{T}^*(\boldsymbol{\ell}-\boldsymbol{L})\rangle &= \delta^2(\boldsymbol{L})C_\ell - \int d\boldsymbol{\ell}'\left[\boldsymbol{\ell}'.(\boldsymbol{\ell}-\boldsymbol{\ell}')\Psi(\boldsymbol{\ell}-\boldsymbol{\ell}')\langle T(\boldsymbol{\ell}')T^*(\boldsymbol{\ell}-\boldsymbol{L})\rangle\right. \\ &\qquad \left. + \boldsymbol{\ell}'.(\boldsymbol{\ell}-\boldsymbol{L}-\boldsymbol{\ell}')\Psi(\boldsymbol{\ell}-\boldsymbol{L}-\boldsymbol{\ell}')\langle T(\boldsymbol{\ell})T^*(\boldsymbol{\ell}')\rangle\right] + \mathcal{O}(\Psi^2) \\ &= \delta^2(\boldsymbol{L})C_\ell + \left[\boldsymbol{L}.(\boldsymbol{L}-\boldsymbol{\ell})C_{|\boldsymbol{\ell}-\boldsymbol{L}|} + \boldsymbol{\ell}.\boldsymbol{L}C_{\boldsymbol{\ell}}\right]\Psi(\boldsymbol{L}) + \mathcal{O}(\Psi^2).\end{aligned}$$

The measurement of the lensing field $\Psi(\boldsymbol{L})$ reduces to the measurement of the mode-to-mode coupling of the lensed CMB temperature field. The CMB lensing is sensitive to metric perturbations over a fairly large redshift range, $0.5 \lesssim z \lesssim 5.0$, which are in turn related to matter density[14], so the measurement of the gravitational lensing of the CMB informs us about the growth of structure in the Universe. The ACT experiment has achieved the first detection of the power spectrum of the lensing potential $C_L^\Psi = \langle\Psi(\boldsymbol{L})\Psi^*(\boldsymbol{L})\rangle$ using the measurement of the four-point correlation function of the lensed CMB temperature field[15] (Das et al. 2011b). *Planck* (Planck Collaboration XVII 2013), SPT (van Engelen et al. 2012) and Polarbear (Ade et al. 2013) have now reported similar detections at higher significance. An extension to the standard ΛCDM model which can be measured accurately with the gravitational lensing of the CMB is the sum of the neutrino masses. The small masses of neutrinos makes their thermal velocities non-negligible in the Universe and lead to smearing out of over-dense regions (Abazajian et al. 2011; Lesgourgues & Pastor 2006). The idea is that neutrinos contribute to the background expansion (due to their energy density Ω_ν), but can not cluster below a scale set by their free streaming scale[16]. Matter perturbations on scales larger than the neutrino free streaming scale grows as $\delta \propto a$, but only as $\delta \propto a^{1-f_\nu}$ with $f_\nu \approx 0.08\frac{\sum m_\nu}{1\mathrm{eV}}$ for scales below the free streaming, leading to small scale power suppression in the matter and lensing power spectrum.

The gravitational lensing impacts the power spectrum of the CMB: keeping all the terms of

[13] Remember that the unlensed CMB field satisfy $\langle T(\boldsymbol{\ell})T^*(\boldsymbol{\ell}')\rangle = \delta^2(\boldsymbol{\ell}-\boldsymbol{\ell}')C_\ell$.
[14] The connection between the two is the poisson equation: $-k^2\psi = 4\pi G\rho_m\delta_m$.
[15] Indeed, $\Psi(\boldsymbol{L}) \propto \tilde{T}(\boldsymbol{\ell})\tilde{T}^*(\boldsymbol{\ell}-\boldsymbol{L})$, so $\langle\Psi(\boldsymbol{L})\Psi^*(\boldsymbol{L})\rangle$ is a four point function.
[16] Their velocity is greater than the escape velocity from gravitational potential wells on those scales.

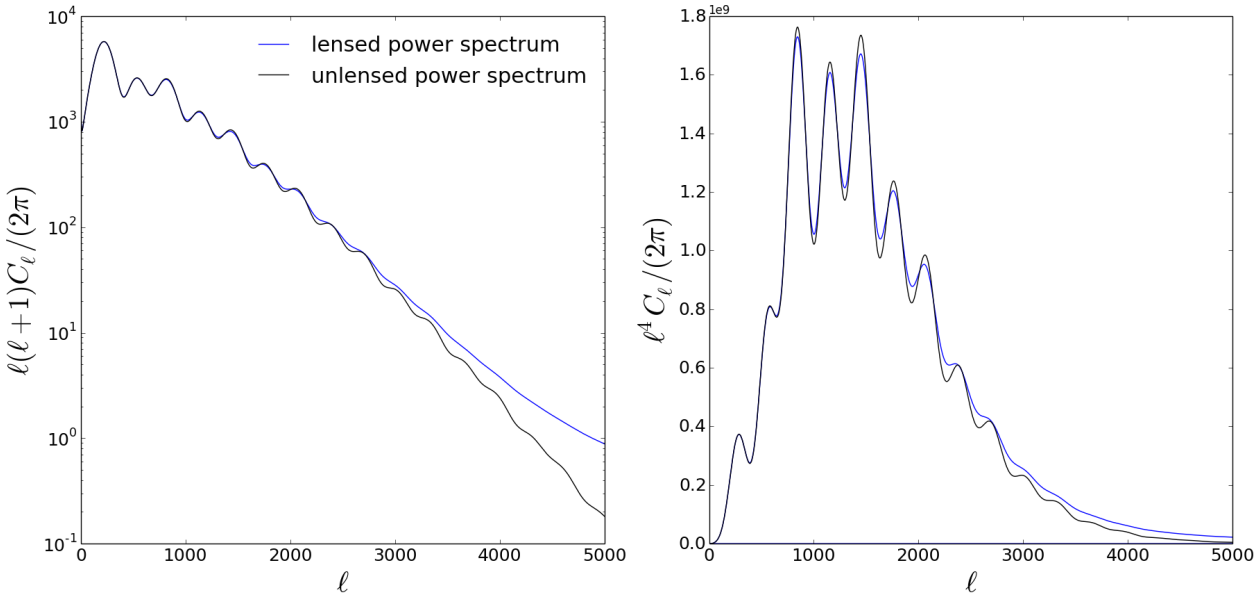

Figure 1.2: Effect of the gravitational lensing on the CMB temperature power spectrum. The left panel (log scale, $\sim \ell^2 C_\ell$) illustrates the transfer of power from the large scales to the small scales, the right panel (linear scale, $\sim \ell^4 C_\ell$) illustrates the smoothing of the acoustic peaks.

order $C_\ell^{\Psi\Psi}$, we have:

$$\tilde{C}_\ell \;=\; C_\ell + \int d\boldsymbol{\ell}'[\boldsymbol{\ell}'.(\boldsymbol{\ell}-\boldsymbol{\ell}')]^2 C^{\Psi}_{|\boldsymbol{\ell}-\boldsymbol{\ell}'|} C_{\ell'} - C_\ell \int d\boldsymbol{\ell}'(\boldsymbol{\ell}.\boldsymbol{\ell}')^2 C^{\Psi}_{\ell'}. \tag{1.20}$$

As illustrated in Figure 1.2, the effect of the lensing is to smooth the acoustic peaks and to transfer power from large scales to small scales.

1.1.4 Astrophysical foregrounds

The microwave sky emission is contaminated by foregrounds of astrophysical origin. They need to be modeled (or subtracted) in order to get an unbiased measurement of cosmological parameters. We can decompose the observed temperature at a given position in the sky as the sum of lensed CMB fluctuations and astrophysical foreground emission: $\Delta T(\hat{n},\nu) = \Delta T^{\rm CMB}(\hat{n}) + \Delta T^{\rm f}(\hat{n},\nu)$. The blackbody nature of the CMB ensures that its temperature in thermodynamic units is independent of the frequency of observation ν; this property will be key for separating the cosmological and

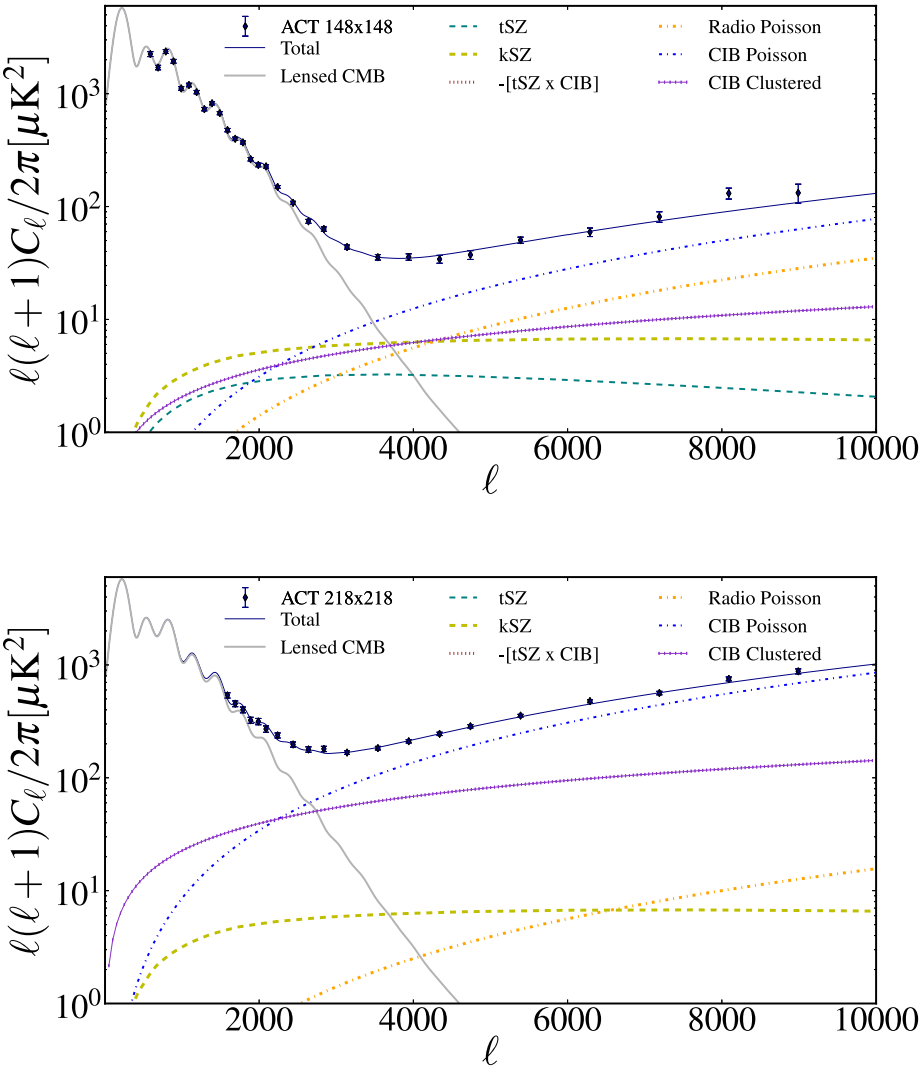

Figure 1.3: Foreground model for the ACT experiment at 148 GHz (top) and 218 GHz (bottom) (Dunkley et al. 2013). The foregrounds have different shape and frequency scaling. The Galactic dust contribution does not appear on the figures as it has been subtracted from the data. The measurement of the power spectra will be discussed in detail in Chapter 2.

astrophysical signal.

We will focus specifically on the Atacama Cosmology Telescope (see section 1.3.2) foreground model. The telescope has been observing in two frequencies bands, centered at 148 GHz and 218 GHz. The dominant foregrounds at these frequencies are the thermal and kinematic Sunyaev-Zel'dovich effect (tSZ and kSZ), the emission from dusty infrared galaxies and radio galaxies, and

the thermal emission from Galactic dust[17] (Dunkley et al. 2013). Defining $B_\ell^{\alpha\beta} = \ell(\ell+1)C_\ell^{\alpha\beta}/(2\pi)$, the observed cross power spectrum between frequencies α and β[18] is then modeled as:

$$B_\ell^{\alpha\beta} = B_\ell^{\rm CMB} + B_\ell^{\rm tSZ,\alpha\beta} + B_\ell^{\rm kSZ} + B_\ell^{\rm CIB,\alpha\beta} + B_\ell^{\rm tSZ\times CIB,\alpha\beta} + B_\ell^{\rm rad,\alpha\beta} + B_\ell^{\rm Gal,\alpha\beta} \tag{1.21}$$

We will now discuss the physical properties and the model used for each term.

1. The tSZ effect accounts for the inverse Compton scattering of CMB photons with relativistic electrons in the intergalactic medium of massive galaxy clusters (Sunyaev & Zeldovich 1980). It results in an increase in photon energies along the lines of sight that pass through clusters. The effect can be described as additional frequency-dependent temperature anisotropies[19]:

$$\Delta T^{tSZ}(\hat{n},\nu) = g_{x(\nu)}\frac{\sigma_T}{m_e c^2}\int \frac{d\chi}{dz}\frac{dz}{1+z}P_e(\hat{n},z), \tag{1.22}$$

   where $P_e(\hat{n},z) = n_e(\hat{n},z)k_B T_e(\hat{n},z)$ is the electron pressure in the direction $\hat{n}$ and at redshift z. The frequency dependence of this effect is encoded in the spectral function $g_x = x\coth(x/2) - 4$, with $x(\nu) = h\nu/k_B\bar{T}$. The tSZ takes low energy photons to high energy. The deficit in low energy photons results in $g_{x(\nu)}$ being negative for $\nu < 217$ GHz. The power spectrum of the thermal SZ effect is modeled as $B_\ell^{\rm tSZ,\alpha\beta} = a_{\rm tSZ}B_\ell^{\rm tSZ,0}(g_\alpha g_\beta/g_0^2)$, where $B_\ell^{\rm tSZ,0}$ is a template tSZ power spectrum at a reference frequency $\nu = \nu_0$. The template is obtained from hydrodynamic simulations, which allow accurate determination of the pressure profiles P_e in the presence of baryonic physics[20] (Battaglia et al. 2012). The amplitude $a_{\rm tSZ}$ which describes the normalization of the power spectrum is left as a free parameter. It is an important parameter as it is sensitive to the abundance of galaxy clusters and can then be used to constrain cosmological parameters that control their growth such as σ_8 and Ω_m (Komatsu & Seljak 2002).

2. The electrons scattering photons also carry a bulk velocity. The kinematic Sunyaev-Zel'dovich

[17] These sources have been named "Galactic Cirrus" as their structure is fairly cloud-like.
[18] $C_\ell^{\alpha\beta} = \langle T^\alpha(\boldsymbol{\ell})T^{\beta *}(\boldsymbol{\ell})\rangle$ with $\alpha,\beta \in [148, 218]$GHz.
[19] Here we use the non relativistic formula, relativistic correction of order 10% are expected.
[20] Radiative cooling, star formation, feedback from AGN and supernovae.

effect is a Doppler shift due to the bulk motion of the electrons (Sunyaev & Zeldovich 1980). This effect does not depend on the frequency of the incoming photon so the produced kSZ anisotropies are frequency independent:

$$\Delta T^{kSZ}(\hat{n}) = -\frac{\sigma_T}{c}\int \frac{d\chi}{dz}\frac{dz}{1+z} n_e(\hat{n},z)e^{-\tau(z)}(\boldsymbol{v}(\hat{n},z).\hat{n}), \tag{1.23}$$

where $\tau(z)$ is the optical depth at redshift z. The kSZ contribution to the ACT power spectrum is modeled as $B_\ell^{\rm kSZ} = a_{\rm kSZ}\tilde{B}_\ell^{\rm kSZ}$, where $\tilde{B}_\ell^{\rm kSZ}$ is a template derived from the same hydrodynamic simulations as the tSZ spectra. Again $a_{\rm kSZ}$ describes the amplitude of the kSZ effect. The kSZ power spectrum is given by the sum of two different components. A low redshift component (homogeneous kSZ) is due to the peculiar velocity of galaxy clusters and a high redshift one (patchy kSZ) is due to fluctuation in the ionized fraction and electron density during the epoch of reionization[21] (see for example (Iliev et al. 2006)).

3. Two populations of galaxies can be observed in the ACT frequency bands (Dunkley et al. 2011). These are the dust dominated sources which are part of the Cosmic Infrared Background (CIB), and the synchrotron dominated radio sources. The radio sources are modeled as a simple Poisson shot noise component $B_\ell^{{\rm rad},\alpha\beta} \propto a_s\ell^2 f(\alpha,\beta)$ where $f(\alpha,\beta)$ scale the signal with frequency, and a_s is the amplitude of the signal. Clustering of CIB galaxies has been detected at CMB frequency, so the dusty galaxies are modeled as the sum of a Poisson and clustered component $B_\ell^{{\rm CIB},\alpha\beta} \propto a_p\ell^2 g(\alpha,\beta) + a_c\ell^{2-n}h(\alpha,\beta)$. Finally, a possible spatial correlation between clusters, which contributes to the tSZ, and CIB galaxies[22] is included with the template $B_\ell^{{\rm tSZ}\times{\rm CIB},\alpha\beta}$ (Addison et al. 2012).

4. The last foreground relevant for ACT is the diffuse Galactic dust emission from the interstellar medium. The dust is heated by absorption of UV/optical photons and radiates in the infrared. This foreground is not isotropic, with more dust emission coming from regions close the Galactic center. We will discuss in detail in Chapter 2 how the dust contribution is modeled,

[21] The epoch of reionization is the period in which the neutral gas filling the Universe was ionized due to the emergence of the first radiating objects, current constraints suggest that it happens between redshift $6 \leq z \leq 15$.

[22] Both trace the same underlying matter density field.

measured and subtracted from our measurement of the power spectrum.

The power spectra of the foregrounds at 148 GHz and 218 GHz are shown in Figure 1.3, highlighting the shape and the frequency scaling of the different astrophysical contaminations.

1.2 Polarization of the Cosmic Microwave Background

1.2.1 Thomson scattering and E mode polarization

In the tight coupled limit, the photon-baryon plasma can be described as a fluid, where the photon distribution can be described only with a monopole $\theta_0(\mathbf{x}, t)$ and a dipole $\theta_1(\mathbf{x}, t)$. When the mean free path of the photon increases, another moment becomes non-negligible: the quadrupole of the photon distribution $\theta_2(\mathbf{x}, t)$[23]. We will now explain how this quadrupole anisotropy generates polarization of the CMB photons.

Light propagating in the z-direction has its magnetic and electric field oscillating in the x-y plane; the electric field of a monochromatic plane electromagnetic wave can be written

$$\begin{aligned} E_x(t) &= A_x(t)e^{i\omega t} \\ E_y(t) &= A_y(t)e^{i(\omega t+\phi)}. \end{aligned} \tag{1.24}$$

If the time evolution of the direction of the electric field is non-random, the wave is said to be polarized. In practice, the way to measure the polarization of an electromagnetic waves is to measure the Stokes parameters[24]:

$$\begin{aligned} I &= \langle|\mathbf{E}.\hat{e}_x|^2\rangle + \langle|\mathbf{E}.\hat{e}_y|^2\rangle = I_x + I_y, \\ Q &= I_x - I_y, \\ U &= \left\langle\left|\mathbf{E}.\frac{(\hat{e}_x+\hat{e}_y)}{\sqrt{2}}\right|^2\right\rangle - \left\langle\left|\mathbf{E}.\frac{(\hat{e}_y-\hat{e}_x)}{\sqrt{2}}\right|^2\right\rangle = I_x^{45} - I_y^{45}. \end{aligned} \tag{1.25}$$

[23]It can be shown that all moments above the dipole scale as $\theta_\ell \propto \theta_{\ell-1}/\tau$ where τ is the optical depth of the plasma. It is very large in the tight coupled limit and starts to decrease when the Universe becomes more and more transparent.

[24]There is a 4th Stokes parameter, V, that is non zero for circular polarization, it's not relevant for CMB polarization so we will not discuss it here.

Measuring U is the same as measuring Q in a basis rotated by 45°. These three parameters are enough to describe the linear polarization of CMB photons[25].

To understand the origin of the polarization of the CMB photons, let's consider incoming light scattering off a single electron (Dodelson 2003; Hu & White 1997a). Consider incoming unpolarized radiation in the -x direction scattered at right angles into the z direction. Heuristically, incoming radiation shakes an electron in the direction of its electric field vector, causing it to radiate with an outgoing polarization parallel to that direction. However, since the outgoing polarization must be orthogonal to the outgoing direction ($\mathbf{E}.\mathbf{k} = 0$), incoming radiation that is polarized parallel to the outgoing direction cannot scatter, leaving only one polarization state. The situation is illustrated in the top left panel of Figure 1.4. Of course, we must generalize to radiation incident on an electron from all direction. The top right panel illustrates the situation for an isotropic radiation (monopole). The net polarization of the outgoing photon is zero because radiation coming from all the directions have equal intensity. The bottom left panel shows a dipole pattern, where red, blue and black denotes high, small and average intensity respectively. Again the total polarization is zero because the blue and the red average to medium intensity. To produce polarized radiation, the incoming radiation must have a non-zero quadrupole as illustrated in the bottom right panel of the figure, where the outgoing wave has a greater intensity along the y-axis than along the x-axis so the light is polarized.

In the following we will introduce the mathematical formalism that is used to describe CMB polarization. Before we do so, we will use an heuristic argument to predict the polarization pattern produced by overdensities and underdensities on the last scattering surface. Imagine an electron falling into a potential well, corresponding to a matter over-density. The closer an electron is to an over density the faster it is falling. In the frame of the electron, particles on a bigger and smaller radius are moving away (Figure 1.5). In the meantime, particles on the same isocontour of density comes closer. This phenomena, illustrated in the left panel of Figure 1.6, generates quadrupole anisotropies. The right panel show the behavior of an electron around an under-density, where the opposite happens. The two dominant polarization patterns are also shown as headless vector in the

[25]The Stokes parameter are especially useful because they are measurable quantities, the angular bracket represents temporal average over the integration time of the detector.

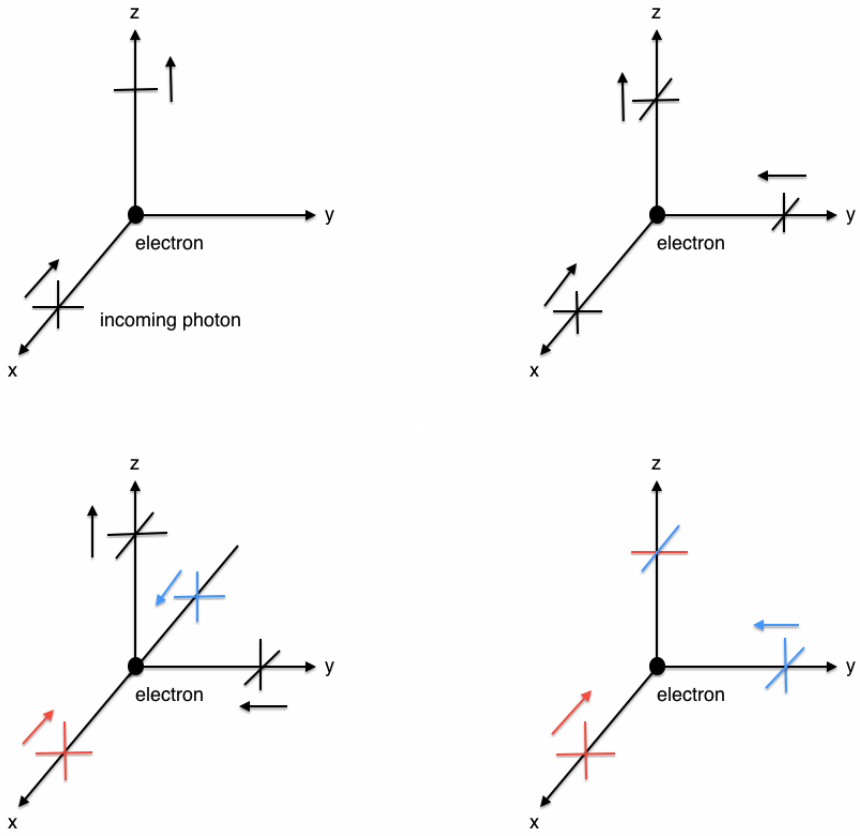

Figure 1.4: The effect of Thomson scattering on photon polarization. (Top left) unpolarized radiation propagating along the -x direction scatters off an electron and is emitted along the z direction, incoming radiation that is polarized parallel to the outgoing direction cannot scatter, so the outgoing radiation is polarized along the y direction. (Top right) monopole and (Bottom left) dipole radiation distribution scattering off a single electron, no polarization is produced. (Bottom right) incoming radiation with non zero quadrupole, the outgoing radiation is polarized.

figure. In fact these pattern are the only ones that can be created by scalar perturbation. They are invariant under a parity operation (x $\rightarrow$ -x) and are called E mode polarization.

1.2.2 Mathematical formalism

From their definition (Eq (1.26)), it is clear that the value of the Stokes parameters Q and U depends on the choice of coordinate. Consider the rotation of the coordinate system by an angle α

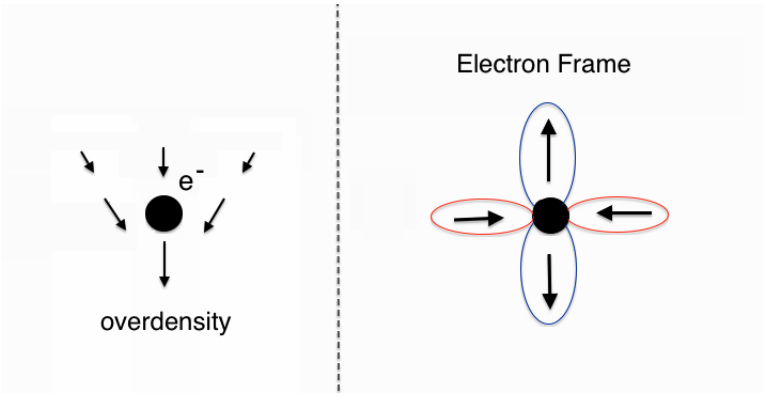

Figure 1.5: Left panel: Velocity field of plasma particles falling into a potential well. The right panel shows the quadrupole measured in the frame of the electron.

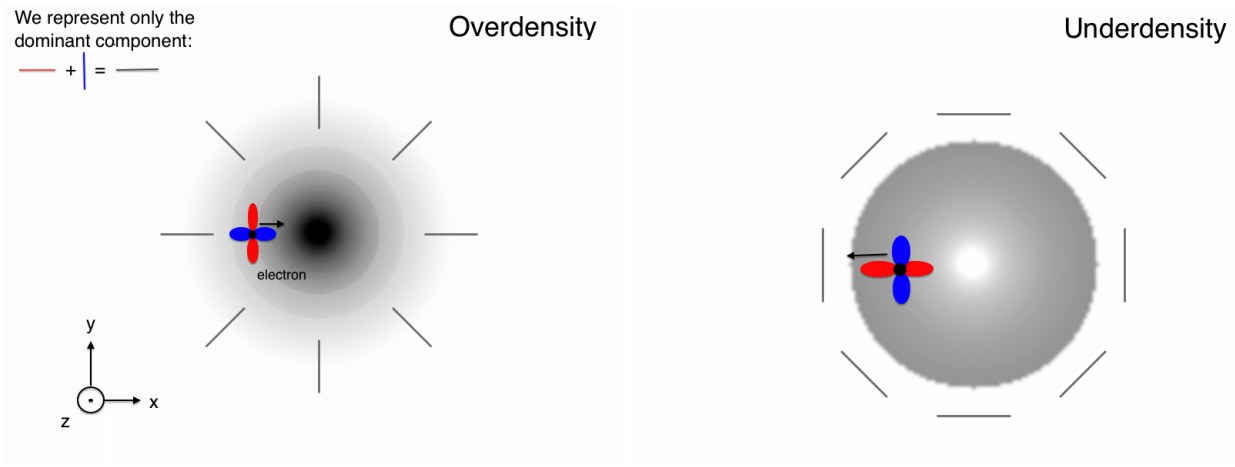

Figure 1.6: Generation of the E mode polarization pattern around scalar perturbations. Here we represent only the dominant component transmitted in the z direction.

around the direction of observation $\hat{n} = \hat{e}_z$

$$\begin{pmatrix} x' \\ y' \end{pmatrix} = \begin{pmatrix} \cos\alpha & \sin\alpha \\ -\sin\alpha & \cos\alpha \end{pmatrix} \begin{pmatrix} x \\ y \end{pmatrix}. \tag{1.26}$$

The Stokes parameters transform as:

$$\begin{pmatrix} I'(\hat{n}) \\ Q'(\hat{n}) \\ U'(\hat{n}) \end{pmatrix} = \begin{pmatrix} 1 & 0 & 0 \\ 0 & \cos 2\alpha & \sin 2\alpha \\ 0 & -\sin 2\alpha & \cos 2\alpha \end{pmatrix} \begin{pmatrix} I(\hat{n}) \\ Q(\hat{n}) \\ U(\hat{n}) \end{pmatrix}. \tag{1.27}$$

The intensity is a scalar quantity: its value is independent of the frame of observation. Q and U transform as the components of a 2×2 symmetric trace free tensor (Kamionkowski et al. 1997):

$$P_{ab}(\hat{n}) = \frac{1}{2} \begin{pmatrix} Q(\hat{n}) & U(\hat{n}) \\ U(\hat{n}) & -Q(\hat{n}) \end{pmatrix}. \tag{1.28}$$

The polarization tensor $P_{ab}(\hat{n})$ is an extremely useful quantity. It contains all information on the polarization of the CMB, and its form is independent of a particular choice of a coordinate system. Any 2×2 symmetric trace-free tensor can be uniquely decomposed into a part of the form $\mathcal{E}_{ab}A = (-\partial_a\partial_b + \frac{1}{2}\delta_{ab}\nabla^2)A$ and another part of the form $\mathcal{B}_{ab}B = \frac{1}{2}(\epsilon_{ac}\partial^c\partial_b + \epsilon_{bc}\partial^c\partial_a)B$ where A and B are scalar functions[26] (Smith 2006). Let's use again the flat-sky approximation. The Fourier modes $e^{i\boldsymbol{\ell}\mathbf{x}}$ provide a basis for a scalar function on a plane; we then define a basis for the Fourier decomposition of a 2×2 symmetric trace free tensor: $({}^E e^{i\boldsymbol{\ell}\mathbf{x}})_{ab} = \frac{\sqrt{2}}{\ell^2}\mathcal{E}_{ab}(e^{i\boldsymbol{\ell}\mathbf{x}})$ and $({}^B e^{i\boldsymbol{\ell}\mathbf{x}})_{ab} = \frac{\sqrt{2}}{\ell^2}\mathcal{B}_{ab}(e^{i\boldsymbol{\ell}\mathbf{x}})$, where the pre-factor has been chosen in order to get an orthonormality relation between the different modes: $\int d^2x ({}^E e^{i\boldsymbol{\ell}\mathbf{x}})^*_{ab} ({}^E e^{i\boldsymbol{\ell}'\mathbf{x}})^{ab} = \delta(\boldsymbol{\ell} - \boldsymbol{\ell}')$. We can expand the polarization field in this basis:

$$P_{ab}(\mathbf{x}) = \frac{1}{\sqrt{2}} \int d\boldsymbol{\ell} E(\boldsymbol{\ell}) ({}^E e^{i\boldsymbol{\ell}\mathbf{x}})_{ab} + B(\boldsymbol{\ell}) ({}^B e^{i\boldsymbol{\ell}\mathbf{x}})_{ab}. \tag{1.29}$$

To get an expression for $E(\boldsymbol{\ell})$ and $B(\boldsymbol{\ell})$, we invert this relation[27]

$$E(\boldsymbol{\ell}) = \frac{2}{\ell^2} \int d^2x P_{ab}(\mathbf{x}) \mathcal{E}^{ab}(e^{-i\boldsymbol{\ell}\mathbf{x}}) \tag{1.30}$$

$$B(\boldsymbol{\ell}) = \frac{2}{\ell^2} \int d^2x P_{ab}(\mathbf{x}) \mathcal{B}^{ab}(e^{-i\boldsymbol{\ell}\mathbf{x}}). \tag{1.31}$$

[26] This is analogous to the decomposition of a vector as a gradient and a curl.
[27] Using the orthogonality of $({}^E e^{i\boldsymbol{\ell}\mathbf{x}})_{ab}$ and $({}^B e^{i\boldsymbol{\ell}\mathbf{x}})_{ab}$.

The polarization information is now contained in two scalar fields: the E modes $E(\boldsymbol{\ell})$ and B modes $B(\boldsymbol{\ell})$. Unlike Q and U they do not depend on the choice of a coordinate system. The Stokes parameters are useful because they are measurable quantities, and the E and B modes are useful because they can be directly related to theory.

These modes can be simply related to the Stokes parameters:

$$\begin{aligned} E(\boldsymbol{\ell}) &= \frac{2}{\ell^2}\int d^2x(\ell^a\ell^b - \frac{\boldsymbol{\ell}^2}{2}\delta^{ab})P_{ab}e^{-i\boldsymbol{\ell}\mathbf{x}} \\ &= \frac{1}{\ell^2}\int d\mathbf{x}\left[(\ell_x^2-\ell_y^2)Q(\mathbf{x}) + 2\ell_x\ell_y U(\mathbf{x})\right]e^{-i\boldsymbol{\ell}\mathbf{x}} \end{aligned} \tag{1.32}$$

$$\begin{aligned} B(\boldsymbol{\ell}) &= -\frac{2}{\ell^2}\int d^2x(\epsilon^{ac}\ell_c\ell^b)P_{ab}e^{-i\boldsymbol{\ell}\mathbf{x}} \\ &= -\frac{1}{\ell^2}\int d^2x\left[\begin{pmatrix}\ell_y\\-\ell_x\end{pmatrix}^T\begin{pmatrix}Q & U\\U & -Q\end{pmatrix}\begin{pmatrix}\ell_x\\\ell_y\end{pmatrix}\right]e^{-i\boldsymbol{\ell}\mathbf{x}} \\ &= -\frac{1}{\ell^2}\int d^2x\left[2\ell_x\ell_y Q(\mathbf{x}) - (\ell_x^2-\ell_y^2)U(\mathbf{x})\right]e^{-i\boldsymbol{\ell}\mathbf{x}} \end{aligned} \tag{1.33}$$

Defining ϕ_ℓ as the angle between the wave vector $\boldsymbol{\ell}$ and the Fourier plane ℓ_x axis, so that $\cos\phi_\ell = \frac{\ell_x}{\ell}$, we have

$$E(\boldsymbol{\ell}) = Q(\boldsymbol{\ell})\cos 2\phi_\ell + U(\boldsymbol{\ell})\sin 2\phi_\ell \tag{1.34}$$

$$B(\boldsymbol{\ell}) = -Q(\boldsymbol{\ell})\sin 2\phi_\ell + U(\boldsymbol{\ell})\cos 2\phi_\ell \tag{1.35}$$

$$E(\boldsymbol{\ell}) \pm iB(\boldsymbol{\ell}) = e^{\mp 2i\phi_\ell}(Q(\boldsymbol{\ell}) \pm iU(\boldsymbol{\ell})) \tag{1.36}$$

Estimating the power spectra $C_\ell^{EE} = \langle E(\boldsymbol{\ell})E^*(\boldsymbol{\ell})\rangle$ and $C_\ell^{BB} = \langle B(\boldsymbol{\ell})B^*(\boldsymbol{\ell})\rangle$ is clearly trivial. The detectors measure the Stokes parameters $Q(\mathbf{x})$ and $U(\mathbf{x})$ at different position on the sky, so we just need to Fourier transform them and apply a rotation in Fourier space to get the E and B modes. In practice, the task is complicated by the finite size of the field of observation. We will discuss this issue in detail in Chapter 4.

This seemingly simple relation in Fourier space can be rewritten in real space:

$$\begin{aligned} \Delta E(\mathbf{x}) &= (\partial_x^2 - \partial_y^2)Q(\mathbf{x}) + 2\partial_x\partial_y U(\mathbf{x}) \\ \Delta B(\mathbf{x}) &= -2\partial_x\partial_y Q(\mathbf{x}) + (\partial_x^2 - \partial_y^2)U(\mathbf{x}), \end{aligned} \tag{1.37}$$

which can be solved using Green functions. The relation between E and B modes and the Stokes parameter is non-local so that the value of the E field at a given position depends on the value of Q and U everywhere on the sky. We described in section 1.2.1 the way scalar perturbations generate polarization. This physical phenomenon is invariant under parity. Let us consider a reflection[28] $\mathcal{R}$ about the y axis, $\mathcal{R}[x] = -x$, $\mathcal{R}[\partial_x] = -\partial_x$ and $\mathcal{R}[U(\mathbf{x})] = -U(\mathbf{x})$. The E modes are invariant under this transformation, $\mathcal{R}[E(\mathbf{x})] = E(\mathbf{x})$, but the B modes are not, $\mathcal{R}[B(\mathbf{x})] = -B(\mathbf{x})$. As a result of this fundamental symmetry, scalar perturbations on the last scattering surface can not generate B modes.

1.2.3 B mode polarization

In the previous sections we have only considered scalar perturbations. In addition, inflation can also generate vector and tensor perturbations (see for example: Lesgourgues 2006). The vector modes have only decaying solutions so they should be completely subdominant and we will neglect them. We will focus on the tensor perturbations, which are uncoupled[29] to the inflaton field, but have non-decaying solution. The tensor perturbations are potentially detectable because they produce observable distortions in the CMB. The tensor perturbation can be characterized with a metric perturbation δg_{ij}:

$$\delta g_{ij} = a^2 \begin{pmatrix} 1+h_+ & h_\times & 0 \\ h_\times & 1-h_+ & 0 \\ 0 & 0 & 1 \end{pmatrix}. \tag{1.38}$$

[28] A parity transformation is defined as the flip of one spatial coordinate. In three dimensions, it is sometimes defined as the simultaneous flip of the three spatial coordinates. In 2-D, parity can not be a simultaneous flip of x and y because the determinant of the parity operation has to be equal to -1. Parity transformation correspond to the flip of either x or y.

[29] Tensor and scalar perturbations decouple and evolve independently as a consequence of the decomposition theorem.

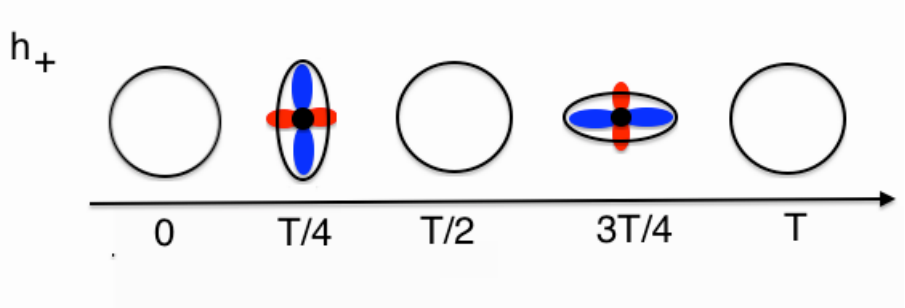

Figure 1.7: Effect of a gravitational wave on a circle of test particles. The generated quadrupole is another source of CMB polarization.

The Einstein equation for this metric translates into an evolution equation for h_α ($\alpha = +, \times$)

$$\ddot{h}_\alpha + 2\frac{\dot{a}}{a}\dot{h}_\alpha + k^2 h_\alpha = 0. \tag{1.39}$$

It's a wave equation and the solutions to this equation are called gravitational waves. Note that we already solved this equation, as it is the same evolution equation as the one satisfied by the quantum fluctuation of the inflaton field $\delta\phi$ (Eq (1.4)). Using exactly the same methodology as in Section 1.1.1, we can compute the primordial power spectrum of the gravitational waves (Dodelson 2003):

$$P_{h_\alpha}(k) = \frac{8\pi G H^2}{k^3}. \tag{1.40}$$

It differs from $P_{\delta\phi}$ only by a normalization factor. The expected amplitude of primordial tensor perturbation is small compare to the one of primordial scalar perturbation P_Ψ, indeed the tensor-to-scalar ratio $r = \frac{(P_{h_+} + P_{h_\times})}{P_\Psi} \sim \epsilon$ with $\epsilon \ll 1$ the slow roll parameter. As shown in Figure 1.7, gravitational waves produce a quadrupole distortion of space time, and are then another source of CMB polarization. The polarization generated by gravitational waves is not parity invariant: it will produce both E and B modes. Because they are the only sources of B mode polarization on the last scattering surface, a detection of primordial B modes would be the smoking gun of the production of gravitational waves during the inflationary area. It would have deep implications for fundamental physics, as the source of tensor perturbations is quantum gravity.

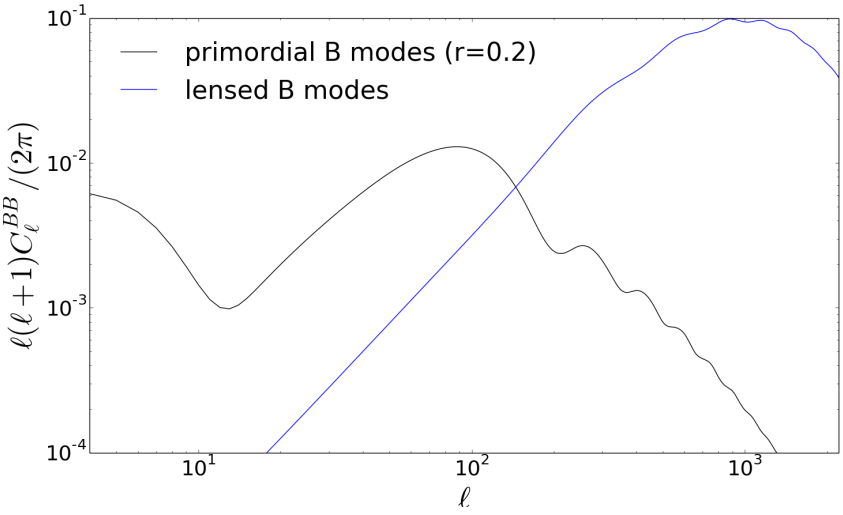

Figure 1.8: Primordial B modes and lensed B modes. The two signal peak at different angular scales. The tensor-to-scalar ratio used in this plot $r = 0.2$ is the value favored by the BICEP2 observations.

Non-primordial B modes are generated by the lensing of the CMB between the last scattering surface and us (Lewis & Challinor 2006). They contaminate the gravitational wave signal and need to be characterized. Let's consider a Universe without any primordial B modes. The lensing of CMB polarization anisotropies converts some E modes into B modes. Intuitively, the photons deflection due to gravitational potential wells breaks the symmetry of the polarization patterns. Setting the primordial B modes to zero we have at first order in Ψ:

$$\begin{aligned} \tilde{E}(\boldsymbol{\ell}) \pm i\tilde{B}(\boldsymbol{\ell}) &= e^{\mp 2i\phi_\ell}(\tilde{Q}(\boldsymbol{\ell}) \pm i\tilde{U}(\boldsymbol{\ell})) \\ &= E(\boldsymbol{\ell}) - \int d\boldsymbol{\ell}'\boldsymbol{\ell}'.(\boldsymbol{\ell}-\boldsymbol{\ell}')e^{\pm 2i(\phi_{\ell'}-\phi_\ell)}\Psi(\boldsymbol{\ell}-\boldsymbol{\ell}')E(\boldsymbol{\ell}'). \end{aligned} \tag{1.41}$$

The B modes produced by lensing of the E modes are then given by:

$$\tilde{C}_\ell^B = \int d\boldsymbol{\ell}'[\boldsymbol{\ell}'.(\boldsymbol{\ell}-\boldsymbol{\ell}')]^2 C^\Psi_{|\boldsymbol{\ell}-\boldsymbol{\ell}'|} C^E_{\ell'} \sin^2 2(\phi_{\ell'}-\phi_\ell). \tag{1.42}$$

The lensed B modes signal peaks at a different angular scale than the primordial B modes (Figure 1.8), simplifying the separation of the two signals. But because the amplitude of gravitational

waves r can be arbitrary small, being able to measure it accurately will likely require delensing. By measuring the lensing potential accurately, we might be able to remap the CMB photons to their original position, resulting in a cancellation of the lensed B mode signal.

1.2.4 TT, TE, EE and BB power spectrum

In the previous sections, we convinced ourselves that the CMB should be polarized, and we discussed physical phenomena generating E and B modes. In practice, as for the case of temperature, we measure the power spectrum of those fields. The EE, TT, TE and BB power spectra are displayed in Figure 1.9.

1. The amplitude of the EE power spectrum is lower than the amplitude of the TT power spectrum. This is due to the fact that the E mode polarization is sourced only by the quadrupole of the temperature anisotropies and is insensitive to the dipole and the monopole. The BB power spectrum is even smaller. The amplitude of the lensed B modes is given by the product of E modes with the lensing potential, which is a perturbative quantity. The primordial gravitational waves amplitude is of order the slow roll parameter ϵ times the scalar perturbation. This makes the detection of the B modes challenging.

2. The EE power spectrum is out of phase with the TT power spectrum[30]. We already mentioned that velocity perturbations on the last scattering surface are out of phase with density perturbations and that the quadrupole generating E modes comes from the local gradient of the velocity field: $E(\ell) \propto \ell v_\gamma$.

3. The E modes are generated by Thomson scattering on the last scattering surface, so there is no equivalent to the Sachs Wolfe plateau for E modes polarization .

4. The T and E modes are correlated, as they are sourced by the same scalar perturbations.

5. In the standard model, the odd-parity cross spectra TB and EB are vanishing. They remain however important quantities to estimate. They can be used in order to characterize

[30]Peaks in the temperature power spectrum correspond to troughs in the E modes power spectrum.

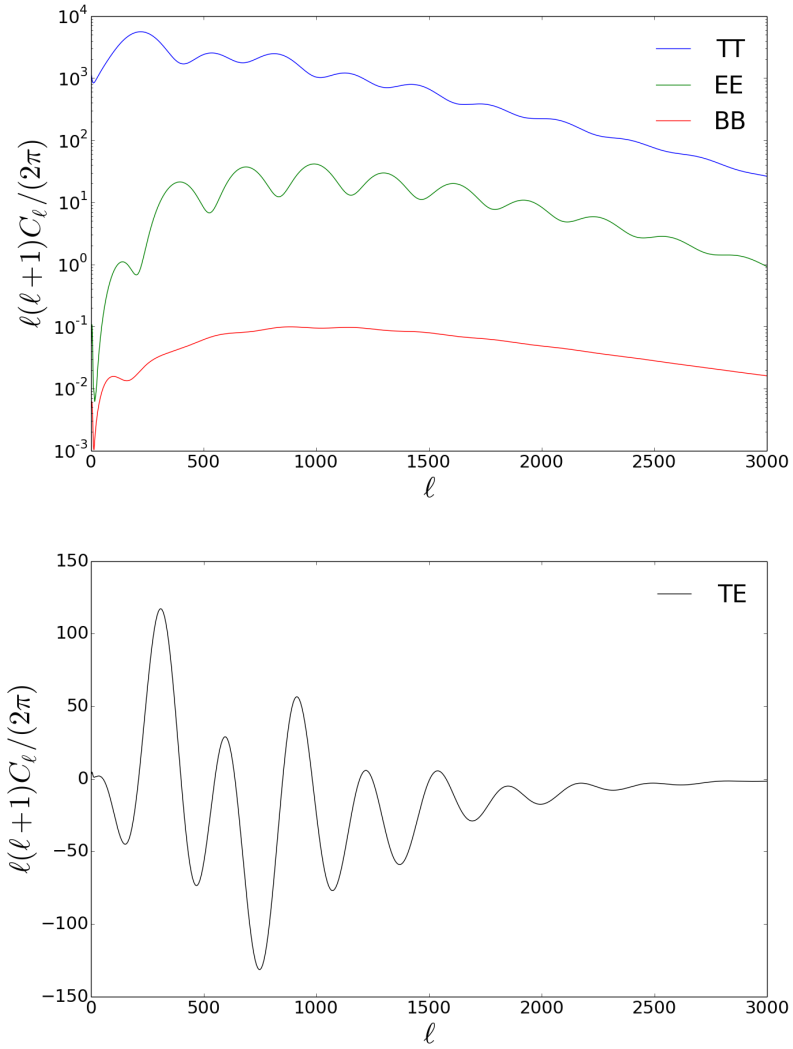

Figure 1.9: The top panel displays the TT, EE and BB power spectra. The peaks in the temperature power spectrum correspond to troughs in the E modes power spectrum. The amplitude of the B modes makes their detection challenging. The correlation between T and E modes is shown in the bottom panel.

systematics in the signal or non standard cosmological mechanisms[31].

6. The peaks in the EE power spectrum are sharper than the peaks in the TT power spectrum.

   This is due to the fact that the two main contributions to the TT power spectrum, the

[31]For example: Primordial stochastic magnetic field or interactions with pseudoscalar fields on the CMB photons trajectory.

monopole and the dipole, are out of phase, resulting in a smoothing of the acoustic peaks[32]. This has an interesting consequence: for a low noise experiment, the EE power spectrum place stronger constraints on some cosmological parameters[33] than the temperature power spectrum (Galli et al. 2014).

Finally we should mention that as for the case of temperature, we expect foregrounds to contaminate the signal. At low frequency, the synchrotron emission due to the motion of relativistic electrons around the field lines of the Galactic magnetic field is highly polarized. At high frequency, linear polarization of the thermal dust emission contaminate the signal. Finally emission from individual polarized point sources can also be detected (see for example Chapter 5).

1.3 Observing the CMB anisotropies

1.3.1 The state of the art

Since the first direct observation of the CMB by Penzias and Wilson in 1965, numerous experiments have mapped the microwave sky with higher and higher precision. The microwave telescopes can be divided into three categories: ground based, balloons and satellite telescopes. Figure 1.10 shows the full sky CMB temperature maps, in Mollweide projection, obtained by the three space missions: COBE (Smoot et al. 1992), WMAP (Bennett et al. 2012) and *Planck* (Planck Collaboration I 2013). The increase in angular resolution is striking. COBE was sensitive to multipoles below $\ell \approx 30$, in the Sachs Wolfe plateau regime of the temperature power spectrum. WMAP resolution extends to $\ell \approx 900$, which, in combination with a lower noise level, has resulted in the measurement of the first three acoustic peaks. The *Planck* nominal resolution is 5 arc minutes ($\ell \approx 2500$), and the top panel of Figure 1.11 shows the *Planck* measurement of seven acoustic peaks along with other experiments.

Ground based telescopes such as ACT and SPT (Fowler et al. 2010; Shirokoff et al. 2011) have reached arc minute resolution ($\ell \approx 10000$), because the size of the mirrors[34] of these experiments

[32] It makes the troughs less accentuated.

[33] For example on θ the angular size of the sound horizon, that is determined by measuring the position of the peaks.

[34] The resolution limit is proportional to λ/D where λ is the wavelength of observation and D the diameter of the primary mirror.

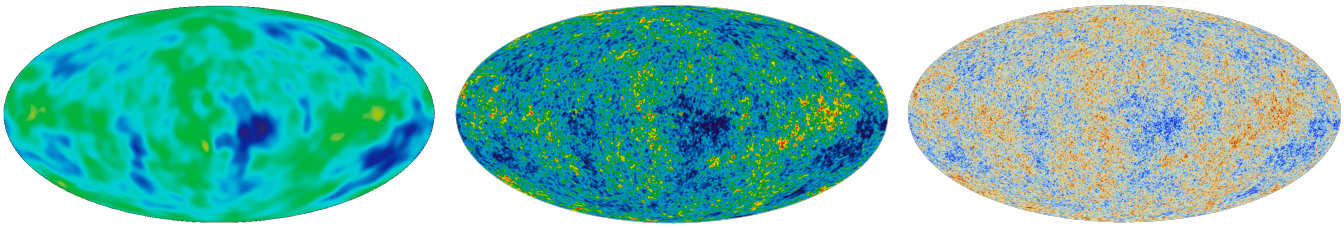

Figure 1.10: From left to right: COBE, WMAP and *Planck* full sky CMB maps (Figure courtesy of Dominic Pesce). The improvement in angular resolution between each experiment is striking.

$\approx$ 6m is large compared to the one of the *Planck* satellite $\approx$ 1.5m . However they suffer from contamination due to the atmosphere, reducing their sensitivity for measuring the large scale modes ($\ell < 500$). They can also observe only a fraction of the sky, while space missions can map the CMB emission over the full sky. In 2011, the ACT collaboration reported the first direct detection of the gravitational lensing of CMB temperature anisotropies (Das et al. 2011b), with a statistical significance of 4σ[35]. The measurement has been repeated by SPT in 2013 (6.3σ), and *Planck* (25σ). These data shown in the bottom panel of Figure 1.11 are consistent with the prediction of the ΛCDM model. The state of the art in E modes, first measured by DASI (Kovac et al. 2002) is presented in Figure 1.12. The best low ell measurement comes from the WMAP satellite, but this situation might change with the release of the *Planck* polarization data expected at the end of this year (2014). The current best TE and EE high ell power spectra have been obtained by the ACTPol collaboration. The detailed analysis leading to this measurement will be presented in Chapter 5. At the time of writing this thesis, the B mode situation is highly controversial. The BICEP2 collaboration claims a 5σ detection of primordial B modes with a tensor-to-scalar ratio $r = 0.2$ (BICEP2 Collaboration I 2014), but, there are claims that the signal could be due to polarized dust emission (Flauger et al. 2014; Mortonson & Seljak 2014). BICEP2 has mapped the polarization at a single frequency 150 GHz, which does not allow for a robust separation of primary signal and foreground. The situation should improve when *Planck* releases its polarization data, since the *Planck* 353 GHz channel is sensitive to polarized dust emission and could be used to predict the dust level at 150 GHz in the BICEP2 observation patch. The BICEP 2 measurement of B modes

[35]See also (Das et al. 2013) for the full ACT data set lensing measurement (4.6σ).

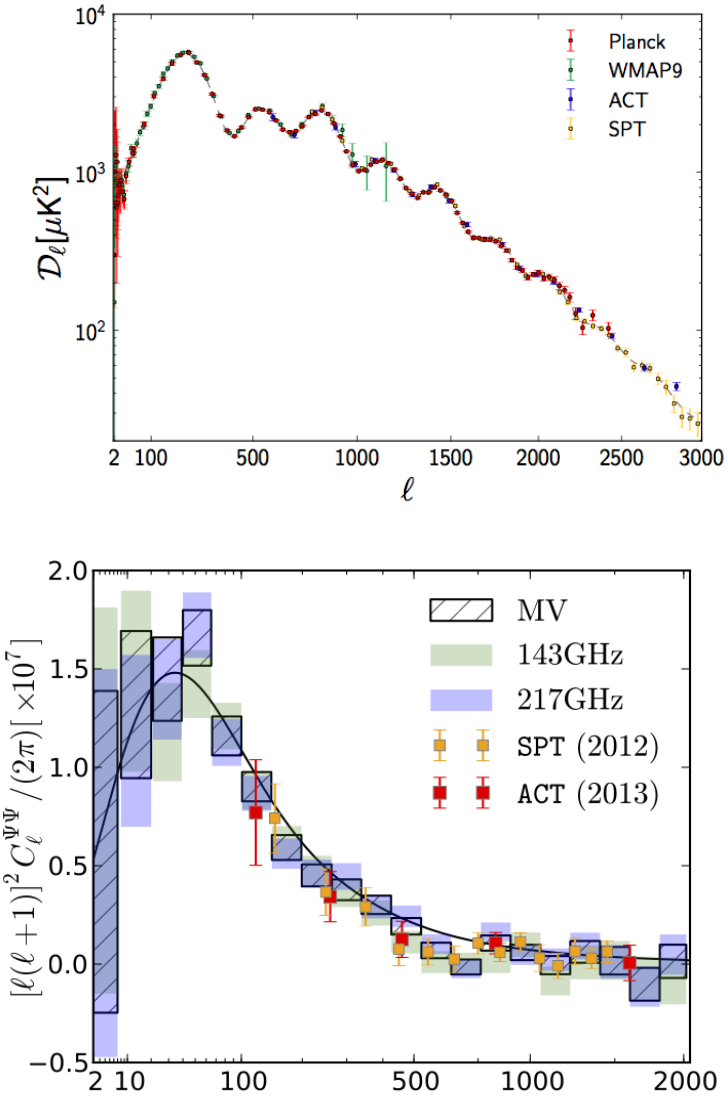

Figure 1.11: Top: State of the art of the CMB temperature power spectrum measurement (Planck Collaboration I 2013). Bottom: State of the art in CMB lensing power spectrum measurement (Planck Collaboration XVII 2013), the minimum-variance combination (MV) of the *Planck* 143 and 217 GHz channel represents a 25σ detection of CMB lensing.

along with the 2σ evidence of lensed B modes by POLARBEAR (Ade et al. 2014b) are shown in Figure 1.13.

1.3.2 The Atacama Cosmology Telescope

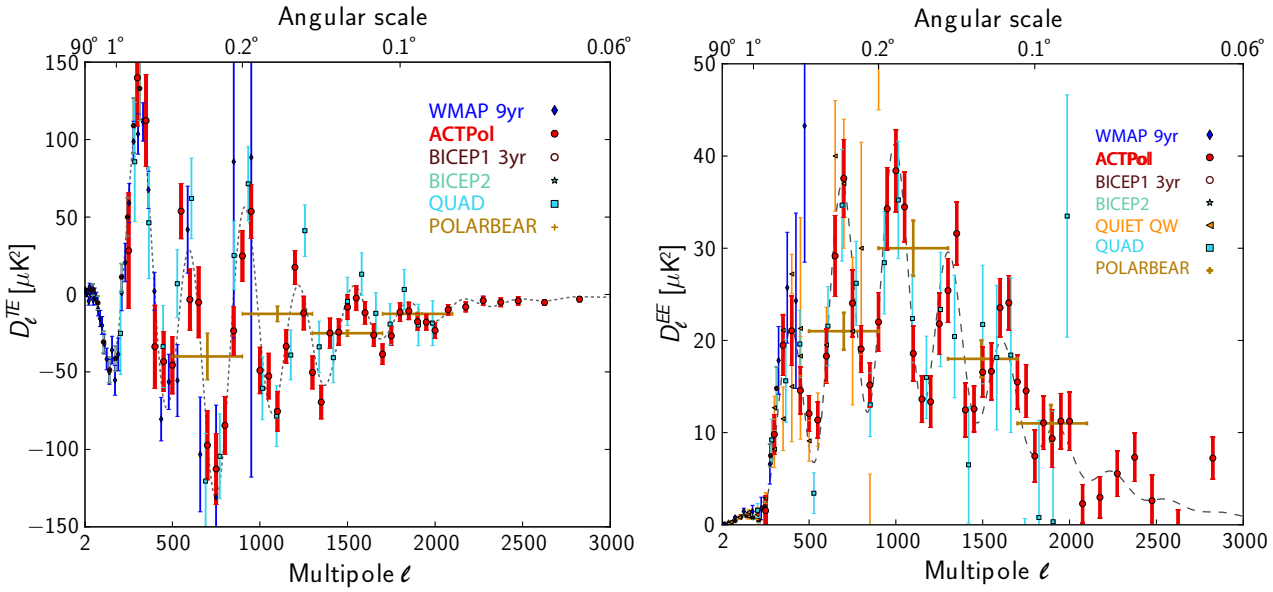

Figure 1.12: State of the art in TE power spectrum measurement (left-hand panels) and EE power spectrum measurement (right-hand panels). The current best measurement above $\ell \approx 500$ comes from the ACTPol collaboration.

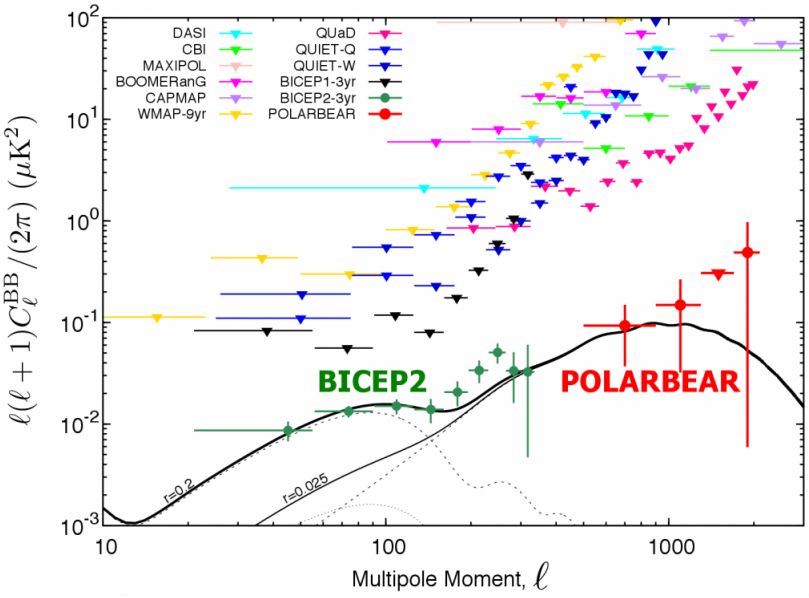

Figure 1.13: State of the art in BB power spectrum measurement (Figure courtesy of POLARBEAR collaboration). BICEP2 claims a 5σ detection of primordial B modes with a tensor-to-scalar ratio $r = 0.2$.

Table 1.1: ACT and ACTPol

	ACT	ACTPol (1 year)
Frequencies	148, 220, 270 GHz	148 Ghz
Beam size	1.3'	1.3'
Array Sensitivity (148 GHz)	32 μK$\sqrt{s}$	19 μK$\sqrt{s}$
Observation time	3 years	3 months
Coverage	600 sq. degrees	276 sq. degrees

In this section, we will present the telescope and the data pipeline used by the ACT collaboration. ACT is a 6-meter off-axis Gregorian telescope situated in the Atacama desert in Chile at an elevation of 5190 m. The first ACT camera, MBAC (ACT's Millimeter Bolometric Array Camera), had three channels operating at 148 GHz, 218 GHz and 277 GHz. The instrument is described in detail in Swetz et al. 2011. Between 2007 and 2010 ACT observed mainly along two constant-declination strips on the sky: one running along the celestial equator, and the other along declination $-55°$ in the southern sky. MBAC was decommissioned and replaced by the polarization-sensitive ACTPol camera (Niemack et al. 2010) in 2013 (see Table 1.1 for a comparison of the two experiments). During its first year of observation, ACTPol concentrated on four "deep fields" approximately centered on the celestial equator at right ascensions 150°, 175°, 355° and 35°. The data pipeline of ACT and ACTPol can be decomposed as follows

1. The data obtained by the telescope are called time-ordered data (TOD), which are the response of each detector to the sky signal as a function of time. Each individual detector is dominated by noise (atmospheric and electronic noise). The calibration of the detector array (gain and beam calibration) is done using planet observations.

2. The data from all the detectors and for a given duration of observation are optimally coadded into a map of the sky. ACT and ACTPol mapmaking consists of solving the maximum likelihood equation $(P^T N^{-1} P)\mathbf{m} = P^T N^{-1}\mathbf{d}$, where $\mathbf{m}$ is the solution map, a vector of length given by the number of pixels, P is a matrix projecting the map into the time stream and N is a model for the noise covariance matrix. The matrix $P^T N^{-1} P$ is too large to be stored or directly inverted, so the system is solved iteratively using a preconditioned conjugate gradient

method. The maps obtained are unbiased by construction. They are also nearly optimal if the noise model N is a good representation of the true noise covariance matrix.

3. The next step in the pipeline is the power spectrum estimation, which we will describe in detail in the following chapters. We used a pseudo C_ℓ approach where the maps are Fourier transformed and squared. The effect of the incomplete sky coverage, beams and the different filters applied to the data are then deconvolved.

4. Finally theoretical power spectrum (produced with CAMB) are fitted to the data power spectrum. We sample the posterior distribution $P(\boldsymbol{\theta}|\boldsymbol{d}) \propto P(\boldsymbol{d}|\boldsymbol{\theta})P(\boldsymbol{\theta})$ of the 6 ΛCDM parameters[36] (and foregrounds and some extensions) using a basic MCMC algorithm.

This is of course a non exhaustive list of what has been done with ACT and ACTPol. Other studies involve: lensing estimation, cross-correlation with other surveys, cluster and extra galactic point sources studies.

[36] $\{\Omega_b h^2, \Omega_c h^2, \theta_A, \Delta_R^2, n_s, \tau\}$

Chapter 2

The Atacama Cosmology Telescope: Temperature Power Spectrum Measurements from Three Seasons of Data

2.1 Introduction

In this Chapter, we present the measurement of the power spectra of CMB temperature anisotropies at 148 GHz and 218 GHz from a subset of Atacama Cosmology Telescope (ACT) observations performed over the 2008, 2009 and 2010 observing seasons, and covering approximately 600 $\deg^2$ of the sky. This is approximately twice the survey area used in a previous measurement of the ACT power spectrum (Das et al. 2011a, hereafter D11). Dunkley et al. (2013) use the temperature bandpowers reported in this Chapter to generate likelihood functions which form the basis of the cosmological parameter constraints reported by Sievers et al. (2012).

The Chapter is organized as follows. In Section 2.2 we describe the observations and the estimation of the beam transfer functions. We discuss the calibration of the maps in Section 2.3. Section 2.4 describes the pipeline used to process the maps into the angular power spectrum. Treat-

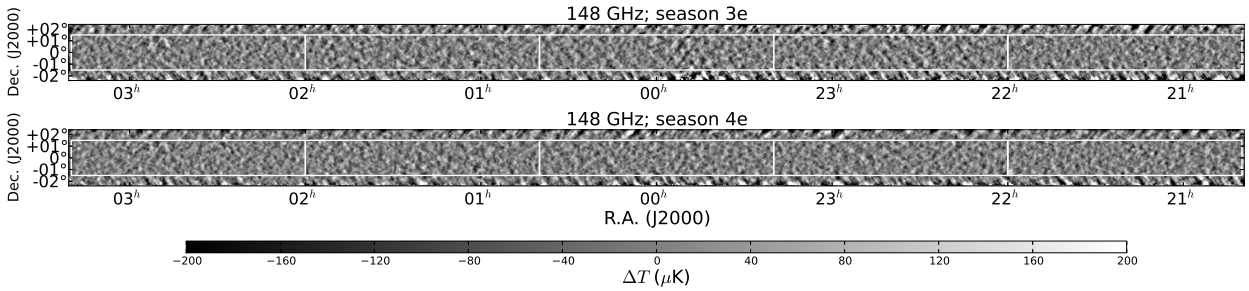

Figure 2.1: Equatorial maps (ACT-E) made from 2009 (upper panel) and 2010 (lower panel) 148 GHz observations filtered to emphasize modes in the range $\ell = 500 - 2500$. The four data splits in either season were co-added to make this plot. Also delineated are the patches used for computing power spectra.

ment of point sources and other foregrounds is discussed in Section 2.5. Simulations used to test and validate various portions of the power spectrum estimation pipeline are described in Section 2.6. The power spectrum results and consistency checks are presented in Section 2.7. We conclude in Section 2.8.

2.2 Observations and Fields

2.2.1 Equatorial Observations

Observations on the ACT equatorial (ACT-E) strip were performed in the 2009 and 2010 seasons, and run along the celestial equator with a right ascension span of 100 degrees, and a width of 3 degrees along the declination direction. For the power spectrum analysis, we make single season maps, and following D11 we divide the data within each season into four *splits* in time, by distributing data from roughly every fourth night into a different split, generating four split-maps, each of which is properly cross-linked. The maps are also spatially divided into five patches on which power spectrum estimation is performed separately. We explicitly avoid the edges of the maps where the cross-linking is poor and the noise is inhomogeneous. A representation of the season 3e and season 4e 148 GHz maps and patches are shown in Fig. 2.1. The two seasons share the same footprint on the sky, and common patches were defined to facilitate the computation of cross season power spectra. Fig. 2.2 shows the noise power spectra of the ACT-E maps by season against the CMB-only theory.

For most seasons, and for 148 GHz, on largest angular scales ($\ell < 500$) atmospheric noise dominates, while for intermediate angular scales ($500 < \ell < 2500$) fluctuations in the CMB dominate the variance. At smaller angular scales detector noise becomes the most significant contribution.

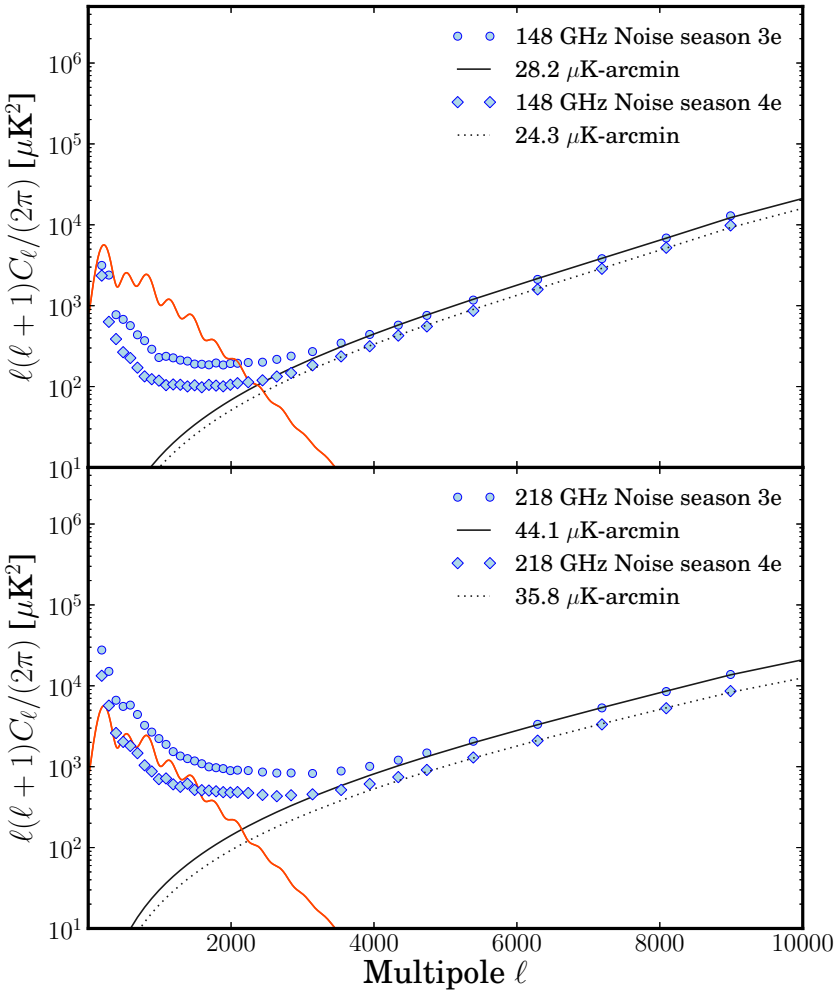

Figure 2.2: Noise spectra for each season for the ACT-E maps for 148 GHz (upper panel) and 218 GHz (lower panel). The red solid line shows the CMB-only spectrum. At 148 GHz the power spectrum is sample variance limited at $\ell < 2500$, while at 218 GHz detector and atmospheric noise dominates on most scales.

2.2.2 Southern Observations

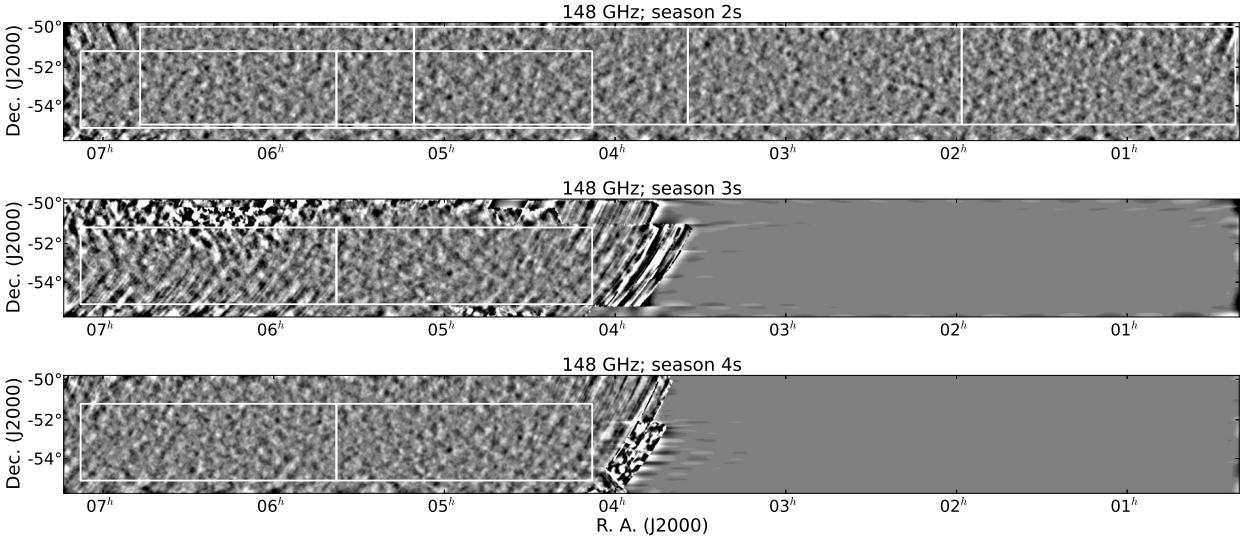

Figure 2.3: Southern maps (ACT-S) made from 2008 (top panel) 2009 (middle panel) and 2010 (bottom panel) 148 GHz observations filtered to emphasize modes in the range $\ell = 500 - 2500$. The four data splits were co-added to make this plot. Also delineated are the patches used for computing power spectra. The smaller two patches common between the three maps are used to compute cross-season cross-power spectra. The four larger patches for season 2sf are used to compute the full footprint 2008-only cross-power spectrum. Areas of large noise or stripes are heavily down weighted in the analysis. The color scale is the same as Fig 2.1.

The observations made on the southern sky across various seasons had different footprints, requiring a somewhat involved strategy for efficiently computing the power spectrum. Filtered versions of various season maps are shown in Fig. 2.3. The largest coverage was obtained in the 2008 season (the same area on which D11 was based). When computing the power spectrum within the 2008 data set, we used four large patches collectively covering 292 deg^2 (we refer to this full footprint as "season 2 south full" or season 2sf in short). For computing the power spectrum within the other two seasons, as well as to compute the cross-power spectra between any pair of the three seasons it was necessary to define another set of two patches (shown by the smaller contiguous rectangles in Fig. 2.3) that had a common footprint across the seasons. As discussed in Section 2.4, care was taken not to double count information while combining the different spectra. The noise power spectra of each of the season maps are displayed in Fig. 2.4 against the CMB-only theory.

The season 3s map is mostly noise dominated on all scales in either frequency – we keep this season in our analysis to tease out information from cross-season spectra, but the season 3s-only spectrum is heavily downweighted in our likelihood.

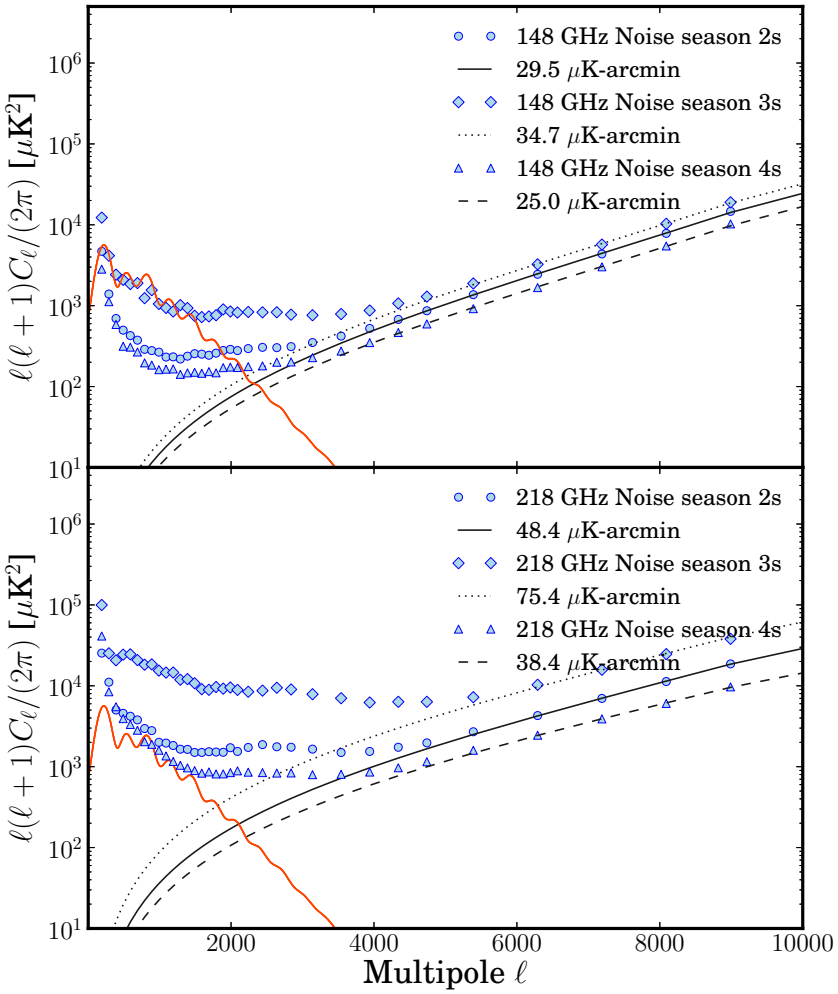

Figure 2.4: Noise spectra for each seasons for the ACT-S maps for 148 GHz (upper panel) an 218 GHz (lower panel). The red solid line shows the CMB-only spectrum. Season 3s is significantly noisier than the other two seasons. Note that the combination of seasons 3s and 4s is more sensitive than season 2s which was used in D11 and Dunkley et al. (2011).

2.2.3 Beam Transfer Functions

The beams are estimated independently for each array and season (Hasselfield et al., 2013) from observations of Saturn following a procedure similar to the one described in Hincks et al. (2010). Radial beam profiles from the planet maps are transformed to Fourier space by fitting a set of basis functions whose analytic transform is known. The fit yields the beam transform as well as a covariance matrix following a procedure similar to that discussed in D11.

2.3 Calibration

The final map calibration is performed in two stages: first, the 148 GHz map from the lowest-noise season is calibrated against the WMAP sky map, and then the 148 GHz maps from the remaining seasons and 218 GHz maps from all seasons are calibrated against the WMAP-calibrated 148 GHz map.

2.3.1 WMAP Calibration

ACT map-making and observing strategies result in maps with unbiased large-angle modes that can be compared to WMAP maps of the same region. The maps are cross-linked, i.e. every point in the survey has been observed during both its rising and setting. The transfer function of the maps is unity to better than 1% at angular scales corresponding to $\ell > 300$ (Dünner et al., 2013). We calibrate the 148 GHz ACT maps directly to WMAP 7-year 94 GHz maps (Jarosik et al., 2011) of the identical regions using the cross-correlation method described in Hajian et al. (2011). By matching the ACT-WMAP cross-spectrum to the ACT power spectrum and the WMAP 7-year power spectrum (Larson et al., 2011) in the range $300 < \ell < 1100$, we calibrate the 148 GHz ACT spectrum to 2% fractional temperature anisotropy uncertainty (Hajian et al., 2011). Calibration to WMAP is done on the deepest seasons for both ACT-E and ACT-S strips, which correspond to season 4e (2010 observing season) and season 2sf (2008 observing season) data respectively. These calibrated maps are used as references to calibrate other seasons as described below.

2.3.2 Relative Season Calibration

Once the deepest 148 GHz season has been calibrated with respect to WMAP, we cross-correlate that map with a 148 GHz map from another season, take the ratio of the cross-season cross-power spectrum to the in-season cross-power spectrum, and fit for a calibration factor. For example, on the equator, the 148 GHz season 4e map is calibrated with respect to WMAP. We then compute the ratio $C_\ell^{4e\times 4e}/C_\ell^{3e\times 4e}$ to estimate the calibration for the season 3e 148 GHz map. This internal method lets us use a much wider range of angular scales (we use an ℓ range of width 2000 starting at $\ell = 500$ for 148 GHz and $\ell = 1000$ for 218 GHz) than possible with WMAP. Using this method, we achieve the following relative calibration uncertainties (expressed as σ_{X-Y} for season X calibrated against season Y) : $\sigma_{3e-4e} \simeq 0.7\%$, $\sigma_{3s-2s} \simeq 3\%$, and $\sigma_{4s-2s} = 3\%$ for 148 GHz, and $\sigma_{3e-4e} \simeq 2\%$, $\sigma_{3s-2s} \simeq 9\%$, and $\sigma_{4s-2s} = 4\%$ for 218 GHz maps. Note that for the ACT-S season 3s maps the calibration uncertainties are higher, as is expected from the fact that this season is largely noise dominated on most scales (see Fig. 2.4). The internal spectrum from this season gets highly downweighted in our likelihood. To tie together the 148 GHz and 218 GHz internal calibrations, we finally calibrate the best season 218 GHz map with respect to its 148 GHz counterpart, achieving $\sigma_{2s(218)-2s(148)} \simeq 1.3\%$, and $\sigma_{4e(218)-4e(148)} \simeq 1.7\%$. This gives the overall calibration of the reference 218 GHz map as 2.4% for ACT-S and 2.6% for ACT-E.

2.4 Temperature Power Spectrum Analysis

The power spectrum analysis methods used here are essentially the same as in D11, the major modifications being due to the smaller extent of the ACT-E maps in the declination direction compared to ACT-S, and the multi-season nature of the spectra.

2.4.1 Preprocessing of maps

Power spectra estimated from an incomplete sky suffer from mode-to-mode coupling. The CMB power spectrum is very red, falling off as ℓ^{-4} on small angular scales. This makes it very vulnerable to the leakage of large to small scale modes. The mode-to-mode coupling can be deconvolved in order to get an unbiased power spectrum, but the estimator becomes suboptimal. A method to

minimize the leakage, and the corresponding increase in the variance of the estimator is to prewhiten the maps (Das et al. (2009)). It consist in real space operations on a map which makes its power spectrum as flat as possible. We convolve the maps with a top hat filter

$$\begin{aligned} T_R(\mathbf{x}) &= \int d\mathbf{x}' W_R(\mathbf{x}' - \mathbf{x}) T(\mathbf{x}') \\ W_R(\mathbf{x}) &= \begin{cases} \frac{1}{\pi R^2} & \text{if} \quad |\mathbf{x}| \leq R \\ 0 & \text{otherwise.} \end{cases} \end{aligned} \tag{2.1}$$

The Fourier transform of the difference map $T_{R-3R} = T_R - T_{3R}$ is given by

$$T_{R-3R}(\boldsymbol{\ell}) = 2\left(\frac{J_1(\ell R)}{\ell R} - \frac{J_1(3\ell R)}{3\ell R}\right) T(\boldsymbol{\ell}). \tag{2.2}$$

In the limit where $\ell R \ll \sqrt{2}$, we can expand the Bessel functions and get:

$$T_{R-3R}(\boldsymbol{\ell}) \approx (\ell R)^2 T(\boldsymbol{\ell}). \tag{2.3}$$

By choosing a suitable radius, we can then prewithen the ℓ^{-4} falling part of the power spectrum, which significantly reduces the leakage and the uncertainty on the estimated small scale CMB power spectrum[1]. We also follow D11 and apply a high-pass filter to the maps to suppress the large angular scale modes ($\ell < 500$) which are not as well constrained as others.

2.4.2 Data Window

Each patch is then multiplied with a data window before the power spectrum is computed. The window is a product of three components: a point source mask, an apodization window, and the $n_{\rm obs}$ map giving the number of observations in each pixel. The point source mask is further described in Section 2.5.2. To simplify the application, we create a single $n_{\rm obs}$ map per patch by adding the individual $n_{\rm obs}$ maps from all the splits involved (four splits for the single frequency spectrum, and the 8 splits for the cross-frequency or cross-season spectrum), and apply this as a weight function.

[1]We also need to choose the disc radius R so that the window function turns over when white noise starts to dominate, in order to avoid noise rising as ℓ^4.

This essentially downweights the poorly observed regions of the patch. An additional step is applied to the ACT-E patches. Since the ACT-E strip is only 3 degrees wide, the absolute Fourier space resolution in the declination direction is $\Delta\ell_y = 120$. This leads to instability in the mode-mode coupling calculations due to poor sampling of power in the Fourier space. To remedy this, we extend the patches in the declination direction by adding a 0.7-degree-wide-strip of zero valued pixels on either side, such that the final declination width of the zero-padded patch is 4.4 degrees. To minimize ringing from the edges of the patch, we also apply an apodization window which is generated by taking a top-hat function that is unity in the center and zero over 10 pixels at the edges of the original patch, and convolving it with a Gaussian of full width at half maximum of $2\farcm5$ for ACT-S and $14\farcm0$ for ACT-E. Another addition to the pipeline for the ACT-E patches is the application of a Galactic dust mask (see Section 2.5.1). Monte Carlo simulations demonstrate that we retrieve an unbiased estimate of the spectrum with these additions to our well-tested pipeline.

2.4.3 Binning of the power spectrum

It is important to note that the narrow inherent width of the ACT-E strip, as well as the smaller dimensions of the mulitseason ACT-S patches prompted us to adopt wider bins for the bandpowers than were used in D11. Most notably, over the acoustic peaks ($\ell < 2000$) the bins used have a width $\Delta\ell = 100$ as opposed to $\Delta\ell = 50$ of D11. This choice is motivated by the fact that with the finer binning, adjacent bins remain significantly correlated for the ACT-E spectrum. In addition, evaluating the covariance using full end-to-end Monte Carlo simulations is prohibitively expensive given the iterative nature of our map-making process. Conversely, more tractable approximations might not be good enough to provide the precision deserved by the high quality of the data. With the larger bins we have verified that the bin-to-bin correlations never exceed 10% and are much smaller than 10% for most bin pairs, allowing us to treat the bandpowers as statistically independent (cf. Section 2.7.1) .

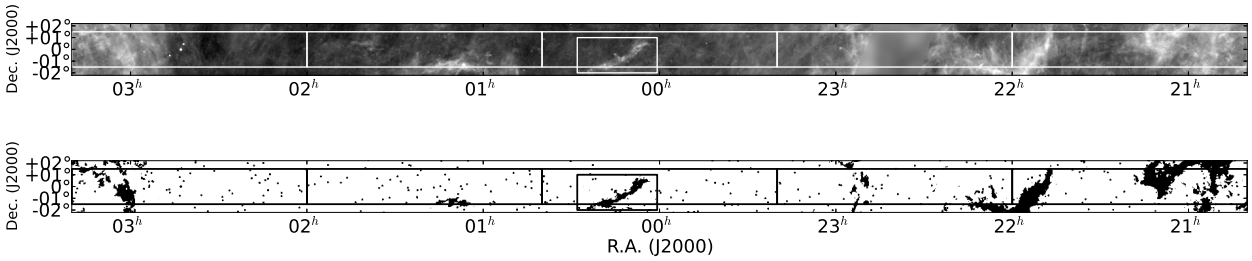

Figure 2.5: *Top:* The IRIS 100 um map on the ACT-E strip (arbitrary color scale). *Bottom:* The equatorial dust mask based on the IRIS map flux cut as described in the text. The small box near right ascension of $00^{\rm h}14^{\rm m}$ shows the "seagull"-like structure that is additionally masked out even though some pixels fall below the flux cut.

2.4.4 Cross-Season Cross-Spectrum Estimation

The temperature map corresponding to the data split i, after windowing and filtering, can be written $\tilde{T}^i(\mathbf{x}) = W(\mathbf{x})T^i_F(\mathbf{x})$ with $T^i_F(\boldsymbol{\ell}) = F_\ell T^i(\boldsymbol{\ell})$, the filter F_ℓ accounts for the effects of beam profile, prewhitening, filtering and pixelization. Because all these operations are convolution in real space they can be written as simple multiplications in Fourier space. The 2D pseudo cross spectrum of the i and j splits is computed as:

$$\tilde{C}^{i\times j}_{\boldsymbol{\ell}} = \mathrm{Re}[\tilde{T}^{*i}(\boldsymbol{\ell})\tilde{T}^j(\boldsymbol{\ell})]. \tag{2.4}$$

The 1D pseudo power spectrum is obtained by averaging the 2D power spectrum in annular bins. The anisotropic scanning strategy translates into an anisotropic noise 2D power spectrum. We use a two-dimensional weighted average, giving less weight to Fourier modes in the noisiest part of the 2D Fourier plane:

$$\begin{aligned} \tilde{C}^{i\times j}_b &= \sum_{\boldsymbol{\ell}} P_{b\boldsymbol{\ell}} \tilde{C}^{i\times j}_{\boldsymbol{\ell}} \\ P_{b\boldsymbol{\ell}} &= \left.\frac{w_{\boldsymbol{\ell}}}{\sum_{\boldsymbol{\ell}} w_{\boldsymbol{\ell}}}\right|_{\boldsymbol{\ell}\in b} \end{aligned} \tag{2.5}$$

The pseudo power spectrum can then be expressed in term of the underlying spectrum $C_{\boldsymbol{\ell}}$:

$$\tilde{C}_b^{i\times j} = \sum_{\boldsymbol{\ell},\boldsymbol{\ell}'} P_{b\boldsymbol{\ell}} |W(\boldsymbol{\ell}-\boldsymbol{\ell}')|^2 F_{\ell'}^2 C_{\boldsymbol{\ell}'}^{i\times j}. \tag{2.6}$$

The convolution in Fourier space comes from the real space multiplication of the window with the maps. This can be rewritten in term of the true binned spectrum:

$$\begin{aligned} \tilde{C}_b^{i\times j} &= \sum_{\boldsymbol{\ell},\boldsymbol{\ell}',b'} P_{b\boldsymbol{\ell}} |W(\boldsymbol{\ell}-\boldsymbol{\ell}')|^2 F_{\ell'}^2 Q_{\boldsymbol{\ell}'b'} C_{b'}^{i\times j} \\ &= \sum_{b'} M_{bb'} C_{b'}^{i\times j}, \end{aligned} \tag{2.7}$$

where $Q_{\boldsymbol{\ell}b}$ is unity when $\boldsymbol{\ell} \in b$ and zero otherwise. The matrix $M_{bb'}$ is the mode-coupling matrix. We compute it exactly and invert it in order to get an unbiased estimator:

$$\hat{C}_{b'}^{i\times j} = \sum_{b'} M_{bb'}^{-1} \tilde{C}_{b'}^{i\times j}. \tag{2.8}$$

For same-season cross spectra, the combinatorics are exactly the same as in D11: we compute 6 cross spectra per patch for the single-frequency spectrum (the 4 "splits" in time giving rise to the 6 cross spectra), and 12 for the cross-frequency spectrum (avoiding crossing the same splits that contain data from the same nights). For cross-season spectra we combine all 16 cross-season cross-spectra, as each split from one season has independent noise from the splits in the other season. For each frequency and season pair, the cross-spectra from the patches are combined with inverse variance weighting. This results in a set of three bandpowers $\{C_b^{3e\times 3e}, C_b^{3e\times 4e}, C_b^{4e\times 4e}\}$ for ACT-E and a set of six bandpowers $\{C_b^{2s\times 2s}, C_b^{2s\times 3s}, C_b^{2s\times 4s}, C_b^{3s\times 3s}, C_b^{3s\times 4s}, C_b^{4s\times 4s}\}$ for ACT-S, for each of the two same-frequency pairs 148×148 and 218×218. For the cross-frequency spectra 148×218, where $C_b^{3e(148)\times 4e(218)}$ is distinct from $C_b^{4e(148)\times 3e(218)}$, we get a set of four bandpowers for ACT-E and nine bandpowers for ACT-S. These add up to a total of 10 cross-power spectra for ACT-E and 21 cross-power spectra for ACT-S that enter the likelihood separately with their individual bandpower covariance matrices. Additionally, there are six cross-power spectra coming from the full-footprint 2008 ACT-S map (2sf), which is added, with proper attention to the overlap between

the s2f and s2 patches.

2.4.5 Bandpower Covariance

For each cross-power spectrum above, we evaluate a bandpower covariance matrix:

$$\Theta_{bb}^{(\alpha A\times\beta B);(\gamma C\times\tau D)} = \left\langle \left(\hat{C}_b^{\alpha A\times\beta B} - \left\langle \hat{C}_b^{\alpha A\times\beta B}\right\rangle\right) \times \left(\hat{C}_b^{\gamma C\times\tau D} - \left\langle \hat{C}_b^{\gamma C\times\tau D}\right\rangle\right)\right\rangle \quad (2.9)$$

where we used Greek indices α, β, etc. to denote the seasons 3e, 2s, etc. and the uppercase Roman numerals A, B, etc. to denote frequencies. The analytic expression of the general term of this covariance matrix $\Theta_{bb}^{(\alpha A\times\beta B);(\gamma C\times\tau D)}$ is discussed in the Appendix. The total covariance matrix is a sum of two terms: a sample covariance part accounting for the fact that different seasons of observation at different frequencies are observing the same CMB modes and that some of our cross spectra have common noise, and another part coming from the covariance of uncertainties in the determination of the beam profile. The covariance matrix is computed analytically and checked against Monte Carlo simulations described in Section 2.6. This total covariance matrix is used in defining the likelihood function (Dunkley et al., 2013; Sievers et al., 2013) when determining cosmological parameters.

Along with the covariance matrices, we also generate bandpower window functions which convert a theoretical power spectrum into a band power: $C_b^{\rm th} = \sum_\ell B_{b\ell} C_\ell^{th}$. Due to different geometry and noise properties of the ACT-E and ACT-S patches, two separate window functions $B_{b\ell;ACT-s}$ and $B_{b\ell;ACT-e}$ are evaluated for the south and the equator.

2.4.6 Combining Multi-Season Spectra

For the purpose of parameter estimation, we keep the ACT-E and ACT-S spectra and covariances for each season separate in the likelihood (Dunkley et al., 2013). For display purposes and for visual comparison with other datasets we combine the spectra from different seasons (separately for

equator and south) using inverse variance weighting:

$$\tilde{C}_b^{A\times B} = \frac{\sum_{\alpha,\beta}(\Theta^{-1})_{bb}^{(\alpha A\times\beta B);(\alpha A\times\beta B)} C_b^{(\alpha A\times\beta B)}}{\sum_{\alpha,\beta}(\Theta^{-1})_{bb}^{(\alpha A\times\beta B);(\alpha A\times\beta B)}}. \tag{2.10}$$

As discussed in Dunkley et al. (2013) the amplitudes of the Galactic cirrus contributions to the ACT-E and ACT-S maps are different. Therefore, before combining the ACT-E and ACT-S spectra obtained above, we subtract the best-fit cirrus component (see 2.5.1 for more details) from the ACT-E and ACT-S spectra, and then combine them using inverse variance weighting. The multiple levels of cross-correlation used in computing the power spectrum help ensure that potential peculiarities in the observation that are located in time or space do not propagate to the final power spectrum.

2.5 Foregrounds

In the 148 GHz and 218 GHz bands the main foregrounds are emission from point sources and diffuse Galactic dust, which we treat with the application of masks as described below. Dunkley et al. (2013) and Sievers et al. (2013) also consider and constrain contributions from thermal and kinetic Sunyaev Zaldovich effects, unresolved clustered and Poisson-like infrared point sources, unresolved radio sources, and a residual Galactic cirrus component.

2.5.1 Galactic Dust

We detect a significant contribution from Galactic cirrus in our ACT-E maps, especially at 218 GHz. We employ a two-step approach for dealing with Galactic cirrus in the ACT-E maps using 100 μm dust maps from IRIS (Miville-Deschênes & Lagache, 2005) as the reference. The first step is motived by the observation that most of the dust contamination in the equatorial power spectrum comes from the regions corresponding to bright clustered structures in the dust map. Therefore, we generate a dust mask by identifying and setting to zero all pixels above a flux density of 5.44 MJy/sr as well as pixels that fall inside significantly clustered structures such as the "seagull"-like structure near right ascension of $00^{\rm h}14^{\rm m}$ shown inside the box in Fig. 2.5. This dust mask is multiplied by the point source mask described below to generate the final mask that is applied to the data.

TABLE A
COEFFICIENTS FOR GALACTIC CIRRUS MODEL

Region	$A_{\rm cirrus}$ MJy^2	Frequency GHz	A_d [a] μK/MJy	a_g
ACT-S	9.95	148	8.65	0.4
		218	30.0	5.2
ACT-E	17.9	148	8.65	0.8
		218	30.0	9.4

[a] we use a common dust coefficient for equator and south

The second step of the dust treatment is generating a model of the residual dust contamination after the application of this mask, and then to inform the parameter estimation pipeline with reasonable priors on this model (the residual model amplitude is fitted and marginalized over when constraining cosmological parameters, as described in Dunkley et al. 2013). The model is constructed as follows. Following Hajian et al. (2012) we perform a multicomponent fit to the auto-power spectrum of the IRIS map after application of the dust mask described above. The components include a power law term for the residual Galactic cirrus, a Poisson shot noise term, a term representing the clustered component of infrared emission, and a white noise term to describe the instrument. The Galactic cirrus component is modeled as $C_\ell^{\rm cirrus} = A_{\rm cirrus}\ \ell^{-2.7}$, where the value of the power law index appears to be a good fit to Herschel observations of cirrus (Miville-Deschênes et al., 2010; Bracco et al., 2011), as well as the cross correlation between ACT and BLAST (Hajian et al., 2012), and that between ACT and IRIS maps. This fitting procedure provides us with an estimate of the amplitude $A_{\rm cirrus}$ separately for the ACT-E and the ACT-S map footprints. Next, we cross-correlate the ACT maps with the IRIS template to evaluate the dust coefficient $A_d = C_\ell^{\rm ACT\times IRIS}/C_\ell^{\rm IRIS\times IRIS}$ for each frequency and each sky region. Finally, the cirrus contribution to the ACT power spectrum can be expressed as $C_\ell^{\rm gal} = A_{\rm cirrus}A_d^2\ \ell^{-2.7}$ or expressed in terms of a rescaled amplitude at $\ell_0 = 3000$: $\mathcal{B}_\ell \equiv \ell^2 C_\ell/(2\pi) = a_{\rm g}\,(\ell/\ell_0)^{-0.7}$, where we have defined $a_{\rm g} \equiv A_{\rm cirrus}\ A_d^2\ \ell_0^{-0.7}/(2\pi)$.

The various model parameters obtained from the fitting method above are displayed in Table

A. There is roughly twice as much dust in the ACT-E region as in ACT-S, but at $\ell = 3000$ and for 148 GHz it is less than 3% of the CMB signal. These values represent a frequency scaling consistent with the early release results from the Planck satellite (Planck Collaboration et al., 2011), and can be compactly written in flux units as $\mathcal{B}_\ell^{ij} = a_g(\ell/\ell_0)^{-0.7}(\nu^i\nu^j/\nu_0^2)^\beta$ μK^2 with $\beta = 1.8$, ν^i and ν^j the two frequencies being crossed, and ν_0 =148 GHz. Based on the scatter observed in these central values as well their variation depending on whether the clustering term is included in the fit, we adopt priors of $a_{gs} = 0.4 \pm 0.2$ and $a_{ge} = 0.8 \pm 0.2$ for ACT-S and ACT-E respectively. The fitted models and priors are illustrated in Fig. 2.6.

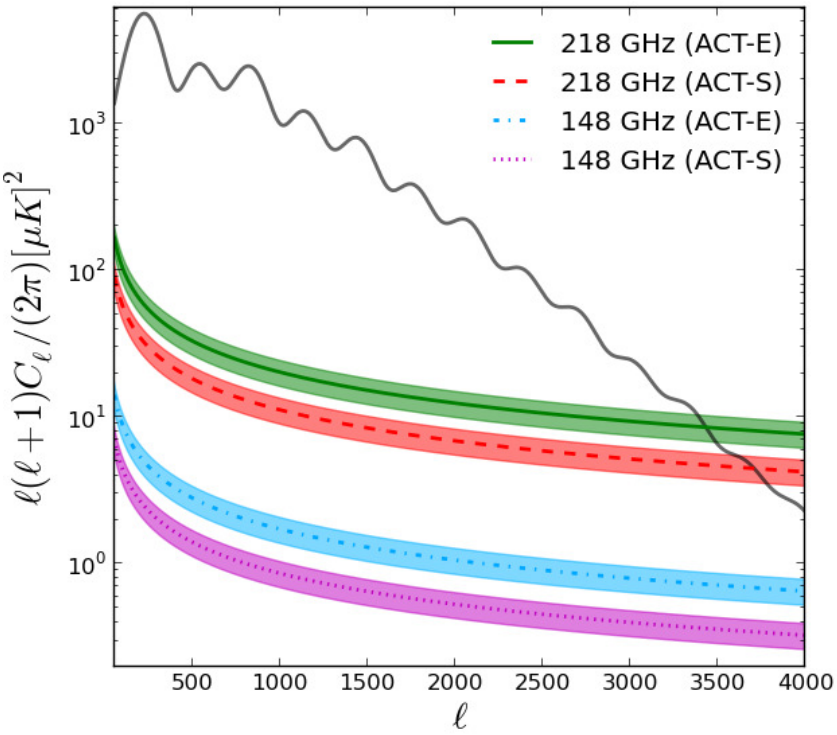

Figure 2.6: Galactic cirrus contributions to the power spectrum modeled as a power law as described in the text, for each frequency and region of the sky. The curves correspond to the best fit amplitudes obtained by cross-correlating ACT maps with cirrus component of the IRIS maps, and the band around them represent the uncertainty adopted as a prior in the ACT likelihood as discussed in Dunkley et al. (2013).

2.5.2 Point Sources

Point sources are the main astrophysical foreground for the 148 and 218 GHz bands. At these frequencies, point sources are typically either radio-loud AGN or dusty star-forming galaxies. Most of the bright sources are AGN, while most of the dusty star-forming galaxies lie below the detection threshold of our survey. Point sources must be identified and masked before the power spectrum is computed so as not to add power to the cosmological signal. We have identified sources using a matched filter algorithm (e.g., Tegmark & de Oliveira-Costa, 1998). We mask data within a 5' radius around all sources detected down to 15 mJy in either band. The residual power contributed to the power spectrum from unmasked sources below our detection threshold is expected to be 2.9 ± 0.4 μK^2 at $l = 3000$ (Gralla et al., in preparation). For details about the point source detection algorithm we used, and catalogs for the south 2008 148 GHz data, see Marriage et al. (2011).

2.6 Simulations

We ran a set of Monte Carlo (MC) simulations in order to validate the analytic prescription for the uncertainties on the cross-season cross-frequency power spectra, and to investigate bandpower covariance and possible biases in the pipeline. As our map-making procedure is iterative, it is prohibitively expensive to run a large set of end-to-end simulations that would capture all aspects of the map-making pipeline, and the noise characteristics and correlations in the actual data set. Instead, following D11, we generate signal maps as Gaussian random realizations from a power spectrum, and add to each of them a realization of a Poisson point source population, and a simulated noise map generated from the observed noise-per-pixel in the data maps. The details of the implementation are essentially the same as in Section 4 of D11 with special care taken so that signal realizations are properly correlated across different seasons and footprints. For each season and each frequency, we generate 960 signal+noise maps (four spits for each frequency), and for each realization we compute the power spectra in exactly the same way as we do for the data maps. From the large set of cross-power spectra obtained in this way we estimate the season-season covariance as well as the correlation between band powers. We find that in all cases, correlation

TABLE B
SINGLE FREQUENCY COMBINED BANDPOWERS PROVIDED FOR PLOTTING PURPOSES ONLY.
$\mathcal{B}_b = \ell_b(\ell_b+1)C_b/2\pi$ (μK^2)

		148 GHz		148 GHz × 218 GHz		218 GHz	
ℓ range	central ℓ_b	$\mathcal{B}_b$	$\sigma(\mathcal{B}_b)$	$\mathcal{B}_b$	$\sigma(\mathcal{B}_b)$	$\mathcal{B}_b$	$\sigma(\mathcal{B}_b)$
540 - 640	590	2267.4	114.3	-	-	-	-
640 - 740	690	1760.2	79.4	-	-	-	-
740 - 840	790	2411.2	97.0	-	-	-	-
840 - 940	890	1962.4	75.5	-	-	-	-
940 - 1040	990	1152.2	42.8	-	-	-	-
1040 - 1140	1090	1208.7	43.2	-	-	-	-
1140 - 1240	1190	1057.7	36.0	-	-	-	-
1240 - 1340	1290	743.1	25.7	-	-	-	-
1340 - 1440	1390	833.3	27.3	-	-	-	-
1440 - 1540	1490	683.0	22.0	-	-	-	-
1540 - 1640	1590	484.7	16.4	494.0	15.7	551.2	30.0
1640 - 1740	1690	403.1	13.3	400.6	12.6	458.5	26.9
1740 - 1840	1790	377.7	12.3	369.7	11.5	408.3	23.9
1840 - 1940	1890	266.8	9.3	272.7	9.3	327.0	20.3
1940 - 2040	1990	236.5	8.7	261.3	8.8	320.2	20.5
2040 - 2140	2090	229.2	8.1	226.6	7.7	274.7	17.9
2140 - 2340	2240	150.2	4.3	168.6	4.6	238.7	12.3
2340 - 2540	2440	109.2	3.5	128.1	3.8	199.8	10.7
2540 - 2740	2640	75.0	3.0	97.5	3.3	181.6	9.8
2740 - 2940	2840	63.7	2.9	86.0	3.2	181.9	9.6
2940 - 3340	3140	43.9	1.9	69.4	2.1	167.3	6.4
3340 - 3740	3540	35.7	2.0	65.2	2.1	183.6	6.5
3740 - 4140	3940	36.1	2.4	68.3	2.3	211.4	7.3
4140 - 4540	4340	34.4	2.8	75.5	2.7	245.7	8.3
4540 - 4940	4740	37.3	3.4	93.8	3.3	286.8	9.8
4940 - 5840	5390	50.5	3.2	109.8	3.0	355.8	9.5
5840 - 6740	6290	59.5	5.2	149.6	4.6	478.0	14.6
6740 - 7640	7190	81.6	8.7	177.9	6.6	564.4	19.9
7640 - 8540	8090	131.4	14.6	240.1	10.7	753.1	29.6
8540 - 9440	8990	133.0	25.5	265.3	16.6	878.7	44.3

between adjacent bins are insignificant at the 10% level.

We evaluate the uncertainties in the band powers using an analytic prescription described in Appendix 2.A. We verify the accuracy of these expressions by comparing the predicted error bars with the scatter of MC realizations. For isotropic white noise realizations with uniform weights, our expressions for multi-season multi-frequency error bars are good to better than a percent.

2.7 Temperature Power Spectrum Results

Power spectra are computed following the procedure outlined in Section 2.4 separately for each region (south and equator) and for each season pair. The entire set of spectra along with their covariance is passed on to the likelihood code that forms the basis of parameter constraints. Al-

though combined spectra are not used in the actual analysis, in this section we discuss various combinations of power spectra for purposes of comparison and systematic tests. Note that ACT-S and ACT-E spectra cannot be trivially combined as residual Galactic cirrus contribution to the two regions are different. Therefore, we subtract the best fit residual cirrus model (as discussed in Dunkley et al. 2013) from the estimated power spectra before combining ACT-E and ACT-S spectra. To simplify the presentation, all figures in this section portray dust-subtracted spectra. Another complication arises due to the different geometries and masking pattern of the ACT-E and ACT-S maps, which cause the theoretical bandpowers for these regions to be in principle different, although the actual differences are small. Also, due to subtle variations of the beam profile from one season to another, the beam uncertainties in individual season spectra are slightly different. All these subtleties prompted the separate treatment of power spectra in the likelihood. In this section, we neglect these subtleties and combine spectra, with inverse variance weight, across season pairs and regions of the sky. We warn the reader that such combinations are for visualization purposes only. Fig. 2.7 shows the ACT-E and ACT-S spectra combined across the different observing seasons, along with their corresponding theoretical band powers. The power spectrum combined across all seasons and across the ACT-E and ACT-S strips is displayed in Fig. 2.8. The corresponding band power values and uncertainties are tabulated in Table B. These plots portray how our pipeline is able to produce an estimate of the power spectrum over the entire multipole range of $500 - 10000$. Over the multipole range of $\ell \simeq 500 - 2500$ these spectra clearly show the Silk damping tail of the CMB power spectrum, while on smaller angular scales ($\ell \sim 2500 - 10000$) an excess from the frequency-dependent Sunyaev Zel'dovich effects and extragalactic foregrounds (radio and infrared point sources) is clearly visible (these contributions are further discussed in Dunkley et al. 2013).

Finally, we display, in Fig. 2.9, the state of the art in CMB temperature power spectrum measurements down to the damping tail where we plot the WMAP 7-year spectrum, the inverse variance combined ACT-E+ACT-S spectrum, and the recent SPT power spectrum (Story et al., 2012).

2.7.1 Power spectrum with alternative binning

As discussed in Section 2.4.3, the choice of large bins for our main power spectrum result was motivated by the need for keeping the bandpowers minimally correlated. It is of interest, however, to ask how the spectrum would have looked with smaller bins of width $\Delta\ell = 50$ over the damping tail, as was done in D11. Such a result is shown in Fig. 2.10. Note that the first through the eighth peak of the CMB can be clearly seen with this binning. We do not pursue this binning any further for the aforementioned reasons.

2.7.2 Derived CMB-only power spectrum

The ACT-E and ACT-S spectra shown in Fig. 2.7 include the primary CMB signal as well as power from foregrounds and SZ. We show the estimated primary CMB spectrum from ACT in Fig. 2.11, derived in Dunkley et al. (2013). There, the multi-frequency spectra are used to estimate the CMB in bandpowers for ACT-E and ACT-S, simultaneously with the SZ and foregrounds components. The CMB spectra for ACT-E and ACT-S are then coadded for display. No assumptions are made about the cosmological model, only that the CMB is blackbody. Using the multi-frequency data to separate components, the CMB power can be recovered out to multipoles of $\ell \sim 3500$.

2.7.3 Systematic Tests

In order to check for systematics in the map-making and power spectrum estimation pipelines, we perform various tests on the data. These are constructed such that the sky signal cancels between the various splits of the data, and only systematic effects remain. We test that the power spectrum obtained is the same in each season, in all time splits, from different parts of the array, with and without data near the telescope turnaround points, from different directions in Fourier space, and for different regions of the sky. The statistics from a subset of these tests are summarized in Tables 2.1, 2.2, 2.3, and 2.4. Given that the spectra are computed individually and then included in the likelihood with the full covariance of the different frequencies and seasons, we compute the null tests on each subset of data, both for ACT-E and ACT-S, and for different seasons.

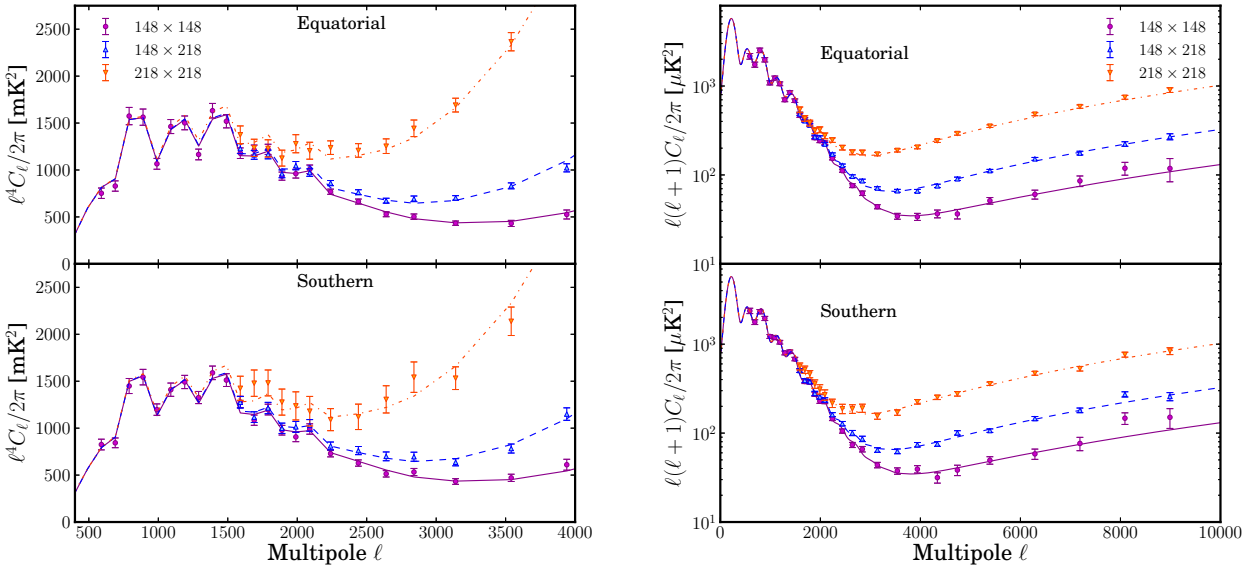

Figure 2.7: Combined multi-season power spectra for the ACT-E Strip (upper panels) and the ACT-S Strip (lower panels). The left hand panel shows a linear scale zoomed-in version of the spectrum with an ℓ^4 scaling to emphasize the higher order acoustic features. The lines show the binned version of the best fit model for each frequency pair including CMB secondaries and foregrounds from Dunkley et al. (2013). The right panel shows the entire range of the computed spectrum on a log-linear scale with the conventional $\ell(\ell+1)$ scaling. The lines show the unbinned version of the best fit model from Dunkley et al. (2013).

Cross season nulls

Table 2.1: Null test χ^2 values for the season consistency tests performed on the ACT data. The probability to exceed (PTE) the χ^2 is shown in parentheses.

Frequency	Region	Seasons	Seasons	Seasons	dof
		2008-2009	2009-2010	2008-2010	
148 GHz	South	32.2 (0.36)	30.7 (0.43)	35.0 (0.24)	30
	Equator	-	39.7 (0.11)	-	30
220 GHz	South	27.7 (0.11)	15.9 (0.72)	21.5 (0.37)	20
	Equator	-	24.2 (0.23)	-	20

First, we test the year-to-year consistency of power spectra. In order to account for differences in the ACT beam from one observing season to the next, we convolve the map from one season with

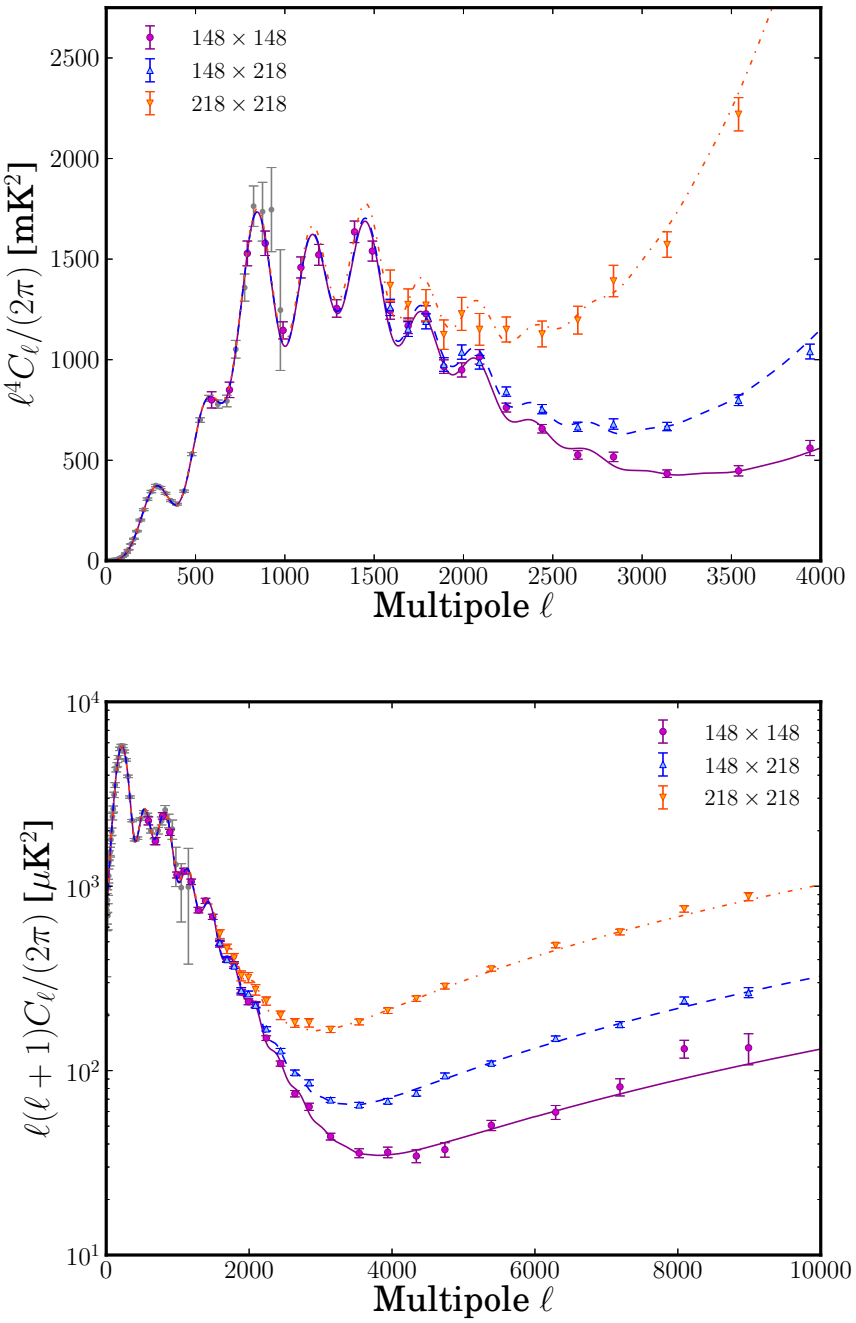

Figure 2.8: Muti-frequency power spectra combined across all seasons and the ACT-E and ACT-S regions. The upper panel shows the $\ell = 500 - 4000$ portion of the power spectrum on a linear scale with an ℓ^4 scaling to emphasize the higher order acoustic peaks. The lower panel shows the entire range of the computed spectra with the $\ell(\ell + 1)$ scaling. The lines in either case show the best fit models for each frequency pair including CMB secondaries and foregrounds from Dunkley et al. (2013). The grey data points represent the power spectrum from the WMAP seven-year data release (Larson et al., 2011).

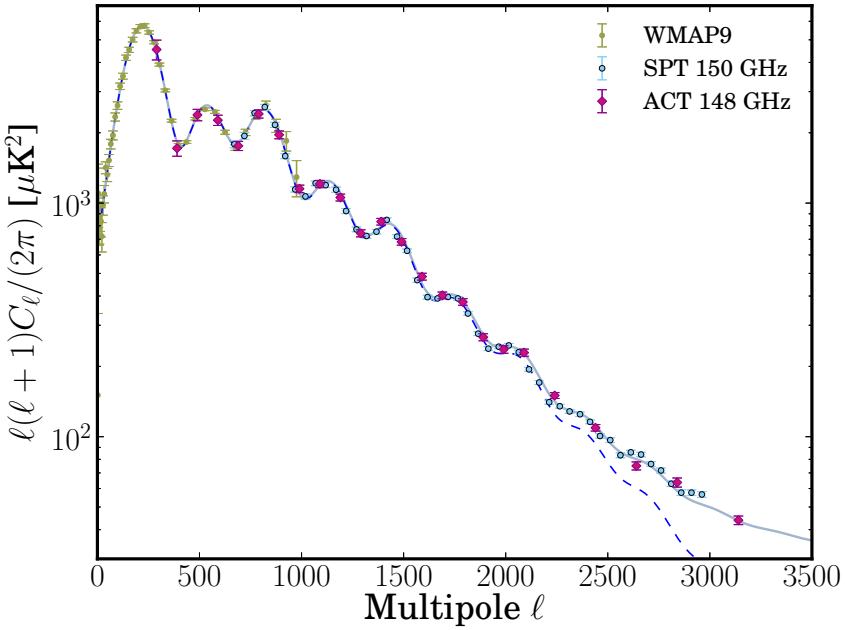

Figure 2.9: CMB temperature power spectrum measurements from the WMAP 9-year data release (Bennett et al., 2012; Hinshaw et al., 2013), the South Pole Telescope (Story et al., 2012) and ACT (this work). The solid line shows the best fit model to the ACT 148 GHz data combined with WMAP 7-year data (Larson et al., 2011). The dashed line shows the CMB-only component of the same best fit model. Although we compute the power spectrum down to $\ell = 200$, we do not use data below $\ell = 540$ in the analysis.

the beam profile of the other season being differenced, so that each map effectively has the same beam transfer function. Then we difference the corresponding splits from seasons s_1 and s_2:

$$\Delta T^i(\mathbf{x}) \equiv [T^i_{s_1}(\mathbf{x}) - T^i_{s_2}(\mathbf{x})], \tag{2.11}$$

where i = 1,2,3,4 represent the split index. The pixel weight map W corresponding to these difference splits is computed as:

$$W^{-1} = W^{-1}_{s_1} + W^{-1}_{s_2}, \tag{2.12}$$

where W_{s_1} is the total $N_{\rm obs}$ map for season s_1 etc. As with the other null tests, the azimuthal weighting is computed using the weights from the full data spectrum run. Figure 2.12 shows these test for the ACT data, while the individual χ^2 values for the tests are summarized in Table 2.1. We

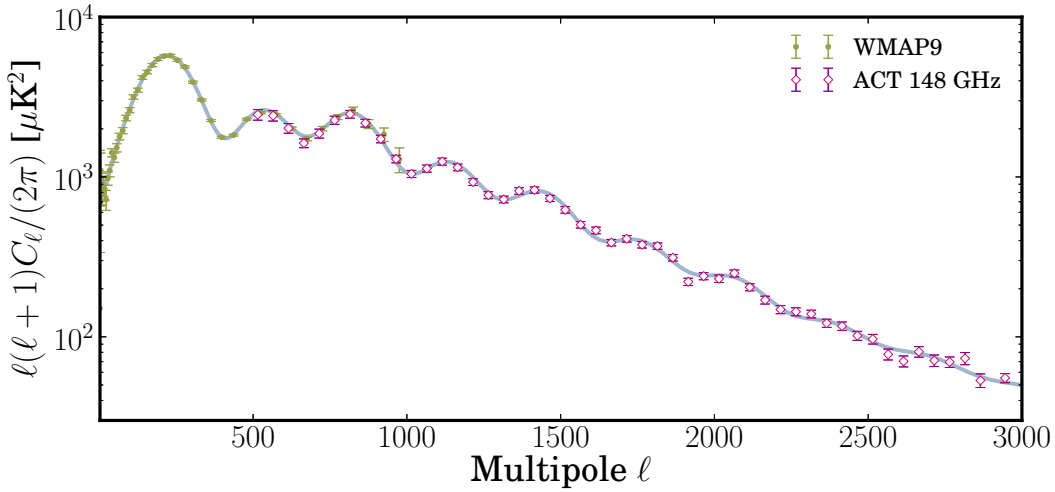

Figure 2.10: Combined ACT-E + ACT-S 148 GHz power spectrum computed with alternate binning shown alongside the WMAP 9-year data (Bennett et al., 2012; Hinshaw et al., 2013). Note that with these smaller bins, the contours of the first eight acoustic peaks of the CMB power spectrum can be clearly seen. The bandpowers are significantly correlated at this bin size, and a precise estimate of the bin to bin correlation is computationally prohibitively costly. The solid line shows the best fit model to the ACT 148 GHz data combined with WMAP 7-year data (Larson et al., 2011).

find all spectra computed in this way to be consistent with null.

Split Nulls

Table 2.2: χ^2 (PTE) values for the TOD split null tests performed on the ACT data.

Frequency	Region	Season	TOD			dof
			(1-2)x(3-4)	(1-3)x(2-4)	(1-4)x(2-3)	
148 GHz	South	2008	19.7 (0.92)	37.7 (0.16)	37.1 (0.17)	30
		2009	30.3 (0.45)	31.8 (0.38)	22.6 (0.83)	30
		2010	35.7 (0.22)	28.6 (0.54)	21.5 (0.87)	30
	Equator	2009	33.9 (0.29)	26.5 (0.65)	40.9 (0.09)	30
		2010	34.6 (0.26)	35.6 (0.22)	24.0 (0.77)	30
220 GHz	South	2008	33.1 (0.03)	28.2 (0.10)	15.3 (0.76)	20
		2009	14.4 (0.81)	11.3 (0.94)	14.8 (0.79)	20
		2010	8.8 (0.99)	16.0 (0.72)	21.0 (0.40)	20
	Equator	2009	24.9 (0.21)	19.3 (0.50)	13.3 (0.87)	20
		2010	11.8 (0.92)	16.3 (0.70)	14.0 (0.83)	20

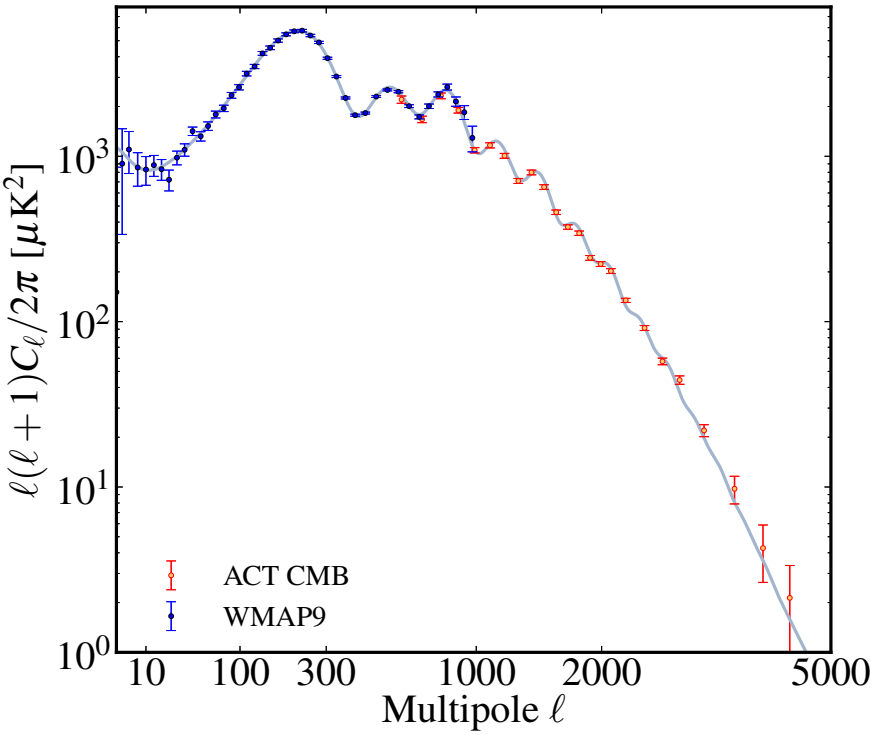

Figure 2.11: The CMB only power spectrum estimated from ACT, shown with the spectrum from the WMAP 9-year data (Bennett et al., 2012; Hinshaw et al., 2013). The errors include uncertainty due to foreground and SZ emission, as well as the relative calibration of the 148 and 218 GHz channels, and beam uncertainty. The full covariance matrix is derived in Dunkley et al. (2013). The solid line shows the CMB-only component of the best fit model for the ACT data combined with the WMAP 7-year data.

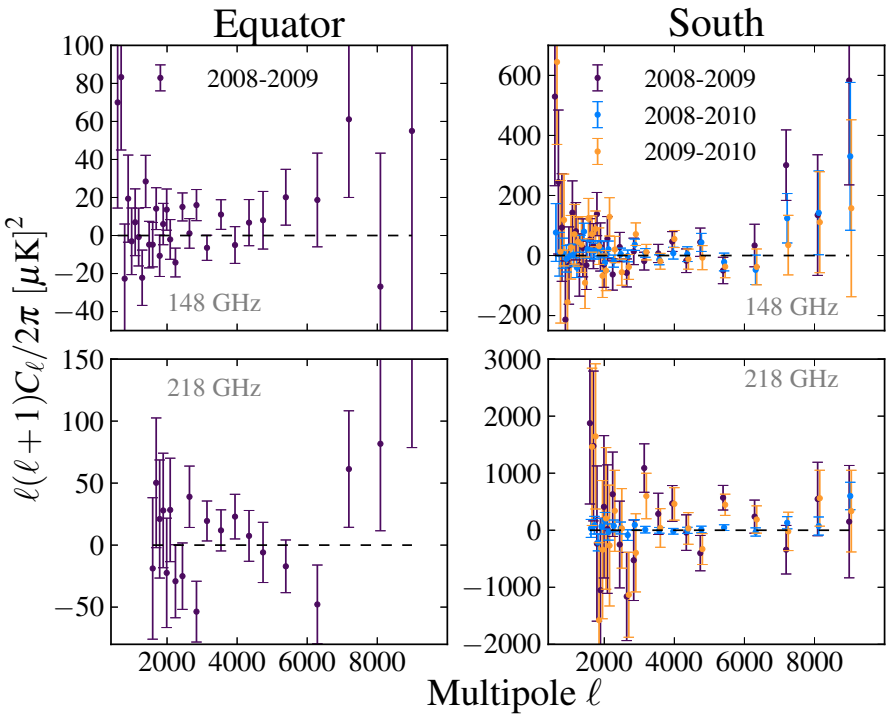

Figure 2.12: Cross season null test for the ACT data. The top row illustrate the 148 GHz cross season null tests for ACT-E (top left) and ACT-S (top right), while the bottom row show the 218 GHz cross season nulls.The χ^2 values for the fit are presented in Table 2.1 and Figure 2.14.

As discussed in Section 2.4, the data in each season are separated into four splits in such a way that the detector noise is independent from one split to another. Therefore, the difference between any two splits should be consistent with noise and the signal should subtract away. We test this by generating difference maps from each pair, and computing the two-way cross spectra from independent pairs of difference maps, e.g.:

$$\begin{aligned} T^{12}(\mathbf{x}) &\equiv [T^1(\mathbf{x}) - T^2(\mathbf{x})]/2 \\ T^{34}(\mathbf{x}) &\equiv [T^3(\mathbf{x}) - T^4(\mathbf{x})]/2. \end{aligned} \tag{2.13}$$

The difference maps are expected to contain noise but no residual signal. We estimate the cross-spectrum of the difference maps, $\hat{C}_b = \langle T^{12}T^{34} \rangle$, and the other two permutations of the differences ($\langle T^{13}T^{24} \rangle$ and $\langle T^{14}T^{23} \rangle$). These difference maps are downweighted by the same weight maps used

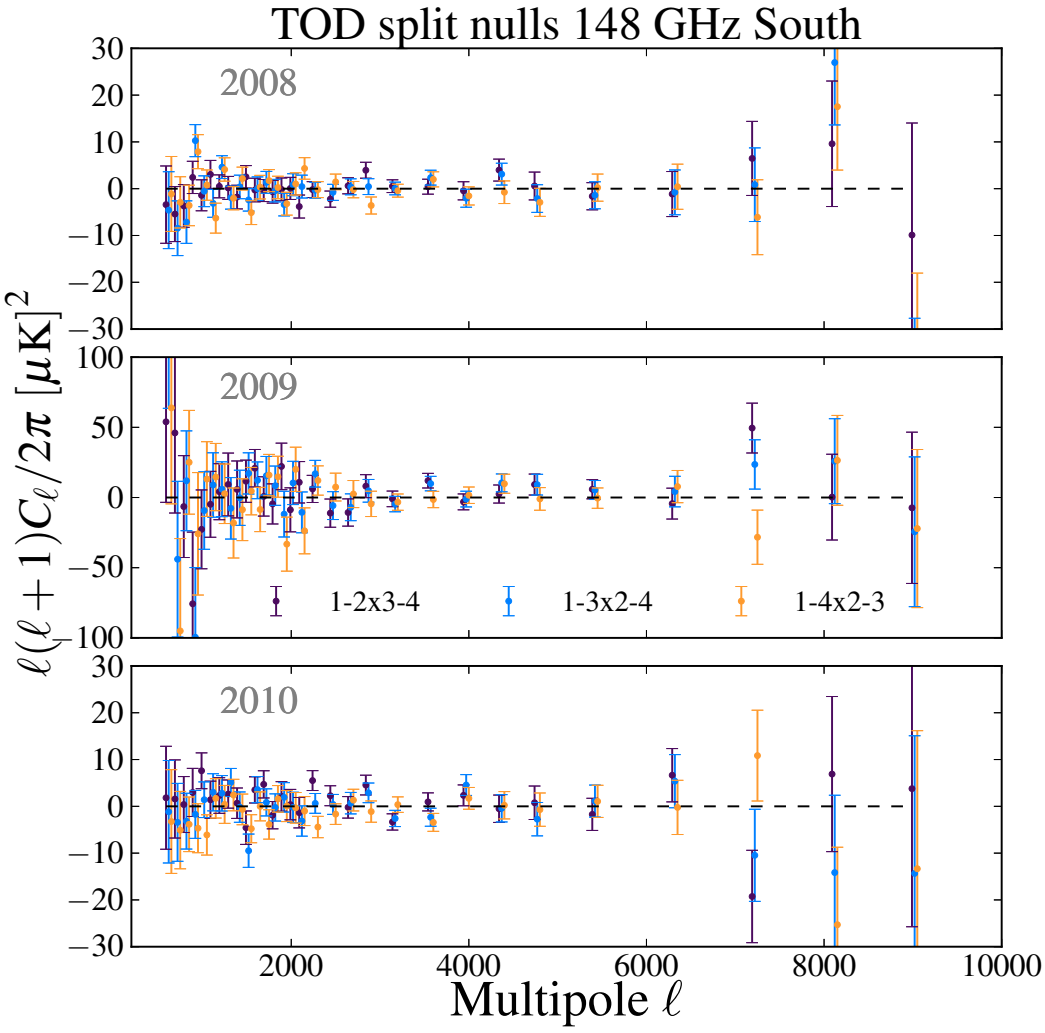

Figure 2.13: TOD null test for the 148 GHz Southern strip, from 2008 (top panel) to 2010 (bottom panel). For each year, three TOD nulls are created from the combinations described in Eq. 2.13. The χ^2 values for the null test are summarised in Table 2.2.

to construct the full power spectrum. Similarly, the azimuthal weights are borrowed from the full data spectrum run. The three difference spectra are shown in Figure 2.13 for the 148 GHz ACT-S data set. The statistics corresponding to this test are shown in Table 2.2. The spectra are found to be consistent with a null signal, as expected.

In/Out nulls

In order to test for systematic detector asymmetries, we make a map using data from detectors from the inner region of the array, and another map from detectors along the edges, and compute the differences between the two maps:

$$\begin{aligned} T_{io}^{12}(\mathbf{x}) &\equiv [T_o^1(\mathbf{x}) - T_i^2(\mathbf{x})]/2 \\ T_{io}^{34}(\mathbf{x}) &\equiv [T_o^3(\mathbf{x}) - T_i^4(\mathbf{x})]/2 \end{aligned} \tag{2.14}$$

where the i and o label the inner and outer parts of the detector array respectively. The full set of reduced χ^2 values are summarized in Table 2.3. In general we see no trend for differences as a function of detector position; the null tests are consistent with no signal.

Table 2.3: Null test χ^2 (PTE) values for the inner vs outer detectors.

Frequency	Region	Season	In/Out			dof
			(1o-2i)x(3o-4i)	(1o-3i)x(2o-4i)	(1o-4i)x(2o-3i)	
148 GHz	South	2008	26.2 (0.66)	28.2 (0.56)	26.2 (0.67)	30
		2009	37.7 (0.16)	17.3 (0.97)	27.3 (0.61)	30
		2010	34.7 (0.26)	27.3 (0.61)	25.6 (0.70)	30
	Equator	2009	49.5 (0.01)	33.3 (0.31)	45.2 (0.04)	30
		2010	35.2 (0.23)	45.8 (0.03)	39.7 (0.11)	30
218 GHz	South	2008	25.3 (0.19)	23.9 (0.24)	21.0 (0.40)	20
		2009	13.7 (0.85)	12.3 (0.91)	25.8 (0.17)	20
		2010	13.8 (0.84)	15.0 (0.78)	26.3 (0.16)	20
	Equator	2009	20.9 (0.41)	37.7 (0.01)	23.2 (0.28)	20
		2010	23.4 (0.27)	24.2 (0.24)	13.5 (0.85)	20

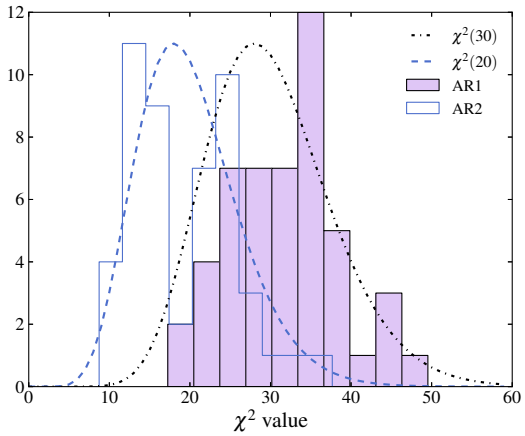

Figure 2.14: The reduced χ^2 values for all null tests. The blue histogram is computed for the χ^2 values from the 218 GHz null tests, while the purple histogram shows the same null tests for the 148 GHz maps. The black dashed and dot-dashed lines show the theoretical distributions for 20 (AR2) and 30 (AR1) degrees of freedom respectively, normalized to match the frequency of the histograms. The χ^2 values presented here are given in Tables 2.1, 2.2, 2.3 and 2.4.

Turnarounds

Another null test, based on cutting out data around telescope turnaround probes the consistency of data taken with the telescope accelerating as it reverses direction at the ends of the scan (turnarounds). In the maps used for the power spectrum estimation, the data taken during the turnaround is included. We test for any artifacts generated by the acceleration at turnaround by taking the difference of maps with and without turnaround data. Maps are made cutting data near the turnarounds, amounting to removing $\approx 10\%$ of the total data. This loss of data affects the two sky regions differently. In the southern patches, the loss of data is uniform and leads to a slight increase in striping in the maps, whereas in the equatorial patches, removing the turnarounds removes data along the declination direction in the maps. Two difference maps are made by pairing one split of the standard map with a different split of the new maps (we avoid differencing the same splits as they have very similar noise structure), and a two-way cross-power spectrum is produced. Any artifact due to the turnaround would be left in these difference maps and might produce excess power. We compute the turnaround cuts as a function of season, frequency range and area on the sky. The reduced χ^2 values are summarized in Table 2.4. Again, we find that the difference maps

have spectra consistent with no signal.

χ^2 Distribution

While the null tests are performed for different subsets of the data, we combine the statistics from the null tests together to test for consistency globally. We restrict the range of the 218 GHz spectrum to be $\ell > 1500$, hence the 218 GHz spectrum contains 20 degrees of freedom, while the 148 GHz spectrum containts 30 degrees of freedom. We show the distribution of χ^2 values and the theoretical χ^2 distribution for the two cases in Figure 2.14. This shows that the null tests are broadly consistent with being drawn from a χ^2 distribution for the number of degrees of freedom. One way to quantify this consistency would be to consider every-chi squares to be drawn from a given distribution also accounting for the correlation between chi square tests sharing common data. We could assign an error bar (and covariance) to each bins of the histogram, and look at departures from the expected distribution. Similarly we could check that the PTE follow an uniform distribution. Otherwise, one general way to attest if data points are drawn for a given distribution is to use the Kolmogorov-Smirnov test.

Isotropy

Table 2.4: Null test χ^2 values for turnarounds

Frequency	Region	Season	Turnarounds			dof
			(1t-2nt)x(3t-4nt)	(1t-3nt)x(2t-4nt)	(1t-4nt)x(2t-3nt)	
148 GHz	South	2008	21.9 (0.85)	24.8 (0.74)	34.6 (0.26)	30
		2009	28.3 (0.56)	35.3 (0.23)	26.7 (0.64)	30
		2010	30.5 (0.44)	30.4 (0.44)	35.0 (0.24)	30
	Equator	2009	27.4 (0.60)	29.3 (0.50)	34.0 (0.28)	30
		2010	35.1 (0.24)	43.9 (0.05)	21.9 (0.86)	30
218 GHz	South	2008	25.9 (0.17)	25.3 (0.19)	20.6 (0.42)	20
		2009	15.8 (0.73)	13.0 (0.88)	14.3 (0.82)	20
		2010	11.2 (0.94)	11.6 (0.93)	21.1 (0.4)	20
	Equator	2009	31.3 (0.06)	19.4 (0.5)	16.6 (0.68)	20
		2010	14.1 (0.82)	24.3 (023)	16.7 (0.67)	20

We test the isotropy of the power spectrum by estimating the power as a function of phase

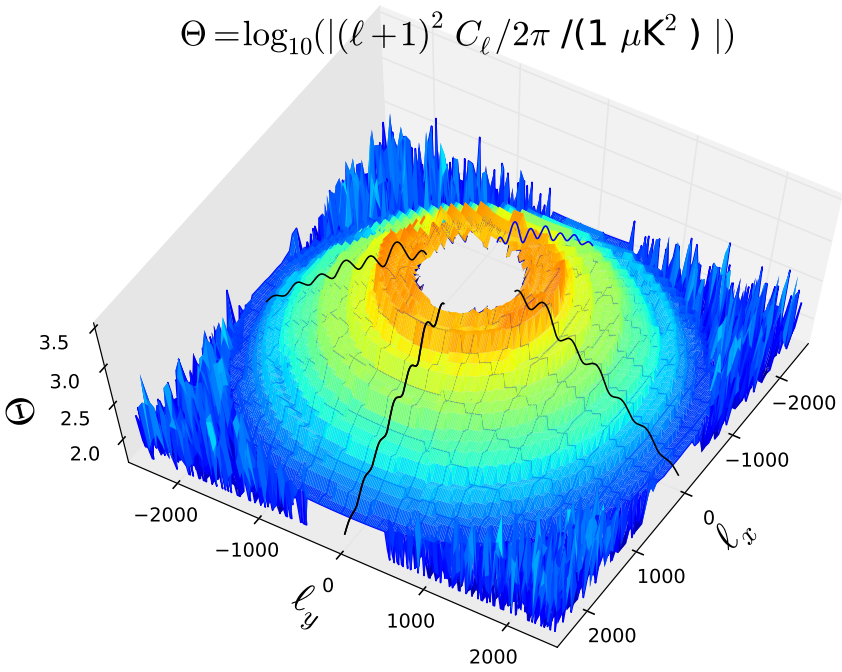

Figure 2.15: The two dimensional 148 GHz cross-power spectrum co-added across the ACT-E patches and seasons. For $\ell < 2500$ smoothing by a small kernel has been applied. The acoustic features in the power spectrum are clearly visible. At $\ell > 2500$, where the instrument noise dominates, we display the raw spectrum. The black lines represent the CMB-only theory and have been plotted to guide the eye.

$\theta = \arctan(\ell_y/\ell_x)$. We compute the inverse-noise-weighted two-dimensional spectrum co-added across patches and seasons for the ACT-E region. We show the mean two-dimensional cross-power pseudo spectrum in Figure 2.15. The spectrum is symmetric for ℓ to $-\ell$, as it is for any real valued map. To quantify any anisotropy, the power averaged over all multipoles in the range $200 < \ell < 10000$ is computed in wedges of $\theta = 20°$, and compared to the mean of the entire annulus. No significant deviation from isotropy is detected using this method. We find that this result holds for ACT-S and 218 GHz maps.

2.7.4 Consistency of ACT-E, ACT-S, and SPT spectra

As mentioned above, due to the difference in geometry of the equatorial vs. southern patches, the band power binning functions for ACT-E and ACT-S are slightly different leading small differences in the binned version of the best fit ACT + WMAP7 model (Sievers et al., 2013). Therefore to

test the consistency between ACT-E and ACT-S spectra we check for the nullity of the residuals from their corresponding binned best fit model. We also consider the consistency of the SPT band powers from Keisler et al. (2011). Care must be taken while computing the residual for the SPT spectrum as the point source masking threshold corresponding to that spectrum was different from that of ACT. To correct for this, we adjust the Poisson point source component of our best fit model to match the masking level used in Keisler et al. (2011). The results are shown in Fig. 2.16, clearly indicating that the three spectra are consistent with null, and therefore with each other.

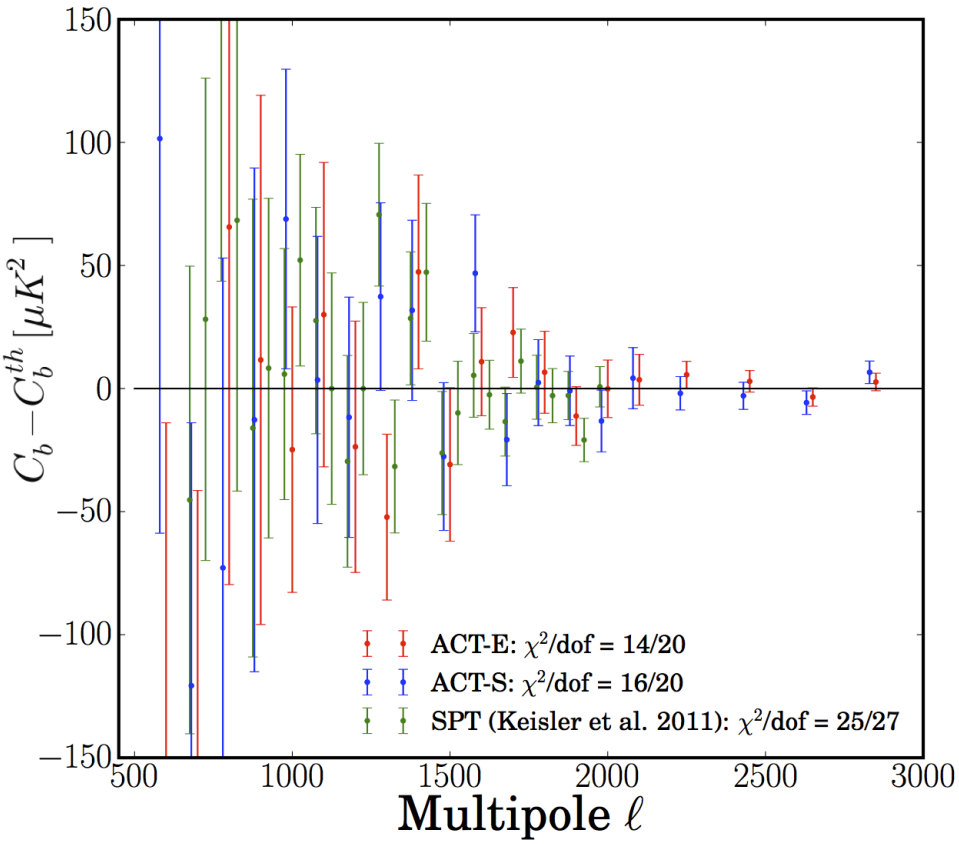

Figure 2.16: The residual power spectra obtained after subtracting the best fit ACT + WMAP model from the ACT-E, ACT-S, and SPT power spectrum (Keisler et al., 2011). For the SPT residual the Poisson point source component of the best fit model is adjusted to reflect the difference in point source masking levels between ACT and SPT. The residuals are all null showing the consistency of these spectra.

The suite of consistency tests performed here show that our reported spectrum passes a wide

range of checks for systematic errors in time, detector-space, map-space, and ℓ-space.

2.8 Discussion

We have derived the power spectrum of microwave sky maps at 148 GHz and 218 GHz produced by the Atacama Cosmology Telescope experiment. The power spectra cover a range of angular scales spanning nearly a factor of 20, ranging from around 0.35 degrees ($\ell = 590$) to a little over one arcminute ($\ell = 8900$). The maps are high quality, and in principle extracting the power spectrum is a simple matter. A host of practical considerations, along with the precision supported by the data, make estimation of the power spectrum challenging. This chapter summarizes algorithms and techniques for handling the particular shapes of our maps, point source contamination, the steepness of the power spectrum, significant features due to galactic dust emission, spatially varying noise levels, and calibration. In addition to the resulting power spectra, we also display numerous null tests on the data. These tests, along with results from simulated maps, make a strong case that any systematic errors in our power spectra are below the level of statistical error.

We combine these power spectra with the WMAP 7-year temperature and polarization power spectra in Sievers et al. (2013), and find excellent consistency with the LCDM model. We see no evidence for extra relativistic degrees of freedom[2] $N_{eff} = 2.79 \pm 0.56$, for a non zero mean spatial curvature $\Omega_k = -0.0020 \pm 0.0047$, for an early dark energy component $\Omega_e < 0.025$, or for the running of the scalar perturbation spectral index $\frac{dn_s}{d\ln k} = -0.004 \pm 0.012$. In Dunkley et al. (2013), we show that the multi-frequency spectra can be well fit by a CMB and simple foreground model. We constrain the tSZ amplitude to be $a_{\rm tSZ} = 3.4 \pm 1.4$, resulting in a constraint on the amplitude of the matter power spectrum on the scale of $8h^{-1}$ Mpc, $\sigma_8 = 0.75 \pm 0.04$. We do not detect the kSZ effect but obtain an upper limit on its amplitude $a_{\rm kSZ} < 8.6$, which can be translated into an upper limit on the duration of reionization.

The ACT power spectra are consistent with those measured by the South Pole Telescope collaboration, as are the underlying maps in a region of overlapping sky coverage. Given how small the signals are and how many sources of error must be tamed to measure them, consistent results

[2]In the standard cosmological model $N_{eff} = 3.046$ accounting for the three neutrinos species and small corrections caused by non-thermal effects during e^+-e^- annihilation.

represent a substantial experimental achievement.

The temperature power spectrum measurements displayed in Figure 2.9 represent the culmination of a two-decade quest, since the first large-angle power measurements were made by the COBE satellite (Smoot et al., 1992). It was soon realized that for inflationary cosmological models, the substantial structure in the microwave background temperature angular power spectrum due to coherent acoustic oscillations in the early universe would allow precise constraints on the basic properties of the universe (Jungman et al., 1996). A series of innovative and increasingly sensitive experiments then gradually unveiled the power spectrum. With the definitive measurements down to quarter-degree scales by the WMAP satellite (Bennett et al., 2012) and the precise arcminute-scale measurements by ACT (this work) and SPT (Story et al., 2012) along with the results from the Planck satellite, this particular route to cosmological knowledge has nearly reached its final destination.

Appendix 2.A

Here we derive an analytic expression for the expected error bars on the cross-frequency mulitseason cross-power spectrum. We denote the frequencies with uppercase A, B, C, D, the seasons with α, β, γ, τ, and the sub-season data splits with i, j, k,l. Following D11, the covariance the of cross-power spectrum is defined as:

$$\Theta_{bb}^{(\alpha A\times\beta B);(\gamma C\times\tau D)} \equiv \langle (C_{b,\alpha\beta}^{(A\times B)} - \langle C_{b,\alpha\beta}^{(A\times B)}\rangle)(C_{b,\gamma\tau}^{(C\times D)} - \langle C_{b,\gamma\tau}^{(C\times D)}\rangle)\rangle, \tag{2.15}$$

which expands as

$$\Theta_{bb}^{(\alpha A\times\beta B);(\gamma C\times\tau D)} = \frac{1}{N}\frac{1}{\nu_b^2}\sum_{i,j,k,l}^{n_d}\sum_{\ell\in b}\sum_{\ell'\in b}\left(\left[\left\langle T_{\ell,\alpha}^{*iA}T_{\ell,\beta}^{jB}T_{\ell',\gamma}^{*kC}T_{\ell',\tau}^{lD}\right\rangle\right] - \left\langle C_{b,\alpha\beta}^{(iA\times jB)}\right\rangle\left\langle C_{b,\gamma\tau}^{(kC\times lD)}\right\rangle\right) \times(1-\delta_{ij}\delta_{\alpha\beta})(1-\delta_{kl}\delta_{\gamma\tau}). \tag{2.16}$$

The Kronecker deltas remove the auto power spectra, and any same-split, same-season cross-frequency spectra. The general normalization is

$$\begin{aligned} N &= \sum_{i,j,k,l}^{n_d} (1-\delta_{ij}\delta_{\alpha\beta})(1-\delta_{kl}\delta_{\gamma\tau}) \\ &= n_d^4 - n_d^3(\delta_{\alpha\beta}+\delta_{\gamma\tau}) + n_d^2(\delta_{\alpha\beta}\delta_{\gamma\tau}). \end{aligned} \tag{2.17}$$

Applying Wick's Theorem, we have

$$\begin{aligned} \Theta_{bb}^{(\alpha A\times\beta B);(\gamma C\times\tau D)} = \frac{1}{\nu_b}\frac{1}{N}\sum_{i,j,k,l}^{n_d}\left[\left\langle C_{b,\alpha\gamma}^{iA\times kC}\right\rangle\left\langle C_{b,\beta\tau}^{jB\times lD}\right\rangle + \left\langle C_{b,\alpha\tau}^{iA\times lD}\right\rangle\left\langle C_{b,\beta\gamma}^{jB\times kC}\right\rangle\right] \\ \times(1-\delta_{ij}\delta_{\alpha\beta})(1-\delta_{kl}\delta_{\gamma\tau}), \end{aligned} \tag{2.18}$$

where

$$\left\langle C_{b,\beta\gamma}^{jB\times kC}\right\rangle = C_b + \delta_{jk}\delta_{BC}\delta_{\beta\gamma}N_b^{\beta\beta,BB}. \tag{2.19}$$

Therefore, $\Theta_{bb}^{(\alpha A\times\beta B);(\gamma C\times\tau D)}$ expands to

$$\begin{aligned} \Theta_{bb}^{1;(\alpha A\times\beta B);(\gamma C\times\tau D)} &= 2\frac{C_b^2}{\nu_b} + \frac{1}{N}\frac{C_b}{\nu_b}\sum_{i,j,k,l}^{n_d}\Big[(\delta_{ik}\delta_{AC}\delta_{\alpha\gamma}N_b^{\alpha\alpha,AA} + \delta_{jl}\delta_{BD}\delta_{\beta\tau}N_b^{\beta\beta,BB}) \\ &\quad + (\delta_{il}\delta_{AD}\delta_{\alpha\tau}N_b^{\alpha\alpha,AA} + \delta_{jk}\delta_{BC}\delta_{\beta\gamma}N_b^{\beta\beta,BB})\Big]\times(1-\delta_{ij}\delta_{\alpha\beta})(1-\delta_{kl}\delta_{\gamma\tau}) \\ &+ \frac{1}{N}\frac{1}{\nu_b}\sum_{i,j,k,l}^{n_d} N_b^{\alpha\alpha,AA}N_b^{\beta\beta,BB}(\delta_{ik}\delta_{AC}\delta_{\alpha\gamma}\delta_{jl}\delta_{BD}\delta_{\beta\tau} + \delta_{il}\delta_{AD}\delta_{\alpha\tau}\delta_{jk}\delta_{BC}\delta_{\beta\gamma})\times(1-\delta_{ij}\delta_{\alpha\beta})(1-\delta_{kl}\delta_{\gamma\tau}), \end{aligned} \tag{2.20}$$

which after some algebra reduces to

$$\begin{aligned} \Theta_{bb}^{(\alpha A\times\beta B);(\gamma C\times\tau D)} = \frac{1}{\nu_b}\Bigg(2C_b^2 + \frac{C_bN_b^{\alpha\alpha,AA}}{n_d}(\delta_{AC}\delta_{\alpha\gamma}+\delta_{AD}\delta_{\alpha\tau}) + \frac{C_bN_b^{\beta\beta,BB}}{n_d}(\delta_{BC}\delta_{\beta\gamma}+\delta_{BD}\delta_{\beta\tau}) \\ + N_b^{\alpha\alpha,AA}N_b^{\beta\beta,BB}(\delta_{AD}\delta_{\alpha\tau}\delta_{BC}\delta_{\beta\gamma}+\delta_{AC}\delta_{\alpha\gamma}\delta_{BD}\delta_{\beta\tau})\frac{n_d^2 - n_d(\delta_{\alpha\beta}+\delta_{\gamma\tau}) + n_d(\delta_{\alpha\beta}\delta_{\gamma\tau})}{n_d^4 - n_d^3(\delta_{\alpha\beta}+\delta_{\gamma\tau}) + n_d^2(\delta_{\alpha\beta}\delta_{\gamma\tau})}\Bigg) \end{aligned} \tag{2.21}$$

Therefore, with $A \neq B \neq C$ and $\alpha \neq \beta$ we have,

$$\Theta_b^{(\alpha A\times\alpha A);(\alpha A\times\alpha A)} = \frac{1}{\nu_b}\left[2C_b^2 + 4\frac{C_b}{n_d}N_b^{\alpha\alpha,AA} + 2\frac{(N_b^{\alpha\alpha,AA})^2}{n_d(n_d-1)}\right], \tag{2.22}$$

$$\Theta_b^{(\alpha A\times\alpha B);(\alpha A\times\alpha B)} = \frac{1}{\nu_b}\left[2C_b^2 + \frac{C_b}{n_d}(N_b^{\alpha\alpha,AA} + N_b^{\alpha\alpha,BB}) + \frac{N_b^{\alpha\alpha,AA}N_b^{\alpha\alpha,BB}}{n_d(n_d-1)}\right], \tag{2.23}$$

$$\Theta_b^{(\alpha A\times\alpha A);(\alpha A\times\alpha B)} = \frac{1}{\nu_b}\left[2C_b^2 + 2\frac{C_bN_b^{\alpha\alpha,AA}}{n_d}\right], \tag{2.24}$$

$$\Theta_b^{(\alpha A\times\alpha A);(\alpha B\times\alpha B)} = \frac{1}{\nu_b}\left[2C_b^2\right], \tag{2.25}$$

$$\Theta_b^{(\alpha A\times\alpha B);(\alpha A\times\alpha C)} = \frac{1}{\nu_b}\left[2C_b^2 + \frac{C_bN_b^{\alpha\alpha,AA}}{n_d}\right], \tag{2.26}$$

$$\Theta_b^{(\alpha A\times\beta A);(\alpha A\times\beta B)} = \frac{1}{\nu_b}\left[2C_b^2 + \frac{C_bN_b^{\alpha\alpha,AA}}{n_d}\right], \tag{2.27}$$

$$\Theta_b^{(\alpha A\times\beta A);(\alpha B\times\beta B)} = \frac{1}{\nu_b}\left[2C_b^2\right], \tag{2.28}$$

$$\Theta_b^{(\alpha A\times\beta B);(\alpha A\times\beta C)} = \frac{1}{\nu_b}\left[2C_b^2 + \frac{C_bN_b^{\alpha\alpha,AA}}{n_d}\right]. \tag{2.29}$$

Appendix 2.B

We can also include the effect of an uncertainty on the beam when combining data between different seasons. We consider the covariance of the power spectrum for two season pairs: $i \times j$ and $k \times l$, with beam window functions $w_b^{i\times j} = B_b^iB_b^j$ and $w_{b'}^{k\times l} = B_{b'}^kB_{b'}^l$, respectively. The measured windows function is given by $w_b^{obs} = w_b + \delta w_b$. This error propagates to the power spectrum covariance as

$$\langle\frac{w_b^{i\times j}C_b^{i\times j}}{w_b^{i\times j}+\delta w_b^{i\times j}}\frac{w_{b'}^{k\times l}C_{b'}^{k\times l}}{w_{b'}^{k\times l}+\delta w_{b'}^{k\times l}}\rangle \rightarrow \frac{C_b^{i\times j}}{w_b^{i\times j}}\frac{C_{b'}^{k\times l}}{w_{b'}^{k\times l}}\langle\delta w_b^{i\times j}\delta w_{b'}^{k\times l}\rangle. \tag{2.30}$$

The error on the window function is related to the error of the beam by

$$\delta w_b^{i\times j} = \delta B_b^iB_b^j + B_b^i\delta B_b^j. \tag{2.31}$$

Chapter 3

The Atacama Cosmology Telescope: Cross Correlation with *Planck* maps

3.1 Introduction

We present a measurement of the cross-correlation of CMB temperature anisotropies at 148 GHz and 218 GHz, from the ACT data acquired during the 2008, 2009 and 2010 observing seasons, with the publicly released *Planck* maps at 143 GHz and 217 GHz. The overlap of the two experiments allows us to test their consistency. The ACT data used in the previous analysis were calibrated to *WMAP* data by matching the ACT$\times$*WMAP* cross-spectrum to the ACT power spectrum (at 2% precision for ACT 148 GHz; Hajian et al., 2011). The lower level of noise, higher resolution, and closer match in frequency of the *Planck* satellite data now enable a more precise calibration.

The Chapter is organized as follows. In Section 3.2 we describe the observations, beam transfer function and mask used in the cross-correlation analysis. In Section 3.3 we show the ACT$\times$*Planck* power spectra for each ACT season and each frequency, and use a simple likelihood to assess the consistency with the ACT power spectra and to compute a best-fit calibration factor. In Section 3.4, we compute new estimates of the Galactic cirrus contamination and Cosmic Infrared Background (CIB) fluctuations in ACT maps using the 353 GHz *Planck* data. In Section 3.5 we test the isotropy of the best fit calibration, by comparing the ACT two-dimensional power spectra to the ACT $\times$

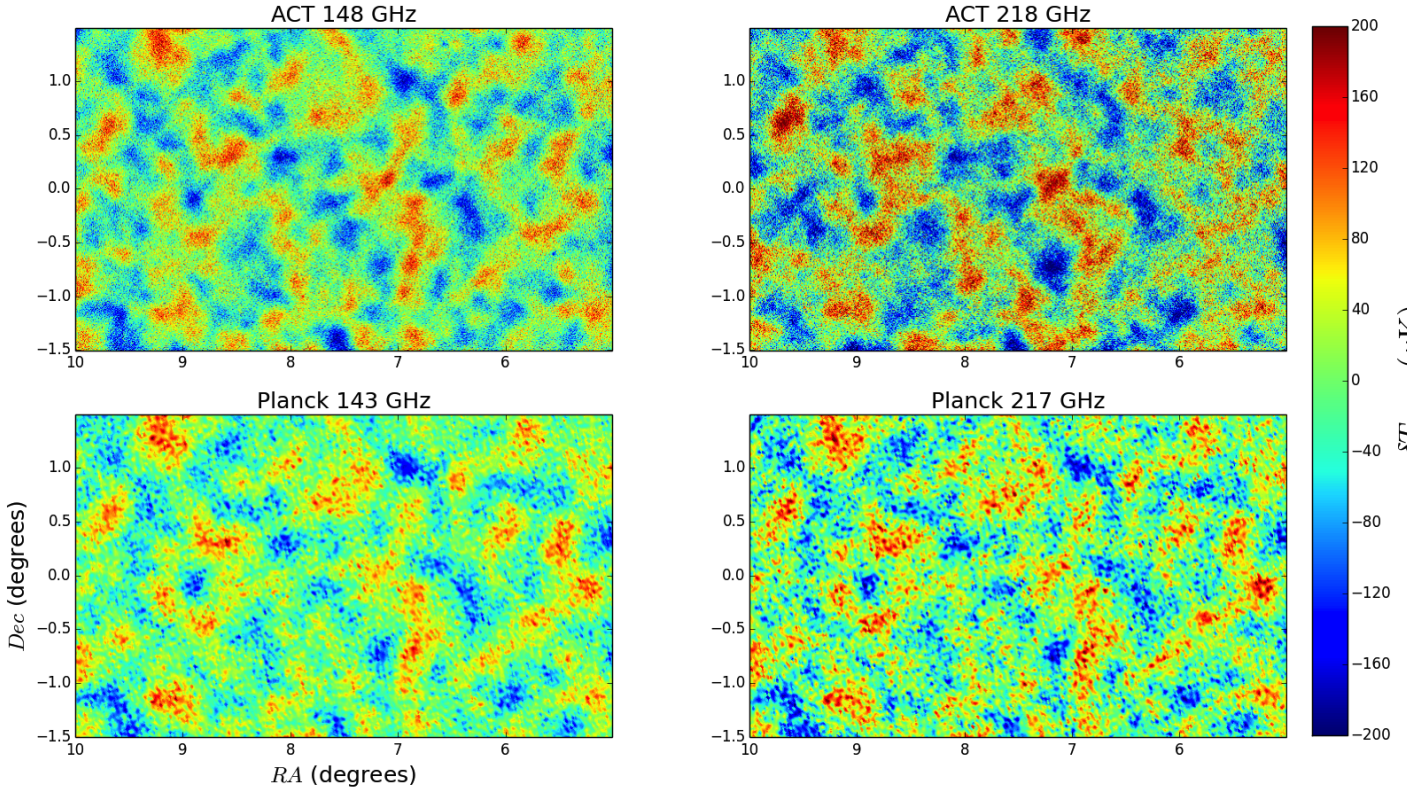

Figure 3.1: Comparison of ACT (*top*) and *Planck* (*bottom*) maps for a 15 deg^2 patch in the ACT Equatorial region. The maps are the inverse variance weighted combination of all ACT data at 148 GHz (*left*) and 218 GHz (*right*) and all *Planck* data at 143 GHz and 217 GHz. All maps have been filtered with a high pass filter (for modes on scales: $\ell < 500$). Artifacts of the HEALpix pixelization are seen in the *Planck* maps. The agreement is visually excellent.

Planck two-dimensional spectra. We conclude in Section 3.6.

In this Chapter we take as a baseline the maps presented in Chapter 2. These maps were calibrated to *WMAP* as in Hajian et al. (2011). Recalibration factors y quoted in the following are values by which one multiplies the ACT maps. That is, a recalibration factor of 1.01 means multiply the ACT map by 1.01 and increase the power spectrum by $(1.01)^2$. Note that the observed map calibration factor between *Planck* and *WMAP* maps is 0.985 (*Planck* is lower than *WMAP*; Planck Collaboration XVI (2013)); this sets our expectation for the ACT calibration to Planck.

3.2 ACT and Planck data

The data used in this Chapter are described in Chapter 2 of this thesis and consist of maps of 300 deg^2 along the celestial equator (ACT-E) and 292 deg^2 along declination -55° in the southern sky (ACT-S). We consider two seasons of data (2009, 2010) for ACT-E and one season of data (2008) for ACT-S (as these have the highest signal to noise ratio). For cross-correlating with *Planck*, the data within each season are divided into two splits in time, each of which is cross-linked, allowing direct estimation of the noise power spectra of the maps. For *Planck* we use the 'half-ring' maps from the public data release. Each frequency channel has two half-ring maps, built using only the first or the second half of the stable pointing period data. We project *Planck*'s galactic-coordinate HEALPix maps to patches of ACT's cylindrical equal area pixels in equatorial coordinates using the Taylor interpolation scheme described in Næss & Louis (2013).

Figure 3.1 depicts a subset of the maps used in this analysis. To account for the instrument resolution, we use the ACT beam transfer functions presented in Hasselfield et al. (2013), and for *Planck* we use the publicly released effective transfer functions (Planck Collaboration VII, 2013). The spatial variations of the *Planck* beam transfer functions across the sky result in effects that are significantly smaller than the statistical uncertainty in the calibration factors, and so will be ignored in this analysis. We use the ACT masks presented in Chapter 2, including a point source mask in both the ACT-S and ACT-E regions with flux cut of 15 mJy at 148 and 218 GHz, and a Galactic cirrus mask in the ACT-E region. Because the Planck beams are significantly broader than the ACT beams, point sources will appear larger in *Planck* maps than in ACT maps. We test the effect of widening the ACT mask by 50% and find that our results are stable at the 0.2 σ level. The *Planck* HFI channels at 100–353 GHz are calibrated on the dipole due to the Sun's motion relative to the CMB, leading to an absolute calibration uncertainty of 0.54 percent for the 100, 143, and 217 GHz channels, with relative calibrations of 0.2 percent between them (Planck Collaboration VIII, 2013).

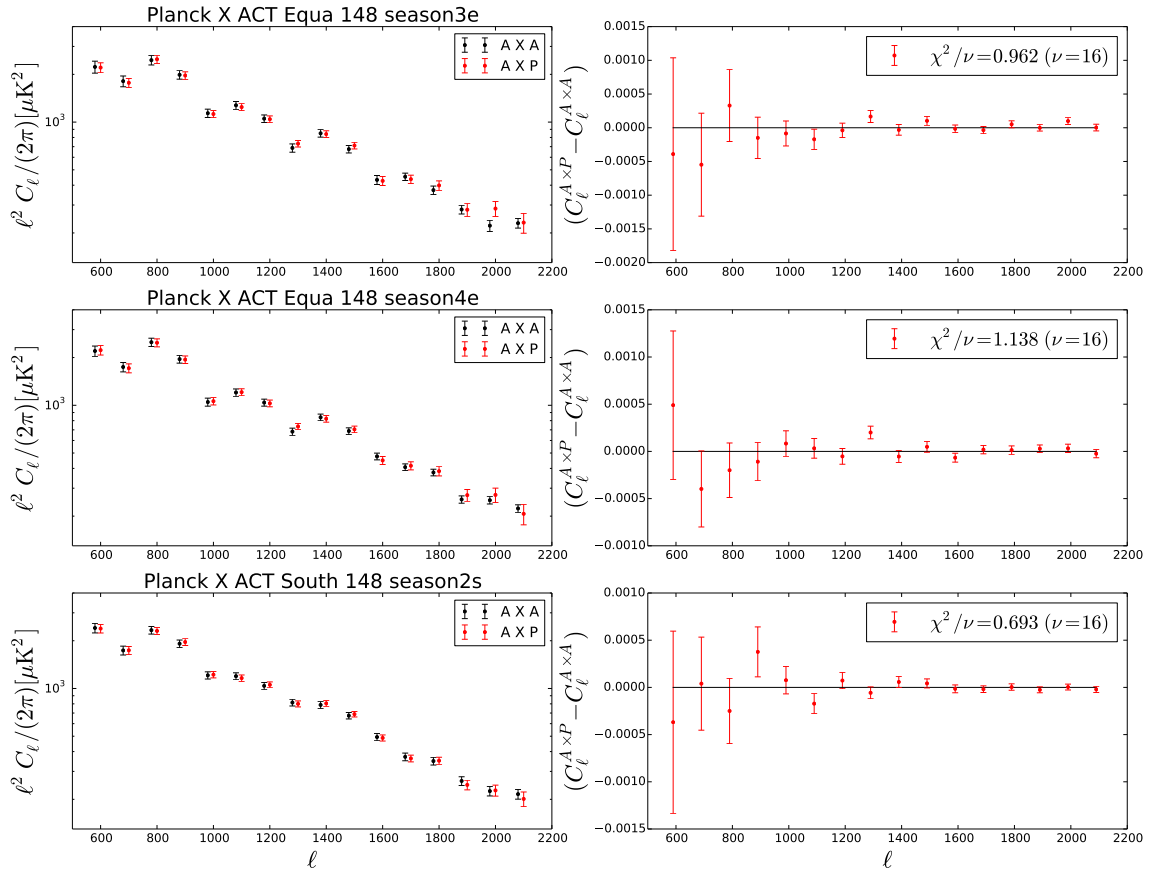

Figure 3.2: *Left:* The recalibrated cross-correlation between ACT at 148 GHz and *Planck* at 143 GHz (A×P), compared to the recalibrated ACT power spectra (A×A), in the overlapping angular range. *Right:* Residuals between the cross and auto-spectra as a function of scale. No significant features are observed. Since data for each experiment in each plot come from the same sky region, the errors on the residuals do not include cosmic variance. Note also that the ordinates of the residual plots are not multiplied by the $\sim \ell^2$ factor used for plotting angular power spectra.

3.3 Cross Correlations

We compute the ACT 148 GHz × *Planck* 143 GHz, and the ACT 218 GHz × *Planck* 217 GHz power spectra, for each ACT season. We follow the same procedure described in Chapter 2, including prewhitening of the maps, filtering, and deconvolving the effects of the beam, pixelization, and windowing. The uncertainties on the spectra are calculated analytically using measurements of the noise in the maps and include beam uncertainties (see Appendix 3.A).

We allow a single degree of freedom for the comparison between the cross-spectra and the ACT spectra, namely a calibration factor that rescales the ACT power spectra to match the cross-spectra. We note that the shift in the effective frequency between the two experiments leads to a negligible variation in the foreground level. The calibration, y, is obtained for each frequency and ACT season and region by minimizing the χ^2 defined as

$$\chi^2(y) = \boldsymbol{r}^t \boldsymbol{\Sigma}^{-1} \boldsymbol{r}. \tag{3.1}$$

Here $\boldsymbol{r} = \boldsymbol{C}^{A\times P} - y\boldsymbol{C}^{A\times A}$ is the residual between the cross and auto-spectra, which removes cosmic variance uncertainty, and $\boldsymbol{\Sigma}$ is the covariance matrix of the residual (Appendix 3.A). This factor y is relative to the original *WMAP* calibration used in the Chapter 2 analysis, and can then be used to rescale the ACT maps. The calibrated power spectra for each season and region, together with the residuals, are shown in Figures 3.2 and 3.3 for the substantial range of angular scales common to both experiments. Doing this comparison in power spectra space instead of maps space allows us to check for any ℓ dependent bias. An effect due to a transfer function at low multipole or to the beam at high multipoles could in principle induce systematic differences between the two experiments.

We find the signal to be consistent at both frequencies and in both regions of the sky, with the probability to exceed (PTE) and the calibration factors reported in Table A. The PTEs for all the spectra lie in the range $0.213 < \mathrm{PTE} < 0.874$, and there are no particular features seen in the residual spectra. We compare the ACT re-calibration factors to those determined by the *Planck* collaboration by jointly fitting the ΛCDM cosmological model to the ACT and full-sky *Planck* power spectra (Planck Collaboration XVI, 2013). They are reported there as $y_{148}^{\mathrm{ACTe}}, y_{148}^{\mathrm{ACTs}}, y_{218}^{\mathrm{ACTe}}, y_{218}^{\mathrm{ACTs}}$,

TABLE A
PROBABILITIES TO EXCEED AND CALIBRATION FACTORS

Freq	Season	χ^2/ν	P.T.E	y (this work)	y (model[a])	y_w (model[b])
148	3e	0.962	0.49	0.980 ± 0.008		
	4e	1.138	0.31	0.989 ± 0.006		
	ACT-E				0.988 ± 0.007	1.009 ± 0.008
	ACT-S[c]	0.693	0.804	0.998 ± 0.0065	0.992 ± 0.007	1.011 ± 0.008
218	3e	0.803	0.683	0.957 ± 0.034		
	4e	1.26	0.213	0.969 ± 0.02		
	ACT-E				0.96 ± 0.01	0.99 ± 0.01
	ACT-S	0.616	0.874	1.001 ± 0.025	1.01 ± 0.01	1.04 ± 0.02

[a]From Planck Collaboration XVI (2013).
[b] Re-calibration factors obtained by jointly fitting the ΛCDM cosmological model to the ACT and full-sky *WMAP* 9 years power spectra.
[c]ACT-S includes just the correlation with the 2008 maps.

and are repeated in Table A for comparison. The two methods give consistent results. For completeness, we also report the re-calibration factors obtained by jointly fitting the ΛCDM cosmological model to the ACT and full-sky *WMAP* 9 years power spectra. The difference between the *Planck* and *WMAP* calibration is consistent with our expectation.

3.4 Galactic dust and CIB using *Planck* 353 Ghz

The 353 GHz *Planck* maps can be modeled as the sum of CMB, Galactic cirrus dust and CIB fluctuations. Figure 3.4 shows the difference between the measured *Planck* 353 GHz and ACT 148 GHz power spectra for the equatorial and southern surveys. Since the dust emission is inhomogeneous, we use the ACT spatial weighting scheme when computing the *Planck* 353 GHz power spectrum, each pixel being weighted by the number of times it was observed. The difference between the two power spectra is dominated by Galactic cirrus and CIB fluctuation emissions at 353 GHz. The contribution from other signals, such as the Sunyaev Zel'dovich effect, is subdominant and can be safely neglected.

Figure 3.4 also shows predictions and error bands for the sum of the CIB and cirrus contributions

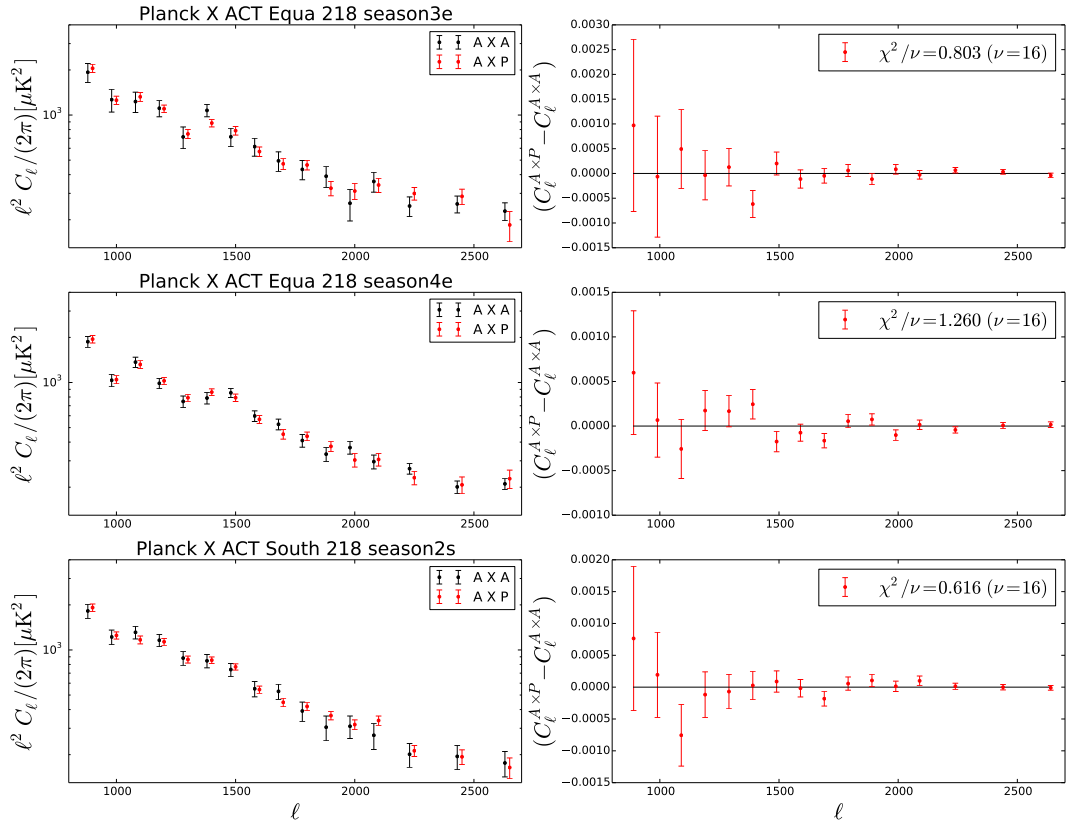

Figure 3.3: As in Figure 3.2, for the correlation between ACT at 218 GHz and *Planck* at 217 GHz.

at 353 GHz. We estimate the Poisson and clustered CIB contribution at 353 GHz based on the ACT constraints from Table 2 of Dunkley et al. (2013).

Following Addison et al. (2012), the CIB power spectrum is modeled as the square of a modified blackbody in flux density units with emissivity index constrained to be $\beta = 2.2 \pm 0.1$, with a fixed effective temperature of $T = 9.7$ K. As can be seen in Figure 17 of the Planck Collaboration XXX (2013) paper, the 2013 Planck CIB model is $\sim 30\%$ higher than the early Planck 217 GHz CIB bandpowers that were used to constrain the Addison et al. (2011) model. We renormalize the Addison et al. model by multiplying the 353 GHz prediction by a factor of 1/1.3.

The Galactic dust power at 353 GHz was calculated using a modified blackbody with emissivity index $\beta = 1.5$ and temperature $T = 20$ K, consistent with submillimeter analysis of cirrus in a similar region of sky along the celestial equator (Bracco et al., 2011), and with observations from

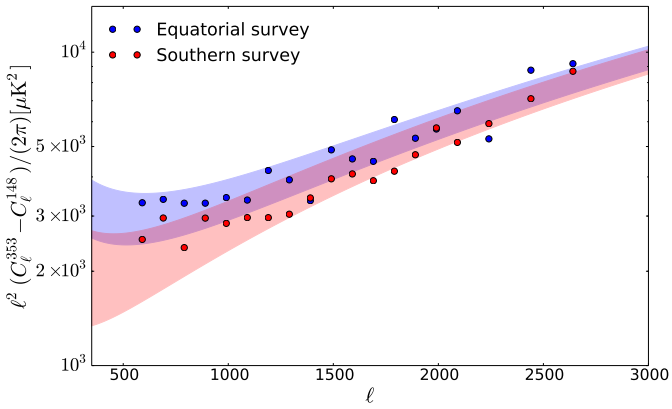

Figure 3.4: Difference between the measured *Planck* 353 GHz and ACT 148 GHz power spectra for the equatorial and southern surveys (dots). The colored bands represent the 1σ prediction for the Galactic dust and CIB amplitude based on the extrapolation of the ACT foreground power spectra modeling at 148 and 218 GHz for the equatorial (blue) and southern surveys (red) (Dunkley et al., 2013).

the Planck satellite (Planck Collaboration XI, 2013). We correct the Galactic and CIB power calculated at the nominal frequency, 353 GHz, for the bandpass profile and response to a dust-like source SED (Planck Collaboration IX, 2013). The uncertainties shown in Figure 3.4 are dominated by uncertainty in the CIB and Galactic dust amplitudes measured by ACT (Dunkley et al., 2013). We interpret the figure as showing that the ACT dust model and measurements are in agreement with *Planck*'s measurement at 353 GHz.

3.5 Isotropy of the two-dimensional power spectra

Because of its scan strategy, ACT has anisotropic noise. While the map-making algorithm should not produce any anisotropy in the map or the transfer function, the *Planck* data provide an opportunity to test the ACT maps by checking for any directional dependence in the calibration factor. Excess noise along and perpendicular to the ACT scan directions leads to X shaped patterns of high noise regions in the ACT two-dimensional power spectra. These features have been down-weighted accordingly using azimuthal weights in the D13 analysis. *Planck* data do not suffer from such artifacts and the effects due to the scanning strategy of ACT become subdominant in the cross-

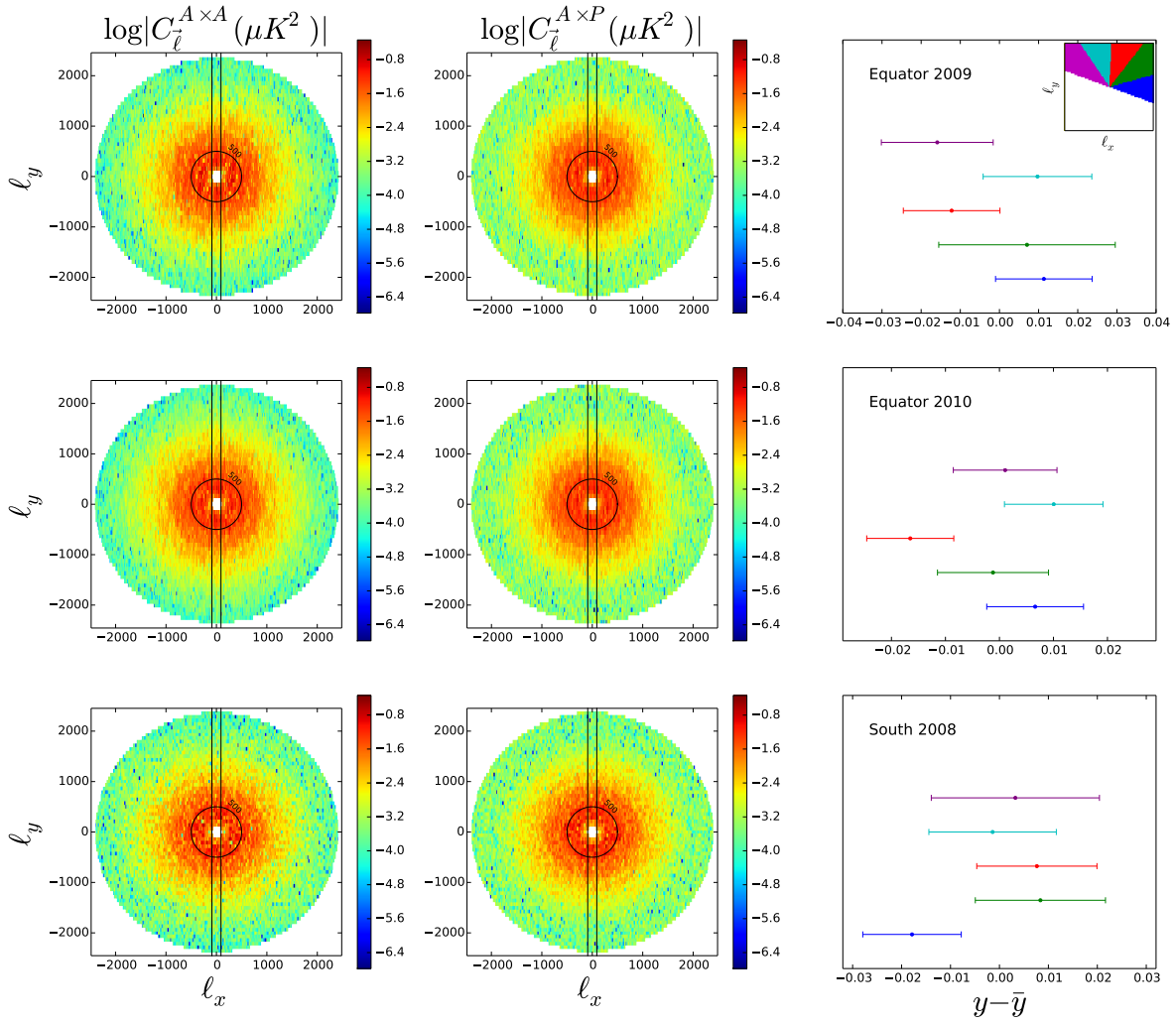

Figure 3.5: Two-dimensional ACT×ACT power spectra (left) and ACT×*Planck* (middle) in the overlapping angular range. The vertical bands show the fourier mask applied to the ACT spectra to avoid artifacts of the scanning strategy and the black circles encompass the $\ell < 500$ modes that are not used in the power spectra analysis. *Right:* calibrations as a function of the angular bands, from which we have subtracted their mean. No significant anisotropy is detected.

spectra. We compare the two-dimensional power spectra of ACT and ACT × *Planck* in order to assess the isotropy of the deduced calibration parameter. We compute the two-dimensional power spectra following the same procedure as for the one-dimensional analysis, except that we do not deconvolve the effect of the window function, because the inversion of the un-binned mode coupling matrices is too computationally intensive. We divide the two-dimensional power spectrum into five different angular wedges, of 36° each, using the symmetry $\ell \rightarrow -\ell$ of the power spectra. We then bin the power spectra using the same bin size as for the one-dimensional power spectra and compute the expected variance in each bin using Monte-Carlo simulations. Finally, we compute the best-fit calibration number for each angular bin. We do not detect any significant anisotropy in the two-dimensional power spectra. The best-fit calibration per angular bin as well as the two-dimensional power spectra are shown in Figure 3.5 and Figure 3.6.

3.6 Conclusion

The ACT experiment has mapped two regions of the sky covering 592 deg^2 at arcminute resolution. The same regions have now been observed by the *Planck* satellite, and we have computed the cross-correlation to check for consistency between the data sets. The cross-comparison also tests the beams and transfer functions of both experiments. The cross-power is consistent at all angular scales probed by both experiments, and at both frequencies observed by ACT. We have estimated new calibration factors for ACT at higher precision by using the *Planck* data in place of *WMAP*. The isotropy of the calibration factor implies that the ACT scan strategy did not introduce anisotropies into the maps. We have also measured the *Planck* 353 GHz power spectrum in the ACT equatorial and southern surveys region, and found the amplitudes of the dust and CIB to be consistent with those measured by ACT. Overall the agreement between the two measurements is excellent.

Appendix 3.A

The total covariance matrix $\mathbf{\Sigma}$ of the residual $C_b^{A\times A} - C_b^{A\times P}$ is a sum of two terms. The first accounts for the noise in ACT and *Planck* and the second accounts for the beam uncertainties:

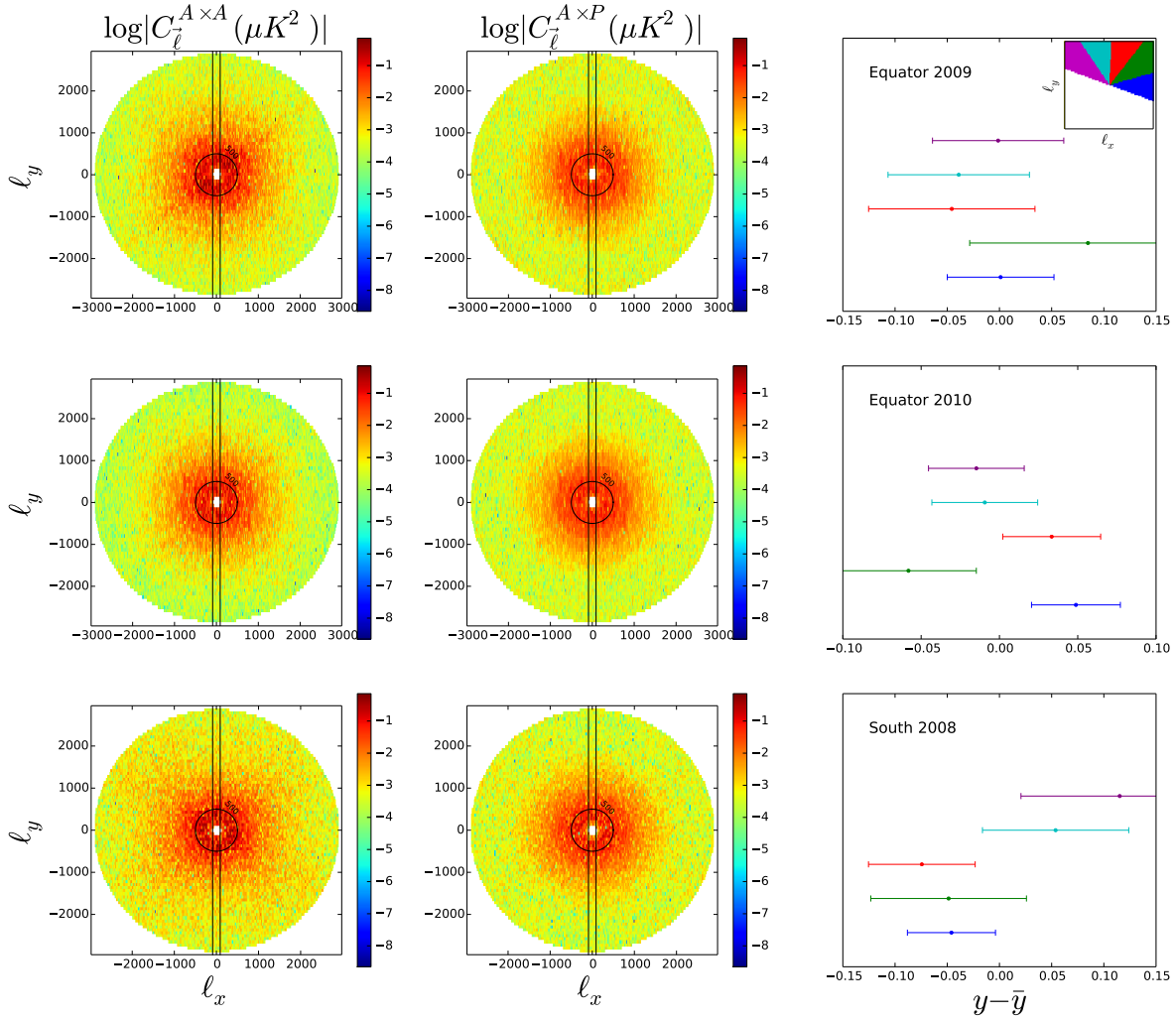

Figure 3.6: As in Figure 3.5, for the correlation between ACT at 218 GHz and *Planck* at 217 GHz. Here the absolute value emphasize the X shaped patterns.

$\mathbf{\Sigma} = \mathbf{\Sigma}_n + \mathbf{\Sigma}_{\rm beam}$. The noise term is given by

$$\mathbf{\Sigma}_n = \left\langle (C_b^{A\times A} - C_b^{A\times P})(C_b^{A\times A} - C_b^{A\times P}) \right\rangle \;=\; \Theta_b^{(A\times A);(A\times A)} + \Theta_b^{(A\times P);(A\times P)} - 2\Theta_b^{(A\times A);(A\times P)} \tag{3.2}$$

Each of the terms can be computed analytically:

$$\Theta_b^{(A\times A);(A\times A)} = \frac{1}{\nu_b}\left[2C_b^2 + 4\frac{C_b}{n_d}N_b^{AA} + 2\frac{(N_b^{AA})^2}{n_d(n_d-1)}\right] \tag{3.3}$$

$$\Theta_b^{(A\times P);(A\times P)} = \frac{1}{\nu_b}\left[2C_b^2 + \frac{C_b}{n_d}(N_b^{AA} + N_b^{PP}) + \frac{N_b^{AA}N_b^{PP}}{n_d^2}\right] \tag{3.4}$$

$$\Theta_b^{(A\times A);(A\times P)} = \frac{1}{\nu_b}\left[2C_b^2 + 2\frac{C_b N_b^{AA}}{n_d}\right], \tag{3.5}$$

where n_d is the number of data splits and ν_b is the number of modes per bin, corrected for the effect of the window function. C_b is a theoretical power spectrum, and N_b^{XX} is the noise power spectrum, given by $C_{b,\,\rm auto}^{XX} - C_{b,\,\rm cross}^{XX}$. Finally the full covariance is given by

$$\left\langle (C_b^{A\times A} - C_b^{A\times P})(C_b^{A\times A} - C_b^{A\times P}) \right\rangle = \frac{1}{\nu_b}\left[2\frac{(N_b^{AA})^2}{n_d(n_d-1)} + \frac{C_b}{n_d}(N_b^{PP} + N_b^{AA}) + \frac{N_b^{AA}N_b^{PP}}{n_d^2}\right]. \tag{3.6}$$

Chapter 4

Lensing Simulation and Power Spectrum Estimation for High Resolution CMB Polarization Maps

4.1 Introduction

The new generation of CMB experiments are focused on measuring the polarization of the CMB. The anisotropies are only ∼10% polarized so an accurate measurement of the polarization power spectrum is challenging. A number of ground-based experiments are targeting this signal, with POLARBEAR (Kermish et al., 2012), SPTpol (Austermann et al., 2012), and ACTPol (Niemack et al., 2010) designed to measure scales of a few arcminutes or less. These experiments aim to constrain the cosmological model by measuring the 'E-mode' power spectrum that provides an independent probe of the scalar modes measured through the temperature fluctuations, and by measuring the 'B-modes' generated due to the gravitational lensing of E-modes by the dark matter distribution along the line-of-sight. These lensing B-modes are generated at small scales, and are more easily accessible to high resolution ground-based telescopes than the larger scale primordial B-modes directly sourced by gravitational waves.

In this Chapter we describe the estimation of E and B-mode power spectra from realistic obser-

vations of the CMB sky. The number of pixels for high resolution experiments is of order $\approx 10^7$, so a direct maximum likelihood method is computationally too expensive. Instead we rely on pseudo C_ℓ estimators (Bond et al., 1998). One of the main challenges in estimating the pseudo B-mode power spectrum arises since the E and B mode decomposition of the polarization field on a incomplete sky induces leakage between the two modes. The discontinuity at the edges of the map mixes E and B modes, increasing the variance of the B-mode power spectrum. Smith (2006) and Smith & Zaldarriaga (2007) provide a general solution to this problem by defining a pure B-mode power spectrum estimator that is not contaminated by this mixing. In Section 4.2, we adapt their algorithm for flat sky maps, and demonstrate that the algebra simplifies considerably under the flat-sky approximation.

In Section 4.3, we introduce a novel technique for generating high resolution lensed CMB maps. Different methods have been proposed to do this, often using a remapping between pixels (Lewis, 2005) and an interpolation scheme. We present a hybrid method that combines pixel remapping and a Taylor series decomposition of the lensed field. In Section 4.4, we use simulated observations from the ACTPol experiment to generate non-uniform realizations of the experimental noise. We then test our lensing simulation and power spectrum estimation method, and its optimality, using Monte Carlo simulations.

4.2 E/B leakage in the flat sky approximation

In this section we review the issue of leakage of power between polarization types due to incomplete sky coverage. This issue has been discussed in previous studies targeting observations over large areas (e.g., Lewis et al., 2002; Smith, 2006; Smith & Zaldarriaga, 2007; Grain et al., 2009; Cao & Fang, 2009; Zhao & Baskaran, 2010; Bunn, 2011; Bowyer et al., 2011; Grain et al., 2012). We demonstrate how the 'pure' estimators of the different polarization types can be applied in the flat-sky approximation, relevant to small patches of the sky.

4.2.1 Notation

We have shown in Chapter 1 that defining the polarization tensor

$$P_{ab}(\mathbf{x}) = \frac{1}{2}\begin{pmatrix} Q(\mathbf{x}) & U(\mathbf{x}) \\ U(\mathbf{x}) & -Q(\mathbf{x}) \end{pmatrix}, \tag{4.1}$$

we can express the E and B modes as

$$\begin{aligned} P_{ab}(\mathbf{x}) &= \frac{1}{\sqrt{2}}\int d\boldsymbol{\ell} E(\boldsymbol{\ell})({}^{E}e^{i\boldsymbol{\ell}\mathbf{x}})_{ab} + B(\boldsymbol{\ell})({}^{B}e^{i\boldsymbol{\ell}\mathbf{x}})_{ab}, \\ E(\boldsymbol{\ell}) &= \frac{2}{\ell^2}\int d^2x P_{ab}(\mathbf{x})\mathcal{E}^{ab}(e^{-i\boldsymbol{\ell}\mathbf{x}}), \\ B(\boldsymbol{\ell}) &= \frac{2}{\ell^2}\int d^2x P_{ab}(\mathbf{x})\mathcal{B}^{ab}(e^{-i\boldsymbol{\ell}\mathbf{x}}). \end{aligned} \tag{4.2}$$

Or equivalently $E(\boldsymbol{\ell}) \pm iB(\boldsymbol{\ell}) = e^{\mp 2i\phi_{\boldsymbol{\ell}}}(Q(\boldsymbol{\ell}) \pm iU(\boldsymbol{\ell}))$.

4.2.2 Partial sky coverage

Observations with modern high resolution experiments are typically performed on a small fraction of the sky, of area Ω (e.g., Story et al., 2012; Das et al., 2013). The observed region can be described by a window function

$$W(\mathbf{x}) = \begin{cases} w(\mathbf{x}) & \text{if} \quad \mathbf{x} \in \Omega \\ 0 & \text{otherwise} \end{cases} \tag{4.3}$$

which modifies the observed Q and U components such that $\tilde{Q}(\mathbf{x}) = W(\mathbf{x})Q(\mathbf{x})$ and $\tilde{U}(\mathbf{x}) = W(\mathbf{x})U(\mathbf{x})$. Propagating the effects of the window function into the $\tilde{E}$ and $\tilde{B}$ modes calculated as in Eqn. 4.2, the window functions mix E and B modes to give the modified modes

$$\begin{aligned} \tilde{E}(\boldsymbol{\ell}) &= \int d\boldsymbol{\ell'} W(\boldsymbol{\ell} - \boldsymbol{\ell'})[E(\boldsymbol{\ell'})\cos 2(\phi_{\boldsymbol{\ell'}} - \phi_{\boldsymbol{\ell}}) - B(\boldsymbol{\ell'})\sin 2(\phi_{\boldsymbol{\ell'}} - \phi_{\boldsymbol{\ell}})], \\ \tilde{B}(\boldsymbol{\ell}) &= \int d\boldsymbol{\ell'} W(\boldsymbol{\ell} - \boldsymbol{\ell'})[E(\boldsymbol{\ell'})\sin 2(\phi_{\boldsymbol{\ell'}} - \phi_{\boldsymbol{\ell}}) + B(\boldsymbol{\ell'})\cos 2(\phi_{\boldsymbol{\ell'}} - \phi_{\boldsymbol{\ell}})]. \end{aligned} \tag{4.4}$$

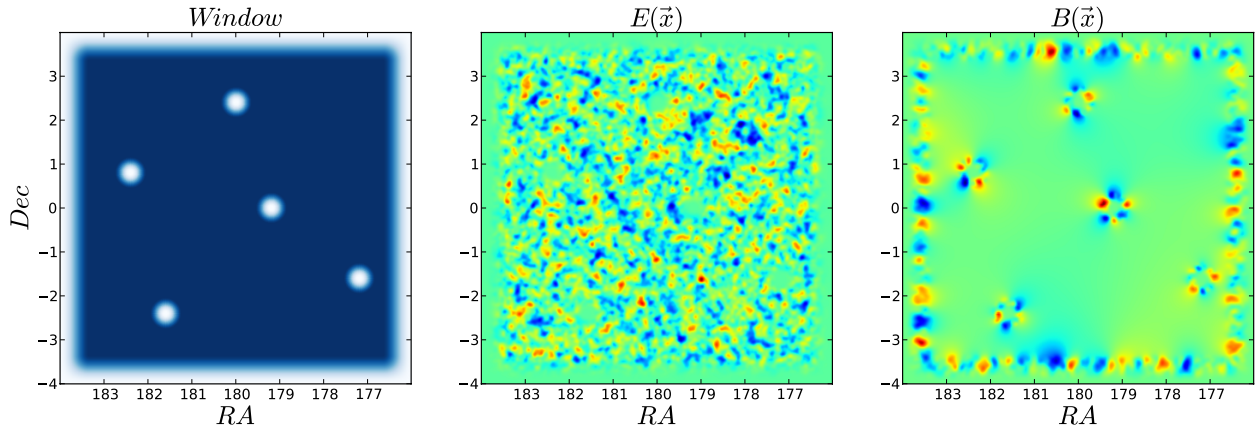

Figure 4.1: **Effect of sky cuts on the polarization pattern.** A pure E-mode signal on the sky is observed through a window with a point source mask (left) leading to the estimated E-mode (centre) and B-mode (right) maps. The leaked E-modes show up as spurious signal in the B-mode map localized around the discontinuities of the window function.

The power spectra of these modified modes are then (See Appendix 4.A)

$$\langle \tilde{E}(\boldsymbol{\ell})\tilde{E}^*(\boldsymbol{\ell})\rangle = \int d\boldsymbol{\ell'}|W(\boldsymbol{\ell}-\boldsymbol{\ell'})|^2[C_{EE}(\ell')\cos^2 2(\phi_{\boldsymbol{\ell'}}-\phi_{\boldsymbol{\ell}}) + C_{BB}(\ell')\sin^2 2(\phi_{\boldsymbol{\ell'}}-\phi_{\boldsymbol{\ell}})],$$
$$\langle \tilde{B}(\boldsymbol{\ell})\tilde{B}^*(\boldsymbol{\ell})\rangle = \int d\boldsymbol{\ell'}|W(\boldsymbol{\ell}-\boldsymbol{\ell'})|^2[C_{EE}(\ell')\sin^2 2(\phi_{\boldsymbol{\ell'}}-\phi_{\boldsymbol{\ell}}) + C_{BB}(\ell')\cos^2 2(\phi_{\boldsymbol{\ell'}}-\phi_{\boldsymbol{\ell}})]. \quad (4.5)$$

Since C_{EE} is expected to be an order of magnitude larger than C_{BB}, this mixing therefore leads to significant contamination of the B-modes by the leaked-in E-modes. This is illustrated in Figure 4.1, which also highlights that the leakage is localized close to the edges of the map, or to the edges of holes due to masking of bright point sources. This leakage will increase the variance of the measured C_{BB}, even when an unbiased estimator is constructed for C_{BB} and C_{EE} by inverting the convolutions.

4.2.3 Pure estimators

A solution to the problem of E/B mixing has been proposed by Smith (2006); Smith & Zaldarriaga (2007). Rather than deconvolving $E(\ell)$ and $B(\ell)$, the window function can be included directly in

the projection operator (Eqn. 4.2), such that

$$E^{pure}(\boldsymbol{\ell}) = \frac{2}{\ell^2}\int d^2x P^{ab}(\mathbf{x})\mathcal{E}_{ab}(W(\mathbf{x})e^{-i\boldsymbol{\ell}\mathbf{x}}) \quad (4.6)$$

$$B^{pure}(\boldsymbol{\ell}) = \frac{2}{\ell^2}\int d^2x P^{ab}(\mathbf{x})\mathcal{B}_{ab}(W(\mathbf{x})e^{-i\boldsymbol{\ell}\mathbf{x}}). \quad (4.7)$$

Using this method, any ambiguous modes are projected out and pure E and B modes are recovered. The window function and its first derivative must be zero at the edges of the map to avoid generating spurious B modes (See Appendix 4.B).

Here we show how this method can be simply applied in the flat sky approximation. By applying the product rule to the differential projection operators on the right hand sides of the above equations, we obtain expressions for the pure E and B modes. The $B^{pure}(\boldsymbol{\ell})$ mode is given by (See Appendix 4.B)

$$B^{pure}(\boldsymbol{\ell}) = \frac{2}{\ell^2}\int d^2x W(\mathbf{x})P^{ab}(\mathbf{x})\mathcal{B}_{ab}(e^{-i\boldsymbol{\ell}\mathbf{x}}) + \frac{1}{\ell^2}\int d^2x \left[2Q\partial_x\partial_y W + U(\partial_y^2 - \partial_x^2)W\right] e^{-i\boldsymbol{\ell}\mathbf{x}}$$
$$- \frac{2i}{\ell}\int d^2x \left[Q(\mathbf{x})(\partial_y W\cos\phi_{\boldsymbol{\ell}} + \partial_x W\sin\phi_{\boldsymbol{\ell}}) + U(\mathbf{x})(\partial_y W\sin\phi_{\boldsymbol{\ell}} - \partial_x W\cos\phi_{\boldsymbol{\ell}})\right] e^{-i\boldsymbol{\ell}\mathbf{x}} \quad (4.8)$$

The first term is the standard "naive" B mode estimator and the second and third terms cancel the window-induced leakage from E to B modes, involving derivatives of the window function. This expression is convenient for numerical uses as it does not require the calculation of derivatives of noisy data. The pure estimator removes the E/B leakage, but the remaining mode coupling effect induced by applying a window to the observed sky still needs to be deconvolved.

To work out this effect, we can simplify the algebra if we express the pure estimator in term of the χ variables (e.g., Lewis et al., 2002), with

$$\chi_E(\mathbf{x}) = -\frac{1}{2}\left[\bar{\eth}\bar{\eth}(Q+iU)(\mathbf{x}) + \eth\eth(Q-iU)(\mathbf{x})\right],$$
$$\chi_B(\mathbf{x}) = \frac{i}{2}\left[\bar{\eth}\bar{\eth}(Q+iU)(\mathbf{x}) - \eth\eth(Q-iU)(\mathbf{x})\right], \quad (4.9)$$

where the spin raising and spin lowering operators are defined as $\eth = -(\partial_x + i\partial_y)$, and $\bar{\eth} = -(\partial_x - i\partial_y)$. After some algebra we find simple expressions for the two pure modes (See Appendix

4.C)

$$\begin{aligned} B^{pure}(\boldsymbol{\ell}) &= \frac{1}{\ell^2}\int d\mathbf{x}\chi_B(\mathbf{x})W(\mathbf{x})e^{-i\boldsymbol{\ell}\mathbf{x}}, \\ E^{pure}(\boldsymbol{\ell}) &= \frac{1}{\ell^2}\int d\mathbf{x}\chi_E(\mathbf{x})W(\mathbf{x})e^{-i\boldsymbol{\ell}\mathbf{x}}. \end{aligned} \tag{4.10}$$

The simple expressions for the pure estimators using the χ variables are convenient for computing this mode-to-mode coupling. Noting that

$$\begin{aligned} \chi_E(\mathbf{x}) &= \int d\boldsymbol{\ell}E(\boldsymbol{\ell})\ell^2 e^{i\boldsymbol{\ell}\mathbf{x}}, \\ \chi_B(\mathbf{x}) &= \int d\boldsymbol{\ell}B(\boldsymbol{\ell})\ell^2 e^{i\boldsymbol{\ell}\mathbf{x}}, \end{aligned} \tag{4.11}$$

we find that the coupling between modes is

$$\begin{aligned} \langle B^{pure}(\boldsymbol{\ell})B^{*pure}(\boldsymbol{\ell})\rangle &= \frac{1}{\ell^4}\left\langle \int d\mathbf{x}\chi_B(\mathbf{x})W(\mathbf{x})e^{-i\boldsymbol{\ell}\mathbf{x}}\int d\mathbf{x}'\chi_B(\mathbf{x}')W(\mathbf{x}')e^{i\boldsymbol{\ell}\mathbf{x}'}\right\rangle, \\ &= \frac{1}{\ell^4}\int d\boldsymbol{\ell}'|W(\boldsymbol{\ell}-\boldsymbol{\ell}')|^2\ell'^4 C_{BB}(\boldsymbol{\ell}') \end{aligned} \tag{4.12}$$

for the B-modes, and

$$\langle E^{pure}(\boldsymbol{\ell})E^{*pure}(\boldsymbol{\ell})\rangle = \frac{1}{\ell^4}\int d\boldsymbol{\ell}'|W(\boldsymbol{\ell}-\boldsymbol{\ell}')|^2\ell'^4 C_{EE}(\boldsymbol{\ell}') \tag{4.13}$$

for the E-modes. Here we have used $\langle\chi_B(\boldsymbol{\ell}')\chi_B^*(\boldsymbol{\ell}'')\rangle = \delta(\boldsymbol{\ell}'-\boldsymbol{\ell}'')\ell'^4 C_{BB}(\boldsymbol{\ell}')$. Note that these expressions are much simpler than the ones for the full sky case. This is because of the simple relation between spin 1 and spin 2 Fourier transform and the spin 0 Fourier transform. For the full sky case we need to rely on spin 1 and 2 spherical harmonics transform, making the analytic computation heavy.

In practice using the pure E mode power spectrum estimator is unnecessary since the B-to-E leakage is small so the advantage of using a pure estimator is lost and results in a loss of sensitivity. We choose to use a hybrid approach (Grain et al., 2012), where the B mode power spectrum is computed using the pure formalism (Eqn. 4.8) and the E modes power spectrum is computed via

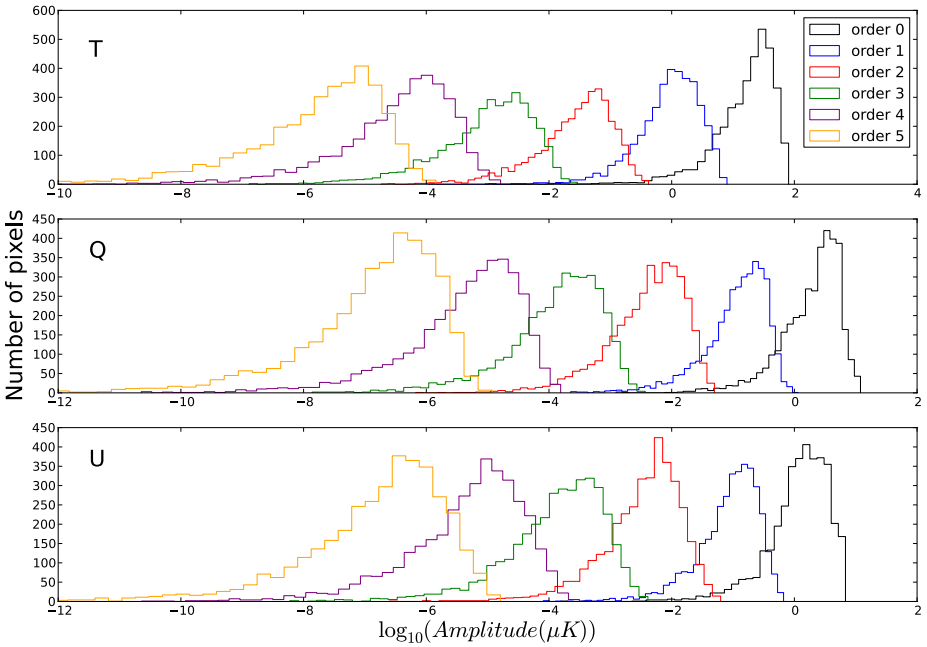

Figure 4.2: **Convergence of the Taylor series in pixel space** We represent the contribution of each higher order term of the Taylor series by showing the histogram of its pixel distribution. The convergence of the series is fast, each term being ≈ 60 times smaller than the preceding one. The contribution of the third order term is of order $10^{-1}\mu$K for T and $10^{-2}\mu$K for Q and U.

the standard pseudo power spectrum formalism.

4.3 Generating gravitationally lensed simulations

On their way from the surface of last scattering, the photons are deflected by the gravitational field of the intervening large scale structure. Accurate lensing simulations are essential for recovering the statistical property of the observed CMB. In the weak field limit, the lensing results in a simple remapping of the temperature by a deflection angle $\alpha = \nabla\phi$, where ϕ is the lensing potential, a line of sight integral over the matter distribution. The same applies to the polarisation field:

$$\begin{aligned} \tilde{T}(\mathbf{x}) &= T(\mathbf{x} + \nabla\phi) \\ \tilde{P}_{ab}(\mathbf{x}) &= P_{ab}(\mathbf{x} + \nabla\phi). \end{aligned} \tag{4.14}$$

This conceptually simple remapping is complicated by the fact that we cannot work directly with the continuous real-space map, only with discrete pixelizations of it. Three main approaches have been suggested for implementing this remapping in simulations (Lewis, 2005):

1. **Go directly from frequency domain to the lensed positions**, i.e. $T(\mathbf{x}+\alpha) = \sum_\ell \mathcal{F}_\ell^{-1}(\mathbf{x}+\alpha)T_\ell$, where $\mathcal{F}_\ell^{-1}(\mathbf{x})$ is the inverse Fourier transform operator, and T_ℓ are the harmonic coefficients of the unlensed map. This approach is exact, but computationally inefficient because the shifted positions will not in general form a regular grid, and one hence cannot use Fast Fourier Transforms (FFT).

2. **Taylor expand the field**: This is straightforward, but has been found to converge slowly at small scales.

3. **Pixel remapping**: Truncate the displacement to the nearest pixel, and read off the corresponding pixel value. This remapping must be done at much higher resolution than the physical scales of interest in the map in order to avoid pixelization errors, and hence comes at a large cost both in terms of CPU-time and memory. It is therefore sometimes combined with pixel-space interpolation schemes.

We present a simple modification to the Taylor expansion method that addresses its slow convergence. In general, the Taylor expansion of a function $f(x)$ around a point x_0 becomes less accurate as the distance from x_0 grows, and conversely, the expansion can be truncated earlier if one can expand around a point close to where one wishes to evaluate the function. The Taylor remapping method above expands $T(\mathbf{x}+\alpha)$ around the point $\alpha = 0$, and the reason for the slow convergence is that α can be relatively large. A better choice is to expand around the pixel center α_0 closest to α, which is already exactly available, resulting in the following expansion

$$\tilde{T}(\mathbf{x}) = T(\mathbf{x}+\alpha_0+\mathbf{\Delta}\alpha) \quad = \quad T(\mathbf{x}+\alpha_0) + \Delta\alpha^c[\partial_c T](\mathbf{x}+\alpha_0) + \frac{1}{2}\Delta\alpha^c\Delta\alpha^d[\partial_c\partial_d T](\mathbf{x}+\alpha_0) + ...$$

The derivatives can be computed in Fourier space

$$\tilde{T}(\mathbf{x}) \quad = \quad T(\mathbf{x}+\alpha_0) + \sum_{n=1}^{\infty}\frac{i^n}{n!}\left[\int(\Delta\alpha^x\ell_x + \Delta\alpha^y\ell_y)^n T(\boldsymbol{\ell})e^{i\boldsymbol{\ell}\mathbf{x}}d\boldsymbol{\ell}\right]_{\mathbf{x}+\alpha_0} \tag{4.15}$$

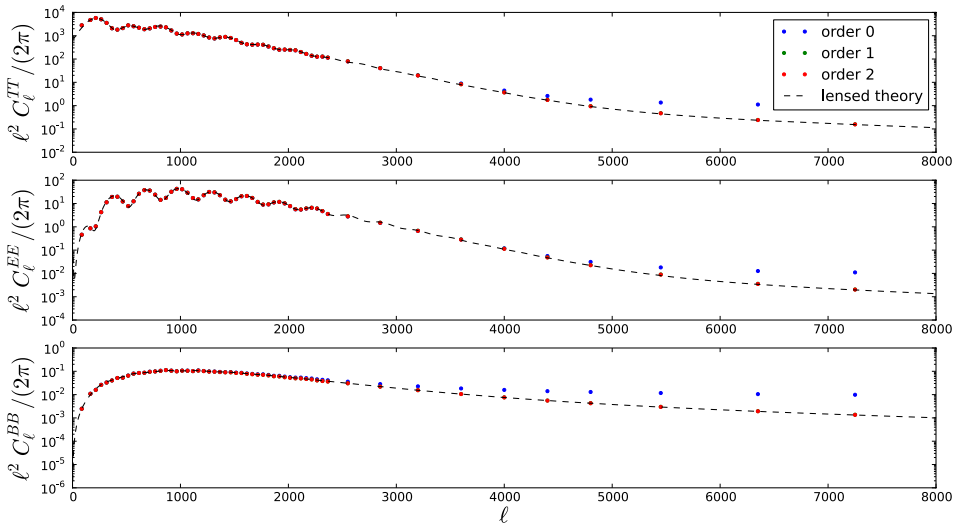

Figure 4.3: **Convergence of the Taylor series: power spectra** We compute the temperature (TT) and polarization (EE, BB) power spectra of the series truncated at different orders. Convergence is achieved by second order in the expansion.

In practice we truncate the expansion at order N

$$\tilde{T}_N(\mathbf{x}) \quad = \quad \sum_{n=0}^{N} \sum_{k \leq n} \frac{(\Delta\alpha^x)^{n-k} (\Delta\alpha^y)^k}{k!(n-k)!} \mathcal{F}^{-1}(i^n \ell_x^{n-k} \ell_y^k \mathcal{F}T)(\mathbf{x} + \alpha_0). \tag{4.16}$$

Here we use the FFT to compute each of the derivatives. Expanding around α_0 ensures that the Taylor expansion will at most need to extrapolate by half a pixel in any direction, which ensures that all scales present in the input map will converge rapidly. This is effectively a hybrid between the pixel remapping and Taylor expansion methods, but unlike normal pixel remapping one does not need to work at higher resolution than the map that is being lensed. Each term in this expansion can be computed at the cost of $(n+1)$ FFT. When expanding around α_0, we find that the series converges rapidly. In Figure 4.2 we show the pixel histograms of a part of the maps for each of the first 6 terms in the expansion. We find that the contribution falls by a factor of ~ 60 for each order for a $13^\circ \times 13^\circ$ lensed noiseless CMB simulation with 0.5' pixel size.

We also computed the bias for each order using 60 such simulations, shown in Figure 4.3, and found that truncating the series at second order is an excellent approximation for any realistic CMB experiment. For comparison, the old method of expanding around $\alpha = 0$ requires more than 20

orders to converge at this resolution, which given the quadratic scaling of the method corresponds to a performance difference of a factor of ~ 50. Using this method, lensing a $13^\circ \times 13^\circ$ patch of the sky at 0.5' resolution takes only a few seconds on one processor, and only requires a few times the memory that a single map takes up. While the method is formulated in the context of the flat sky in this case, it also generalizes trivially to the full, curved sky.

4.4 Implementation on realistic observations

High resolution ground-based experiments are observing small patches of the sky, measuring both the temperature and polarization of the CMB. There are also a set of lower resolution experiments underway targeting larger regions of sky in order to constrain or measure gravitational waves, but these may require analysis on the curved sky. In this section we test our power spectrum estimation method on simulated data, using a specific example of a subset of observations expected from the ACTPol experiment where the flat-sky approximation is appropriate.

Here we assume that 4 patches of the sky, for a total area of ~ 300 deg^2, are observed to a noise level of 5.7 μK/arcmin in temperature. The expected coverage of a patch is non-uniform due to the scanning strategy of the telescope; the expected statistical weight associated with each pixel is shown in the left panel of Figure 4.4 for one of the patches. ACTPol will also target a larger region of the sky ($\sim$1000 deg^2 overlapping with the BOSS survey). For comparison, the PolarBear experiment is targeting three 225 deg^2 regions at 6 μK/arcmin sensitivity in temperature (Kermish et al., 2012), and SPTPol have initially targeted a 100 deg^2 region, with the goal to cover 625 deg^2 to 5 μK/arcmin (Austermann et al., 2012).

4.4.1 Estimated power spectra

We simulate data for each patch of sky in four subsets, generating independent maps of identical coverage and equal depth as in Das et al. (2011a). We refer to each subset as a 'split'. We convolve the simulation with a spherically symmetric gaussian beam with FWHM of $1'$, and we simulate an inhomogeneous noise realization by convolving the weight map for each patch with a 5.7 μK/arcmin noise realization. We 'prewhiten' the temperature maps as defined in Das et al. (2009). Here, the

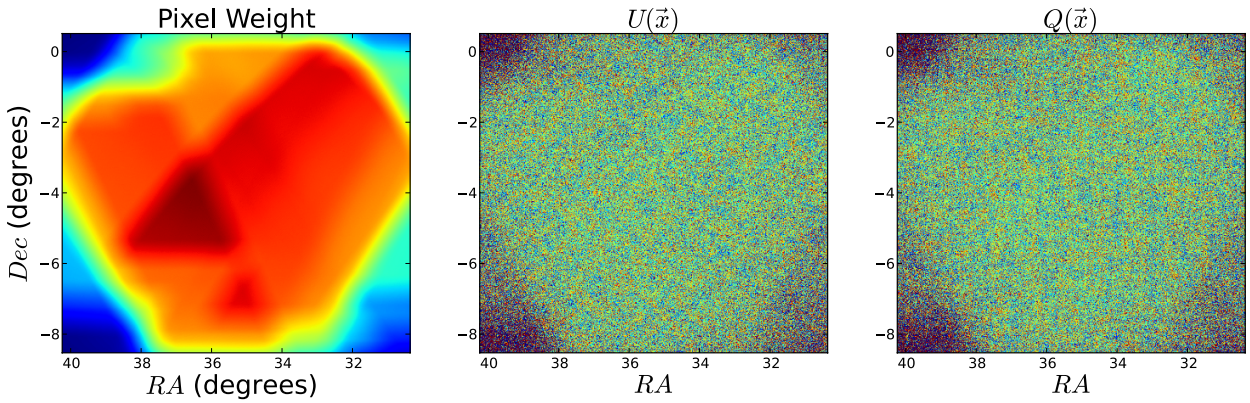

Figure 4.4: **Realization of the noise**, for a U and Q map (centre and right) generated using a simulated pixel weight map (left). This represents the number of observations per pixel for an inhomogeneous survey, and is taken from a simulation for the ACTPol experiment.

maps are convolved in real space with kernels designed to make the power spectrum as flat as possible, to reduce aliasing of power due to the window function. We then apply a 5' (apodized with a 0.3° cosine kernel) point source mask to account for the possible contamination from polarized extragalactic point sources.

We compute the binned cross-power spectrum $C_b^{iX\times jY}$ between maps i and j, for polarization types X and Y, using the pure estimators for B (Eqn. 4.8) and a standard Fourier transform for T and E as discussed in section 2. The estimated spectrum is then given by

$$\widetilde{C}_b^{iX\times jY} = \sum_{b'} M_{bb'}^{XY} C_{b'}^{iX\times jY}, \tag{4.17}$$

where the mode coupling matrix is

$$M_{bb'}^{XY} = \sum_{\boldsymbol{\ell},\boldsymbol{\ell}'} P_{b\boldsymbol{\ell}} |W^{XY}(\boldsymbol{\ell}-\boldsymbol{\ell}')|^2 \left(\frac{\ell'}{\ell}\right)^{\beta_{XY}} (F_{\ell'}^{XY})^2 Q_{\boldsymbol{\ell}'b'}. \tag{4.18}$$

Here $\beta_{XY} = 2[\delta_{BX} + \delta_{BY}]$, i.e., for the pure-mode BB spectrum $\beta = 4$, but $\beta = 0$ for TT and EE. The window function $W^{XY}(\boldsymbol{\ell})$ is a product of the point source mask, the $n_{\rm obs}$ weight map, and a 0.7° cosine apodization at the edges (Smith & Zaldarriaga (2007)), with a geometrical correction for the E modes (Eqn. 4.4). The function F_ℓ^{XY} is the product of the beam, a pixel window function

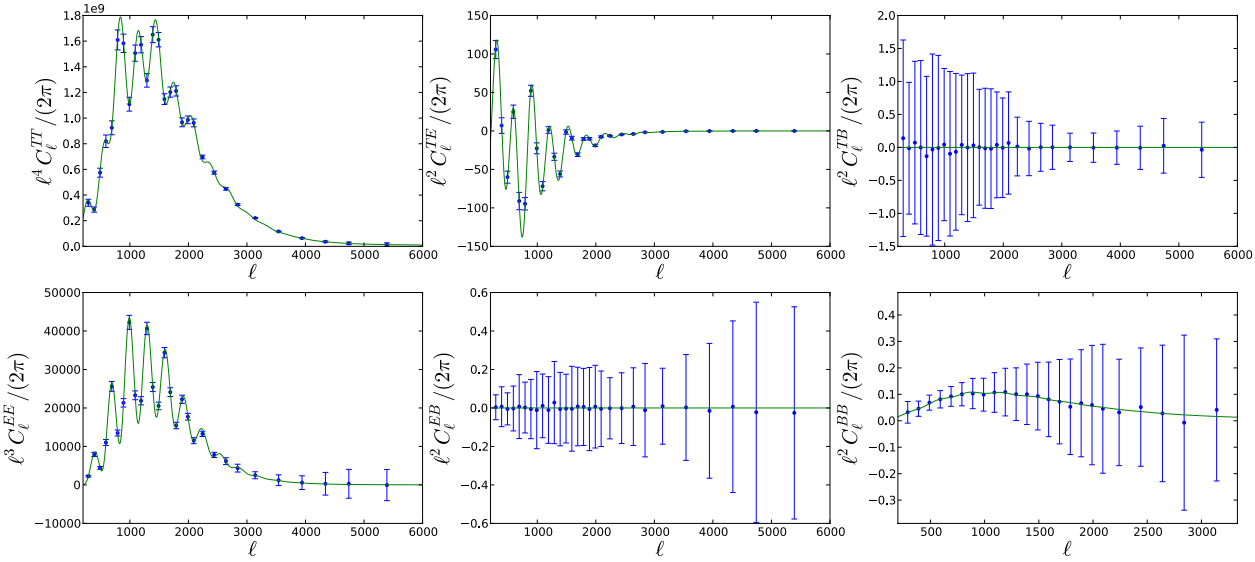

Figure 4.5: **Power spectra estimated from temperature and polarization maps.** This shows the average binned spectra estimated from 720 Monte Carlo simulations, with errors estimated from the 1σ dispersion. The B-mode spectra are derived using the pure estimator, to avoid leakage from the E-mode spectrum.

and the transfer function of the prewhitener for the temperature power spectrum. Here $P_{b\boldsymbol{\ell}}$ is a binning matrix, and $Q_{\boldsymbol{\ell}b}$ is an interpolation matrix, the binning being defined as a set of annuli in the 2 dimensional power spectrum space. Here we choose a minimal bin size of $\Delta\ell = 100$. Each of the mode coupling matrices is computed exactly and inverted in order to recover an unbiased spectrum.

We compute the spectra for 720 realizations of the noise and CMB, each with a different realization of the gravitational lensing potential. The cosmological model we use is the best-fitting ΛCDM model with no tensor contribution, so the B-mode signal comes only from gravitational lensing. The mean recovered spectra for TT, EE, BB, and the cross-correlation spectra are shown in Figure 4.5, together with the estimated 1σ error bar for a single realization derived from the scatter of the simulations. The recovered power spectra are consistent with the input power spectra at the 0.1 σ level in the interval $500 < \ell < 6000$.

4.4.2 Power spectrum uncertainties

Using the Monte Carlo simulations, we can compare the errors derived from the internal scatter, with an analytic estimate. This provides a measure of the optimality of this method. The analytic covariance in a single bin assuming no leakage is given by

$$\begin{aligned}\Theta_{bb}^{(X\times Y);(W\times Z)} &= \frac{1}{\nu_b}\left(C_b^{X\times W}C_b^{Y\times Z}+C_b^{X\times Z}C_b^{Y\times W}\right)\\ &+ \frac{1}{\nu_b n_d}\left(C_b^{X\times W}N_b^{Y\times Z}+C_b^{Y\times Z}N_b^{X\times W}+C_b^{X\times Z}N_b^{Y\times W}+C_b^{Y\times W}N_b^{X\times Z}\right)\\ &+ \frac{1}{\nu_b n_d(n_d-1)}\left(N_b^{X\times W}N_b^{Y\times Z}+N_b^{X\times Z}N_b^{Y\times W}\right), \end{aligned} \tag{4.19}$$

where n_d is the number of splits and ν_b is the number of modes per bin, corrected for the effect of the window function. $C_b^{Y\times Z}$ is the theoretical power spectrum, and $N_b^{Y\times Z}$ is the noise power spectrum, given by $C_{b,\mathrm{auto}}^{Y\times Z}-C_{b,\mathrm{cross}}^{Y\times Z}$. This does not include the non-Gaussian part of the covariance due to the effect of lensing, described in Benoit-Levy et al. (2012). This is a subdominant part of the error for the noise levels we consider here, but introduces correlations between bins. We find that the analytic error bars agree with the 1σ dispersion from the simulations at the 15% level for $500<\ell<6000$, as shown in Figure 4.6, indicating that all sources of leakage on these scales are subdominant. The error is dominated by cosmic variance at large scales, but at smaller scales is noise dominated. This agreement is promising and demonstrates the power of the pure estimator to recover the B-mode spectrum. In practice these spectra will be used to construct a likelihood for testing cosmological models, such that

$$-2\ln L=(\tilde{C}_b-C_b^{\mathrm{th}})^T Q^{-1}(\tilde{C}_b-C_b^{\mathrm{th}}). \tag{4.20}$$

The full covariance matrix, Q, can be estimated numerically from the simulations, or analytically, and the binned theory spectra C_b^{th} computed using bandpower window functions. The realistic likelihood will also include the lensing deflection spectrum, estimated from higher point statistics of the map, and appropriate cross-correlations.

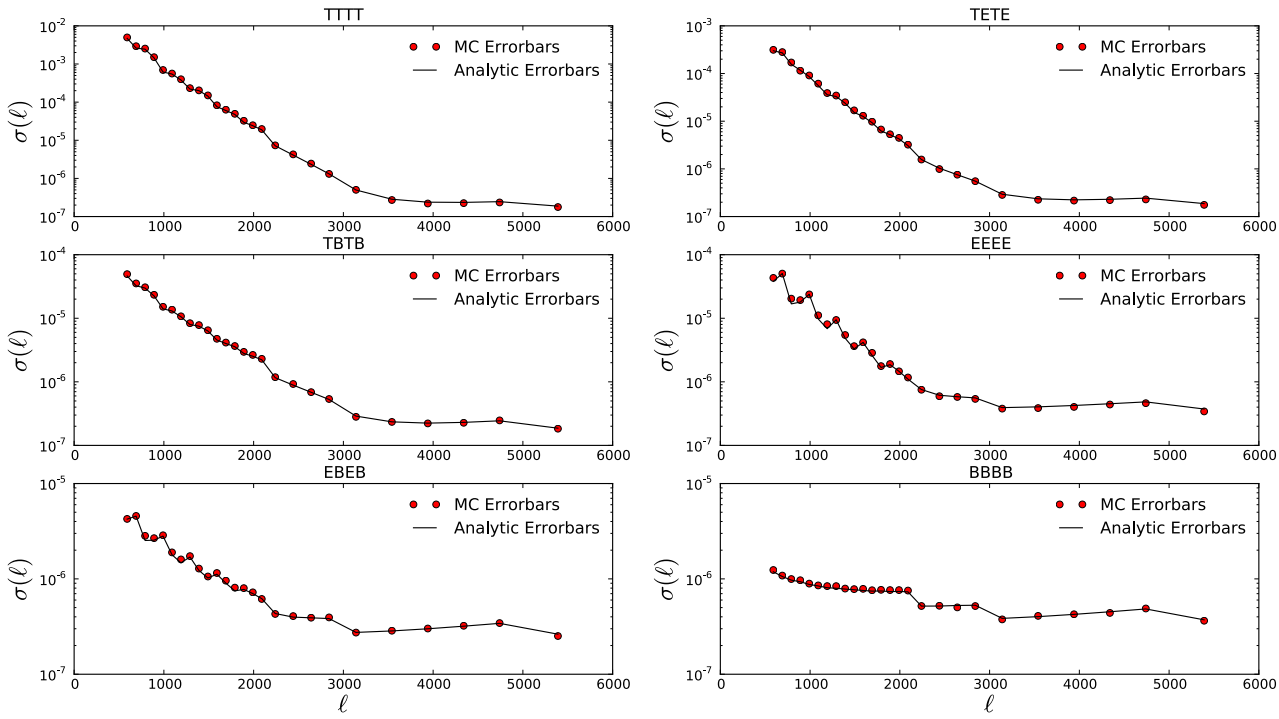

Figure 4.6: **Comparison between Monte Carlo scatter and analytic errors for each cross spectrum for one of the patches.** They agree at the 15 per cent level for $500 < \ell < 6000$, indicating that all sources of leakage are subdominant for these modes, The analytic estimate does not include the non-Gaussian contribution from lensing, but the noise in our simulation is high enough for this effect to be subdominant.

4.5 Conclusions

A number of issues arise in the analysis of high resolution CMB polarization maps, one of the most significant being the leakage of E-mode into B-mode polarization due to observing a limited region of sky. In this paper we have described a simple method for estimating the power spectrum in the flat sky approximation that minimizes this leakage. It draws on an existing all-sky method using a 'pure' estimator for the B-mode, and simplifies the approach for the flat sky. This will be appropriate for small regions observed by current CMB experiments including ACTPol, SPTPol, and PolarBear. Using a suite of Monte Carlo simulations with realistic noise levels for upcoming experiments, we have demonstrated our ability to recover unbiased and quasi-optimal power spectra.

To test the robustness of any power spectrum method requires accurate simulations. The B-mode polarization spectrum at small angular scales is sourced solely from the gravitational lensing of the

E-mode signal. We have shown how high resolution lensed CMB maps can be rapidly and accurately simulated using a hybrid approach between pixel remapping and interpolation in harmonic space. This method, which has advantages over the standard pixel-space interpolation approach, also has the potential to be extended to full sky spherical maps (Næss & Louis (2013)).

Appendix 4.A

Defining the windows function:

$$W(\mathbf{x}) = \begin{cases} w(\mathbf{x}) & \text{if} \quad \mathbf{x} \in \Omega \\ 0 & \text{otherwise,} \end{cases} \tag{4.21}$$

the observed Q and U component are given by

$$\tilde{Q}(\mathbf{x}) = W(\mathbf{x})Q(\mathbf{x}) \tag{4.22}$$

$$\tilde{U}(\mathbf{x}) = W(\mathbf{x})U(\mathbf{x}), \tag{4.23}$$

with Fourier component

$$\tilde{Q}(\boldsymbol{\ell}) = \int d\boldsymbol{\ell'} W(\boldsymbol{\ell} - \boldsymbol{\ell'})Q(\boldsymbol{\ell'}) \tag{4.24}$$

$$\tilde{U}(\boldsymbol{\ell}) = \int d\boldsymbol{\ell'} W(\boldsymbol{\ell} - \boldsymbol{\ell'})U(\boldsymbol{\ell'}). \tag{4.25}$$

$$\tag{4.26}$$

The estimated E and B modes are given by

$$\begin{aligned} \tilde{E}(\boldsymbol{\ell}) \pm i\tilde{B}(\boldsymbol{\ell}) &= e^{\mp 2i\phi_{\boldsymbol{\ell}}}(\tilde{Q}(\boldsymbol{\ell}) \pm i\tilde{U}(\boldsymbol{\ell})) && (4.27) \\ &= e^{\mp 2i\phi_{\boldsymbol{\ell}}} \int d\boldsymbol{\ell'} W(\boldsymbol{\ell} - \boldsymbol{\ell'})[Q(\boldsymbol{\ell'}) \pm iU(\boldsymbol{\ell'})] && (4.28) \\ &= e^{\mp 2i\phi_{\boldsymbol{\ell}}} \int d\boldsymbol{\ell'} W(\boldsymbol{\ell} - \boldsymbol{\ell'})[E(\boldsymbol{\ell'}) \pm iB(\boldsymbol{\ell'})]e^{\pm 2i\phi_{\boldsymbol{\ell'}}} && (4.29) \\ &= \int d\boldsymbol{\ell'} W(\boldsymbol{\ell} - \boldsymbol{\ell'})[E(\boldsymbol{\ell'}) \pm iB(\boldsymbol{\ell'})]e^{\pm 2i(\phi_{\boldsymbol{\ell'}} - \phi_{\boldsymbol{\ell}})} && (4.30) \end{aligned}$$

So they are a combination of the true underlying E and B modes:

$$\begin{aligned}
\tilde{E}(\boldsymbol{\ell}) &= \frac{1}{2}\int d\boldsymbol{\ell'} W(\boldsymbol{\ell}-\boldsymbol{\ell'})\left([E(\boldsymbol{\ell'})+iB(\boldsymbol{\ell'})]e^{2i(\phi_{\boldsymbol{\ell'}}-\phi_{\boldsymbol{\ell}})}+[E(\boldsymbol{\ell'})-iB(\boldsymbol{\ell'})]e^{-2i(\phi_{\boldsymbol{\ell'}}-\phi_{\boldsymbol{\ell}})}\right) \\
&= \int d\boldsymbol{\ell'} W(\boldsymbol{\ell}-\boldsymbol{\ell'})[E(\boldsymbol{\ell'})\cos 2(\phi_{\boldsymbol{\ell'}}-\phi_{\boldsymbol{\ell}})-B(\boldsymbol{\ell'})\sin 2(\phi_{\boldsymbol{\ell'}}-\phi_{\boldsymbol{\ell}})] \\
\tilde{B}(\boldsymbol{\ell}) &= \frac{1}{2i}\int d\boldsymbol{\ell'} W(\boldsymbol{\ell}-\boldsymbol{\ell'})\left([E(\boldsymbol{\ell'})+iB(\boldsymbol{\ell'})]e^{2i(\phi_{\boldsymbol{\ell'}}-\phi_{\boldsymbol{\ell}})}-[E(\boldsymbol{\ell'})-iB(\boldsymbol{\ell'})]e^{-2i(\phi_{\boldsymbol{\ell'}}-\phi_{\boldsymbol{\ell}})}\right) \quad (4.31) \\
&= \int d\boldsymbol{\ell'} W(\boldsymbol{\ell}-\boldsymbol{\ell'})[E(\boldsymbol{\ell'})\sin 2(\phi_{\boldsymbol{\ell'}}-\phi_{\boldsymbol{\ell}})+B(\boldsymbol{\ell'})\cos 2(\phi_{\boldsymbol{\ell'}}-\phi_{\boldsymbol{\ell}})]
\end{aligned}$$

(4.32)

Let us assume that there is no primordial $\langle EB\rangle$, we have:

$$\begin{aligned}
\langle\tilde{E}(\boldsymbol{\ell})\tilde{E}^*(\boldsymbol{\ell})\rangle &= \int d\boldsymbol{\ell'}|W(\boldsymbol{\ell}-\boldsymbol{\ell'})|^2[C_{EE}(\ell')\cos^2 2(\phi_{\boldsymbol{\ell'}}-\phi_{\boldsymbol{\ell}})+C_{BB}(\ell')\sin^2 2(\phi_{\boldsymbol{\ell'}}-\phi_{\boldsymbol{\ell}})] \\
\langle\tilde{B}(\boldsymbol{\ell})\tilde{B}^*(\boldsymbol{\ell})\rangle &= \int d\boldsymbol{\ell'}|W(\boldsymbol{\ell}-\boldsymbol{\ell'})|^2[C_{EE}(\ell')\sin^2 2(\phi_{\boldsymbol{\ell'}}-\phi_{\boldsymbol{\ell}})+C_{BB}(\ell')\cos^2 2(\phi_{\boldsymbol{\ell'}}-\phi_{\boldsymbol{\ell}})] \quad (4.33)
\end{aligned}$$

So,

$$\begin{pmatrix}\tilde{C}_{EE}(\boldsymbol{\ell})\\ \tilde{C}_{BB}(\boldsymbol{\ell})\end{pmatrix} = \sum_{\ell'} M_{\boldsymbol{\ell},\boldsymbol{\ell'}}\begin{pmatrix}C_{EE}(\boldsymbol{\ell'})\\ C_{BB}(\boldsymbol{\ell'})\end{pmatrix}, \quad (4.34)$$

with

$$M_{\boldsymbol{\ell},\boldsymbol{\ell'}} = |W(\boldsymbol{\ell}-\boldsymbol{\ell'})|^2\begin{pmatrix}\cos^2 2(\phi_{\boldsymbol{\ell'}}-\phi_{\boldsymbol{\ell}}) & \sin^2 2(\phi_{\boldsymbol{\ell'}}-\phi_{\boldsymbol{\ell}})\\ \sin^2 2(\phi_{\boldsymbol{\ell'}}-\phi_{\boldsymbol{\ell}}) & \cos^2 2(\phi_{\boldsymbol{\ell'}}-\phi_{\boldsymbol{\ell}})\end{pmatrix}, \quad (4.35)$$

Including TE, TB and EB correlations we have

$$\begin{aligned}
\langle\tilde{E}(\boldsymbol{\ell})\tilde{E}^*(\boldsymbol{\ell})\rangle &= \int d\boldsymbol{\ell'}|W(\boldsymbol{\ell}-\boldsymbol{\ell'})|^2[C_{EE}(\ell')\cos^2 2(\phi_{\boldsymbol{\ell'}}-\phi_{\boldsymbol{\ell}}) + C_{BB}(\ell')\sin^2 2(\phi_{\boldsymbol{\ell'}}-\phi_{\boldsymbol{\ell}}) \\
&- 2C_{EB}(\ell')\cos 2(\phi_{\boldsymbol{\ell'}}-\phi_{\boldsymbol{\ell}})\sin 2(\phi_{\boldsymbol{\ell'}}-\phi_{\boldsymbol{\ell}})] \\
\langle\tilde{B}(\boldsymbol{\ell})\tilde{B}^*(\boldsymbol{\ell})\rangle &= \int d\boldsymbol{\ell'}|W(\boldsymbol{\ell}-\boldsymbol{\ell'})|^2[C_{EE}(\ell')\sin^2 2(\phi_{\boldsymbol{\ell'}}-\phi_{\boldsymbol{\ell}}) + C_{BB}(\ell')\cos^2 2(\phi_{\boldsymbol{\ell'}}-\phi_{\boldsymbol{\ell}}) \\
&+ 2C_{EB}(\ell')\cos 2(\phi_{\boldsymbol{\ell'}}-\phi_{\boldsymbol{\ell}})\sin 2(\phi_{\boldsymbol{\ell'}}-\phi_{\boldsymbol{\ell}})] \\
\langle\tilde{T}(\boldsymbol{\ell})\tilde{E}^*(\boldsymbol{\ell})\rangle &= \int d\boldsymbol{\ell'}|W(\boldsymbol{\ell}-\boldsymbol{\ell'})|^2[C_{TE}(\ell')\cos 2(\phi_{\boldsymbol{\ell'}}-\phi_{\boldsymbol{\ell}}) - C_{TB}(\ell')\sin 2(\phi_{\boldsymbol{\ell'}}-\phi_{\boldsymbol{\ell}})] \\
\langle\tilde{T}(\boldsymbol{\ell})\tilde{B}^*(\boldsymbol{\ell})\rangle &= \int d\boldsymbol{\ell'}|W(\boldsymbol{\ell}-\boldsymbol{\ell'})|^2[C_{TE}(\ell')\sin 2(\phi_{\boldsymbol{\ell'}}-\phi_{\boldsymbol{\ell}}) + C_{TB}(\ell')\cos 2(\phi_{\boldsymbol{\ell'}}-\phi_{\boldsymbol{\ell}})] \\
\langle\tilde{E}(\boldsymbol{\ell})\tilde{B}^*(\boldsymbol{\ell})\rangle &= \int d\boldsymbol{\ell'}|W(\boldsymbol{\ell}-\boldsymbol{\ell'})|^2[C_{EE}(\ell')\cos 2(\phi_{\boldsymbol{\ell'}}-\phi_{\boldsymbol{\ell}})\sin 2(\phi_{\boldsymbol{\ell'}}-\phi_{\boldsymbol{\ell}}) \\
&- C_{BB}(\ell')\sin 2(\phi_{\boldsymbol{\ell'}}-\phi_{\boldsymbol{\ell}})\cos 2(\phi_{\boldsymbol{\ell'}}-\phi_{\boldsymbol{\ell}}) + C_{EB}(\cos^2 2(\phi_{\boldsymbol{\ell'}}-\phi_{\boldsymbol{\ell}}) - \sin^2 2(\phi_{\boldsymbol{\ell'}}-\phi_{\boldsymbol{\ell}}))].
\end{aligned} \tag{4.36}$$

The estimated power spectra are given by a linear combination of the true underlying power spectra

$$\begin{pmatrix} \tilde{C}_{TE}(\boldsymbol{\ell}) \\ \tilde{C}_{TB}(\boldsymbol{\ell}) \\ \tilde{C}_{EE}(\boldsymbol{\ell}) \\ \tilde{C}_{EB}(\boldsymbol{\ell}) \\ \tilde{C}_{BB}(\boldsymbol{\ell}) \end{pmatrix} = \sum_{\ell'} M_{\boldsymbol{\ell},\boldsymbol{\ell'}} \begin{pmatrix} C_{TE}(\boldsymbol{\ell'}) \\ C_{TB}(\boldsymbol{\ell'}) \\ C_{EE}(\boldsymbol{\ell'}) \\ C_{EB}(\boldsymbol{\ell'}) \\ C_{BB}(\boldsymbol{\ell'}) \end{pmatrix} \tag{4.37}$$

Defining $\Delta_{\ell,\ell'} = 2(\phi_{\boldsymbol{\ell'}} - \phi_{\boldsymbol{\ell}})$, gives

$$M_{\boldsymbol{\ell},\boldsymbol{\ell'}} = |W(\boldsymbol{\ell}-\boldsymbol{\ell'})|^2 \begin{pmatrix} \cos\Delta_{\ell,\ell'} & -\sin\Delta_{\ell,\ell'} & 0 & 0 & 0 \\ \sin\Delta_{\ell,\ell'} & \cos\Delta_{\ell,\ell'} & 0 & 0 & 0 \\ 0 & 0 & \cos^2\Delta_{\ell,\ell'} & -2\cos\Delta_{\ell,\ell'}\sin\Delta_{\ell,\ell'} & \sin^2\Delta_{\ell,\ell'} \\ 0 & 0 & \cos\Delta_{\ell,\ell'}\sin\Delta_{\ell,\ell'} & \cos^2\Delta_{\ell,\ell'} - \sin^2\Delta_{\ell,\ell'} & -\cos\Delta_{\ell,\ell'}\sin\Delta_{\ell,\ell'} \\ 0 & 0 & \sin^2\Delta_{\ell,\ell'} & 2\cos\Delta_{\ell,\ell'}\sin\Delta_{\ell,\ell'} & \cos^2\Delta_{\ell,\ell'} \end{pmatrix}.$$

Appendix 4.B

Pure B modes are defined as

$$B^{pure}(\boldsymbol{\ell}) = \frac{2}{\ell^2}\int d^2x P^{ab}(\mathbf{x})\mathcal{B}_{ab}(W(\mathbf{x})e^{-i\boldsymbol{\ell}\mathbf{x}}). \tag{4.38}$$

A proof that this estimate only contains B modes is to show that starting with a pure E mode $P_{ab} = \mathcal{E}_{ab}\phi(\mathbf{x})$, with $\phi(\mathbf{x})$ a scalar function, the estimate gives zero:

$$\begin{aligned}
B^{pure}(\boldsymbol{\ell}) &= \frac{2}{\ell^2}\int d^2x \left[(-\partial^a\partial^b + \frac{1}{2}\delta^{ab}\nabla^2)\phi(\mathbf{x})\right]\left[\epsilon_{ac}\partial^c\partial_b(W(\mathbf{x})e^{-i\boldsymbol{\ell}\mathbf{x}})\right] \\
&= \frac{2}{\ell^2}\int d^2x \left[-\epsilon_{ac}\partial^c(-\partial^a\partial^b + \frac{1}{2}\delta^{ab}\nabla^2)\phi(\mathbf{x})\right]\left[\partial_b(W(\mathbf{x})e^{-i\boldsymbol{\ell}\mathbf{x}})\right] \\
&+ \oint d\sigma\epsilon_{ac}n^c\left(-\partial^a\partial^b + \frac{1}{2}\delta^{ab}\nabla^2)\phi(\mathbf{x})\right)\partial_b(W(\mathbf{x})e^{-i\boldsymbol{\ell}\mathbf{x}}) \\
&= \frac{2}{\ell^2}\int d^2x \left[\epsilon_{ac}\partial^c\partial_b(-\partial^a\partial^b + \frac{1}{2}\delta^{ab}\nabla^2)\phi(\mathbf{x})\right]\left[(W(\mathbf{x})e^{-i\boldsymbol{\ell}\mathbf{x}})\right] \\
&+ \oint d\sigma\epsilon_{ac}n^c\left(-\partial^a\partial^b + \frac{1}{2}\delta^{ab}\nabla^2)\phi(\mathbf{x})\right)\partial_b(W(\mathbf{x})e^{-i\boldsymbol{\ell}\mathbf{x}}) \\
&+ \oint d\sigma n_b\left[-\epsilon_{ac}\partial^c(-\partial^a\partial^b + \frac{1}{2}\delta^{ab}\nabla^2)\phi(\mathbf{x})\right]\left[(W(\mathbf{x})e^{-i\boldsymbol{\ell}\mathbf{x}})\right] \\
&= \frac{2}{\ell^2}\int d^2x \left[\epsilon_{ac}\partial^c\partial_b(-\partial^a\partial^b + \frac{1}{2}\delta^{ab}\nabla^2)\phi(\mathbf{x})\right]\left[(W(\mathbf{x})e^{-i\boldsymbol{\ell}\mathbf{x}})\right] \\
&- \oint d\sigma t_a\left((-\partial^a\partial^b + \frac{1}{2}\delta^{ab}\nabla^2)\phi(\mathbf{x})\right)\partial_b(W(\mathbf{x})e^{-i\boldsymbol{\ell}\mathbf{x}}) \\
&+ \oint d\sigma n^a\left[-\epsilon_{ac}\partial^c\frac{1}{2}\nabla^2\phi(\mathbf{x})\right]\left[(W(\mathbf{x})e^{-i\boldsymbol{\ell}\mathbf{x}})\right] \\
&= \frac{2}{\ell^2}\int d^2x \left[\epsilon_{ac}\partial^c\partial_b(-\partial^a\partial^b + \frac{1}{2}\delta^{ab}\nabla^2)\phi(\mathbf{x})\right]\left[(W(\mathbf{x})e^{-i\boldsymbol{\ell}\mathbf{x}})\right] \\
&- \oint d\sigma t_a\left(-\partial^a\partial^b + \frac{1}{2}\delta^{ab}\nabla^2)\phi(\mathbf{x})\right)\partial_b(W(\mathbf{x})e^{-i\boldsymbol{\ell}\mathbf{x}}) \\
&- \oint d\sigma t_c(\frac{1}{2}\partial^c\nabla^2\phi(\mathbf{x}))\left[(W(\mathbf{x})e^{-i\boldsymbol{\ell}\mathbf{x}})\right] \\
&= 0
\end{aligned} \tag{4.39}$$

if $W(x)$ and $\partial_a W(x)$ vanish on the survey boundary. We also used $t_a = -\epsilon_{ac}n^c$, and the fact that $\mathcal{B}_{ab}\mathcal{E}^{ab}$ vanish. To express $B^{pure}(\boldsymbol{\ell})$ as a function of the Stokes parameters, we need to expand

$\mathcal{B}_{ab}(W(\mathbf{x})e^{i\boldsymbol{\ell}\mathbf{x}})$ in term of Fourier modes and derivative of windows function

$$\begin{aligned}
&\mathcal{B}_{ab}(AB) = \frac{1}{2}(\epsilon_{ac}\partial^c\partial_b + \epsilon_{bc}\partial^c\partial_a)(AB) = \frac{1}{2}(\epsilon_{ac}\partial^c(B\partial_b A + A\partial_b B) + \epsilon_{bc}\partial^c(B\partial_a A + A\partial_a B)) \\
= \;& \frac{1}{2}(\epsilon_{ac}(\partial^c B\partial_b A + \partial^c A\partial_b B + B\partial^c\partial_b A + A\partial^c\partial_b B) + \epsilon_{bc}(\partial^c B\partial_a A + \partial^c A\partial_a B + B\partial^c\partial_a A + A\partial^c\partial_a B)) \\
= \;& B\mathcal{B}_{ab}(A) + A\mathcal{B}_{ab}(B) + \frac{1}{2}\left[\epsilon_{ac}(\partial^c B\partial_b A + \partial^c A\partial_b B) + \epsilon_{bc}(\partial^c B\partial_a A + \partial^c A\partial_a B)\right]. \qquad (4.40)
\end{aligned}$$

We can rewrite the last term as $2T_{abcd}\partial^c A\partial^d B$ with:

$$T_{abcd} = \frac{1}{4}(\epsilon_{ad}\delta_{bc} + \epsilon_{ac}\delta_{bd} + \epsilon_{bd}\delta_{ac} + \epsilon_{bc}\delta_{ad}). \qquad (4.41)$$

Finally:

$$\begin{aligned}
B^{pure}(\boldsymbol{\ell}) &= \frac{2}{\ell^2}\int d^2x P^{ab}(\mathbf{x})\mathcal{B}_{ab}(W(\mathbf{x})e^{-i\boldsymbol{\ell}\mathbf{x}}) \\
&= \frac{2}{\ell^2}\int d^2x P^{ab}(\mathbf{x})\left[W(\mathbf{x})\mathcal{B}_{ab}(e^{-i\boldsymbol{\ell}\mathbf{x}}) + \mathcal{B}_{ab}(W(\mathbf{x}))e^{-i\boldsymbol{\ell}\mathbf{x}} + 2T_{abcd}\partial^c W(\mathbf{x})\partial^d(e^{-i\boldsymbol{\ell}\mathbf{x}})\right] \\
&= \frac{2}{\ell^2}\int d^2x W(\mathbf{x})P^{ab}(\mathbf{x})\mathcal{B}_{ab}(e^{-i\boldsymbol{\ell}\mathbf{x}}) \\
&+ \frac{1}{\ell^2}\int d^2x\left[2Q(\mathbf{x})\partial_x\partial_y W + U(\mathbf{x})(\partial_y^2 - \partial_x^2)W\right]e^{-i\boldsymbol{\ell}\mathbf{x}} \\
&- \frac{2i}{\ell}\int d^2x\left[Q(\mathbf{x})(\partial_y W\cos\phi_{\boldsymbol{\ell}} + \partial_x W\sin\phi_{\boldsymbol{\ell}}) + U(\mathbf{x})(\partial_y W\sin\phi_{\boldsymbol{\ell}} - \partial_x W\cos\phi_{\boldsymbol{\ell}})\right]e^{-i\boldsymbol{\ell}\mathbf{x}}
\end{aligned} \qquad (4.42)$$

.

Appendix 4.C

The χ variables are defined as

$$\begin{aligned}
\chi_E(\mathbf{x}) &= -\frac{1}{2}\left[\bar{\eth}\bar{\eth}(Q+iU)(\mathbf{x}) + \eth\eth(Q-iU)(\mathbf{x})\right] \\
\chi_B(\mathbf{x}) &= \frac{i}{2}\left[\bar{\eth}\bar{\eth}(Q+iU)(\mathbf{x}) - \eth\eth(Q-iU)(\mathbf{x})\right] \qquad (4.43)
\end{aligned}$$

with

$$\begin{aligned}\eth\eth e^{i\boldsymbol{\ell}\mathbf{x}} &= (i\ell_x - \ell_y)^2 e^{i\boldsymbol{\ell}\mathbf{x}} = -\ell^2 e^{2i\phi_{\boldsymbol{\ell}}} e^{i\boldsymbol{\ell}\mathbf{x}} \\ \bar{\eth}\bar{\eth} e^{i\boldsymbol{\ell}\mathbf{x}} &= (i\ell_x + \ell_y)^2 e^{i\boldsymbol{\ell}\mathbf{x}} = -\ell^2 e^{-2i\phi_{\boldsymbol{\ell}}} e^{i\boldsymbol{\ell}\mathbf{x}}. \end{aligned} \tag{4.44}$$

We have:

$$\begin{aligned}\chi_E(\mathbf{x}) &= \int d\boldsymbol{\ell} E(\boldsymbol{\ell}) \ell^2 e^{i\boldsymbol{\ell}\mathbf{x}} \\ \chi_B(\mathbf{x}) &= \int d\boldsymbol{\ell} B(\boldsymbol{\ell}) \ell^2 e^{i\boldsymbol{\ell}\mathbf{x}}. \end{aligned} \tag{4.45}$$

We can show that we can rewrite $B^{pure}(\boldsymbol{\ell})$ in term of this variable:

$$\begin{aligned} B^{pure}(\boldsymbol{\ell}) &= \frac{1}{\ell^2} \int d\mathbf{x} \chi_B(\mathbf{x}) W(\mathbf{x}) e^{-i\boldsymbol{\ell}\mathbf{x}} \\ &= \frac{i}{2\ell^2} \int d\mathbf{x} \left[(Q(\mathbf{x}) + iU(\mathbf{x})) \bar{\eth}\bar{\eth} W(\mathbf{x}) e^{-i\boldsymbol{\ell}\mathbf{x}} - (Q(\mathbf{x}) - iU(\mathbf{x})) \eth\eth W(\mathbf{x}) e^{-i\boldsymbol{\ell}\mathbf{x}} \right]. \end{aligned} \tag{4.46}$$

Expanding the derivative operator

$$\begin{aligned} (\partial_x + i\partial_y)(\partial_x + i\partial_y)(W(\mathbf{x})e^{-i\boldsymbol{\ell}\mathbf{x}}) &= (\partial_x + i\partial_y)\left[(\partial_x W(\mathbf{x}) - i\ell_x W(\mathbf{x}) + i\partial_y W(\mathbf{x}) + \ell_y W(\mathbf{x})\right] e^{-i\boldsymbol{\ell}\mathbf{x}} \\ &= \left(\partial_x^2 W(\mathbf{x}) - i\ell_x \partial_x W(\mathbf{x}) + i\partial_x\partial_y W(\mathbf{x}) + \ell_y \partial_x W(\mathbf{x})\right) e^{-i\boldsymbol{\ell}\mathbf{x}} \\ &- \left(i\ell_x \partial_x W(\mathbf{x}) + \ell_x^2 W(\mathbf{x}) - \ell_x \partial_y W(\mathbf{x}) + i\ell_x\ell_y W(\mathbf{x})\right) e^{-i\boldsymbol{\ell}\mathbf{x}} \\ &+ \left(i\partial_y\partial_x W(\mathbf{x}) + \ell_x \partial_y W(\mathbf{x}) - \partial_y^2 W(\mathbf{x}) + i\ell_y \partial_y W(\mathbf{x})\right) e^{-i\boldsymbol{\ell}\mathbf{x}} \\ &+ \left(\ell_y \partial_x W(\mathbf{x}) - i\ell_y\ell_x W(\mathbf{x}) + i\ell_y \partial_y W(\mathbf{x}) + \ell_y^2 W(\mathbf{x})\right) e^{-i\boldsymbol{\ell}\mathbf{x}} \end{aligned} \tag{4.47}$$

We note: $\eth\eth(W(\mathbf{x})e^{-i\boldsymbol{\ell}\mathbf{x}}) = f(\mathbf{x})e^{-i\boldsymbol{\ell}\mathbf{x}}$ with

$$\begin{aligned} f(\mathbf{x}) = (\partial_x^2 - \partial_y^2)W(\mathbf{x}) + (\ell_y^2 - \ell_x^2)W(\mathbf{x}) - 2i\ell_x\partial_x W(\mathbf{x}) + 2i\partial_x\partial_y W(\mathbf{x}) + 2\ell_y\partial_x W(\mathbf{x}) \\ + 2\ell_x\partial_y W(\mathbf{x}) - 2i\ell_x\ell_y W(\mathbf{x}) + 2i\ell_y\partial_y W(\mathbf{x}) \end{aligned}$$

The action of the second derivative operator can also be computed

$$\begin{aligned}
(\partial_x - i\partial_y)(\partial_x - i\partial_y)(W(\mathbf{x})e^{-i\boldsymbol{\ell}\mathbf{x}}) &= (\partial_x - i\partial_y)\left[(\partial_x W(\mathbf{x}) - i\ell_x W(\mathbf{x}) - i\partial_y W(\mathbf{x}) - \ell_y W(\mathbf{x})\right] e^{-i\boldsymbol{\ell}\mathbf{x}} \\
&= \left(\partial_x^2 W(\mathbf{x}) - i\ell_x\partial_x W(\mathbf{x}) - i\partial_x\partial_y W(\mathbf{x}) - \ell_y\partial_x W(\mathbf{x})\right) e^{-i\boldsymbol{\ell}\mathbf{x}} \\
&- \left(i\ell_x\partial_x W(\mathbf{x}) + \ell_x^2 W(\mathbf{x}) + \ell_x\partial_y W(\mathbf{x}) - i\ell_x\ell_y W(\mathbf{x})\right) e^{-i\boldsymbol{\ell}\mathbf{x}} \\
&- \left(i\partial_y\partial_x W(\mathbf{x}) + \ell_x\partial_y W(\mathbf{x}) + \partial_y^2 W(\mathbf{x}) - i\ell_y\partial_y W(\mathbf{x})\right) e^{-i\boldsymbol{\ell}\mathbf{x}} \\
&- \left(\ell_y\partial_x W(\mathbf{x}) - i\ell_y\ell_x W(\mathbf{x}) - i\ell_y\partial_y W(\mathbf{x}) - \ell_y^2 W(\mathbf{x})\right) e^{-i\boldsymbol{\ell}\mathbf{x}} \\
&= g(\mathbf{x})e^{-i\boldsymbol{\ell}\mathbf{x}} \qquad (4.48)
\end{aligned}$$

with

$$\begin{aligned}
g(\mathbf{x}) = (\partial_x^2 - \partial_y^2)W(\mathbf{x}) + (\ell_y^2 - \ell_x^2)W(\mathbf{x}) - 2i\ell_x\partial_x W(\mathbf{x}) - 2i\partial_x\partial_y W(\mathbf{x}) - 2\ell_y\partial_x W(\mathbf{x}) \\
- 2\ell_x\partial_y W(\mathbf{x}) + 2i\ell_x\ell_y W(\mathbf{x}) + 2i\ell_y\partial_y W(\mathbf{x}).
\end{aligned}$$

We can express the difference and the sum of these two functions

$$\begin{aligned}
g(\mathbf{x}) - f(\mathbf{x}) &= -4i\partial_x\partial_y W(\mathbf{x}) - 4\ell_y\partial_x W(\mathbf{x}) - 4\ell_x\partial_y W(\mathbf{x}) + 4i\ell_x\ell_y W(\mathbf{x}) \\
f(\mathbf{x}) + g(\mathbf{x}) &= 2(\partial_x^2 - \partial_y^2)W(\mathbf{x}) + 2(\ell_y^2 - \ell_x^2)W(\mathbf{x}) - 4i\ell_x\partial_x W(\mathbf{x}) + 4i\ell_y\partial_y W(\mathbf{x})
\end{aligned} \qquad (4.49)$$

$$
\begin{aligned}
B^{pure}(\boldsymbol{\ell}) &= \frac{i}{2\ell^2}\int d\mathbf{x}\left[(Q(\mathbf{x})(g(\mathbf{x})-f(\mathbf{x}))+iU(\mathbf{x})(f(\mathbf{x})+g(\mathbf{x}))e^{-i\boldsymbol{\ell}\mathbf{x}}\right] \\
&= \frac{1}{\ell^2}\int d\mathbf{x}Q(\mathbf{x})\left[(2\partial_x\partial_y W(\mathbf{x})-2i\ell_y\partial_x W(\mathbf{x})-2i\ell_x\partial_y W(\mathbf{x})-2\ell_x\ell_y W(\mathbf{x})\right]e^{-i\boldsymbol{\ell}\mathbf{x}} \\
&- \frac{1}{\ell^2}\int d\mathbf{x}U(\mathbf{x})\left[(\partial_x^2-\partial_y^2)W(\mathbf{x})+(\ell_y^2-\ell_x^2)W(\mathbf{x})-2i\ell_x\partial_x W(\mathbf{x})+2i\ell_y\partial_y W(\mathbf{x})\right]e^{-i\boldsymbol{\ell}\mathbf{x}} \\
&= \frac{2}{\ell^2}\int d^2x W(\mathbf{x})P^{ab}(\mathbf{x})\mathcal{B}_{ab}(e^{-i\boldsymbol{\ell}\mathbf{x}}) \\
&+ \frac{1}{\ell^2}\int d^2x\left[2Q\partial_x\partial_y W+U(\partial_y^2-\partial_x^2)W\right]e^{-i\boldsymbol{\ell}\mathbf{x}} \\
&- \frac{2i}{\ell}\int d^2x\left[Q(\mathbf{x})(\partial_y W\cos\phi_{\boldsymbol{\ell}}+\partial_x W\sin\phi_{\boldsymbol{\ell}})+U(\mathbf{x})(\partial_y W\sin\phi_{\boldsymbol{\ell}}-\partial_x W\cos\phi_{\boldsymbol{\ell}})\right]e^{-i\boldsymbol{\ell}\mathbf{x}} \\
&= \frac{2}{\ell^2}\int d^2x P^{ab}(\mathbf{x})\mathcal{B}_{ab}(W(\mathbf{x})e^{-i\boldsymbol{\ell}\mathbf{x}})
\end{aligned}
$$

This proves the equivalence between the two definitions of the pure B modes.

Chapter 5

The Atacama Cosmology Telescope: CMB Polarization at $200 < \ell < 9000$

5.1 Introduction

This Chapter is the Atacama Cosmology Telescope (ACT) collaboration's first step in measuring CMB polarization and is organized as follows. Section 5.2 describe the observations and data reduction. In Section 5.3 we present our power spectra measurements and interpretation, and conclude in Section 5.4. For power spectra, we use the *Planck* notation: $\mathcal{D}_\ell^{\rm XY} = \ell(\ell+1)C_\ell^{\rm XY}/2\pi$ where XY $\in$ TT, TE, TB, EE, EB, BB. We do not consider circular polarization (e.g., Alexander et al., 2009; Cooray et al., 2003). The maps are made in J2000 equatorial coordinates. We adopt the HEALPIX (Górski et al., 2005) convention for Stokes parameters Q and U. Polarization position angles respect the IAU convention (see, e.g., Hamaker & Bregman, 1996), increasing from North towards East, and thus are computed as $\gamma_p = (1/2)\arg(Q - iU)$. We note that these are the same conventions adopted by *Planck* (see, e.g., Section 2.1 of Ade et al., 2014a), although *Planck* uses Galactic coordinates.

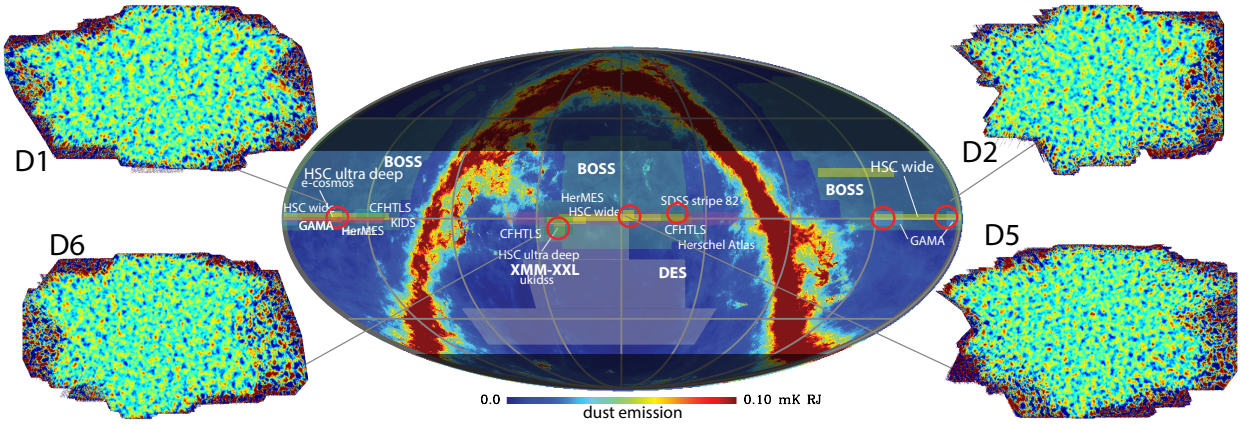

Figure 5.1: ACTPol maps and overlapping surveys. The maps have been filtered to emphasize $\ell > 300$. The power spectra are obtained with only the high S/N region of each map. Going from left to right across the equator, the red circles indicate patches D1, D6, D5, D4, D3, D2 (the first ACTPol season focused on D1, D2, D5, and D6). More than half the sky, as indicated by the light colored area, is accessible to ACTPol. Overlapping surveys include SDSS (SDSS, 2014), BOSS(BOSS, 2014), CFHTLS (Erben et al., 2013), XMM-XXL (XMM-XXL, 2014), Herschel (HerMES & HeLMS, Oliver et al. (2012); Viero et al. (2014)), HSC (Subaru, 2014), DES (DES, 2014), GAMA (Driver et al., 2009), and KiDS (de Jong et al., 2013).

5.2 The observations and data reduction

5.2.1 Sky coverage and scan strategy

ACTPol data are acquired by scanning the telescope in azimuth at a variety of different elevations. A patch is scanned as it rises in the east and then again as it sets in the west. In this first year, we concentrated on four “deep fields" approximately centered on the celestial equator at right ascensions 150°, 175°, 355° and 35° which we call D1 ($73\,\mathrm{deg}^2$), D2 ($70\,\mathrm{deg}^2$), D5 ($70\,\mathrm{deg}^2$), D6 ($63\,\mathrm{deg}^2$) respectively. The areas refer to the deep, rectangular regions with even coverage in the center of each patch that we use for power spectrum analysis. These patches were chosen for their overlap with other surveys and are shown in Figure 5.1. The separation of the patches is such that only one is visible at any given time, and in a typical 24 hour period all four patches were observed in sequence unless the observation would require the telecope to point within five degrees of the Sun. With our scan strategy, each patch is observed in a range of different parallactic angles while scanning horizontally. This is important for separating instrumental from celestial polarization and is a benefit of observing from a non-polar site.

The CMB fields are observed by scanning at 1.5°/s in azimuth, turning around in 1 s, scanning back to the original position, turning around in 1 s and repeating. The duration of the scan depends on elevation; a full cycle takes 16.4 s at an elevation of 35° and 20.9 s at 60°. This is done for 60 scans, or roughly 10 minutes, to form a time-ordered-data or "TOD" packet. The elevation is sometimes changed between 10 minute scans, at which point the detector bias is modulated to recalibrate and check for any changes in the time constants due to the change in sky load.

Data for the maps in Figure 5.1 were taken from Sept. 11, 2013 to Dec. 14, 2013. During this time, in addition to observing the CMB, we performed a number of systematic checks, characterized the instrument, observed planets, and observed the Crab Nebula (Tau A). The net amount of time that went into the maps was 236, 178, 311, and 305 hours for D1, D2, D5, D6 respectively. This represents 24%, 16%, 29% and 31% of the total CMB observation time. However, we use only the lowest noise regions of the maps, which consitute around 70% of the total observing time. This results in a white noise map sensitivity, in the sense of Figure 2 in Das et al. (2013), of 16.2, 17, 13.2, and 11.2 μK-arcmin respectively. For Stokes Q or U sensitivities these numbers should be multiplied by $\sqrt{2}$.

We divide the data into "day" (11:00-24:00 UTC) and "night" (0:00-11:00 UTC). The nighttime data fraction for patches D1, D2, D5 and D6 is 50%, 25%, 76% and 94% respectively. For this analysis we use only the nighttime data from D1, D5, and D6, amounting to 63% of the total.

5.2.2 Beam, pointing, and polarization reconstruction

We have found that multiple observations of planets (Hincks et al., 2010; Hasselfield et al., 2013) are essential for determining the beam profile. In 2013 Uranus was observed 120 times and analyzed as in Hasselfield et al. (2013). With all detectors combined, regardless of polarization, the beam is slightly elliptical with FWHM of 1.36′ (1.26′) along the major (minor) axis. The solid angle is $\Omega_B = 194 \pm 6$ nsr ($2.29 \pm 0.07\,\mathrm{arcmin}^2$), before any smearing due to pointing. These results agree up to $\ell = 5000$ with a similar analysis of 20 observations of Saturn, a much brighter source. We did not detect any significant deviations when the data were split by the elevation of observation or whether the source was rising or setting. A simple telescope pointing model is constrained using observations

of planets at night. This model allows the pointing to be reconstructed with an rms error of $14''$. The impact of pointing variance on the full season CMB maps is handled as in Hasselfield et al. (2013), leading to effective beams in the CMB maps with solid angle $\Omega_B = 224 \pm 20\,\mathrm{nsr}$ for D1, $\Omega_B = 234 \pm 14\,\mathrm{nsr}$ for D5, and $\Omega_B = 224 \pm 12\,\mathrm{nsr}$ for D6. The uncertainties include both beam and pointing contributions.

Average pointing error in the full season maps is assessed by comparing point source positions to the FIRST catalog (Becker et al., 1995; White et al., 1997). The absolute pointing error rms is found to be $5''$ in the nighttime maps, with no significant deviations when the data are split by elevation or time of observation. A $7''$ offset in the absolute pointing is uncorrected in this analysis.

During the day, the heat from the Sun distorts the telescope structure. The distortion pattern is repeatable, although we currently cut data between 17:00 and 20:00 UTC (13:00 and 16:00 local time) when the distortion is greatest. The distortion leads to two effects: the first is a pointing offset and the second is a repeatable deformation of the reflector, which changes the shape of the beam. Both of these effects lead to a roll-off in ℓ that resembles a low pass filter and can be treated as a beam effect in the likelihood. We do not include the daytime data in our cosmological parameter analysis, as models for the daytime beam response are still in development. Nevertheless, our preliminary treatment of the daytime beam produces power spectra that are consistent with nighttime spectra (Figure 5.4) and pass null tests (see §5.3.1).

CMB temperature fluctuation measurements from *Planck* and *WMAP* are used to calibrate the ACTPol T, Q, and U maps with a common rescaling factor, as described in §5.3. However, signal in the Q and U maps will be attenuated by an additional factor α_{P}, which is different from one due primarily to errors in the assumed detector polarization angles. For the present analysis we take $\alpha_{\mathrm{P}} = 0.95 \pm 0.05$.

Any mean offset between the assumed and actual detector polarization angles must be understood in order to properly decompose polarized intensity into E and B components. The polarized CMB may be used to assess the offset angle under the assumption that the intrinsic correlation between the E and B signals is zero. Systematic optical effects associated with polarization, including parallactic rotations, cause a leakage from E to B modes and induce spurious signal in EB and TB

correlations (e.g., Shimon et al. 2008). The most likely instrument polarization reference angle may thus be determined by minimizing the inferred EB signal with respect to offset angle (e.g., Keating et al. 2013). Under these assumptions, the ACTPol E and B spectra from $500 < \ell < 2000$ constrain the instrumental polarization offset angle to be $\delta\gamma_p = -0.2^\circ \pm 0.5^\circ$. This result is referred to as the EB-nulling offset angle. Since this angle is small and consistent with zero, we do not correct the spectra for this effect in the present analysis. The agreement with zero suggests that the optical modeling procedure is free of systematic errors at the 0.5° level or better.

Naturally, the calibration of the polarization offset angle by assuming E and B to be uncorrelated eliminates sensitivity to models, such as isotropic cosmic birefringence, where the distinguishing characteristic is a constant EB cross-correlation. As an alternative calibration approach, measurements of the polarized signal from a bright astrophysical source may be compared to values from the literature. The Crab Nebula is a convenient source for this purpose.

5.2.3 Map making

The time-ordered data are projected on the sky by solving the maximum-likelihood map making equation for a vector of map pixels $\mathbf{m}$,

$$A^T N^{-1} A\mathbf{m} = A^T N^{-1}\mathbf{d}, \tag{5.1}$$

via the preconditioned[1] Conjugate Gradients algorithm. Here $\mathbf{d}$ is the set of time-ordered data, N is the noise covariance of $\mathbf{d}$ and A is the generalized pointing matrix that projects from map domain to time domain. This follows the method used in Dünner et al. (2013), but extends it to polarization. Polarization is handled by including each detector's response to the I, Q and U Stokes parameters in the pointing matrix, so the analysis does not depend on explicit detector pair differencing.

With our current data set, each 70 deg^2 map is a reduction of $\sim 10^{11}$ samples into $\sim 10^6$ pixels, making this the most computationally intensive step in the analysis. Nevertheless, due to the short observation time so far, the costs are still relatively modest compared to the original ACT analysis.

[1] We currently use a simple binned preconditoner, with a simple 3x3 matrix at each (I, Q, U) map pixel that inverts the (polarized) hit-count map. We are investigating other approaches such as a stationary correlation preconditioner (Næss & Louis, 2013).

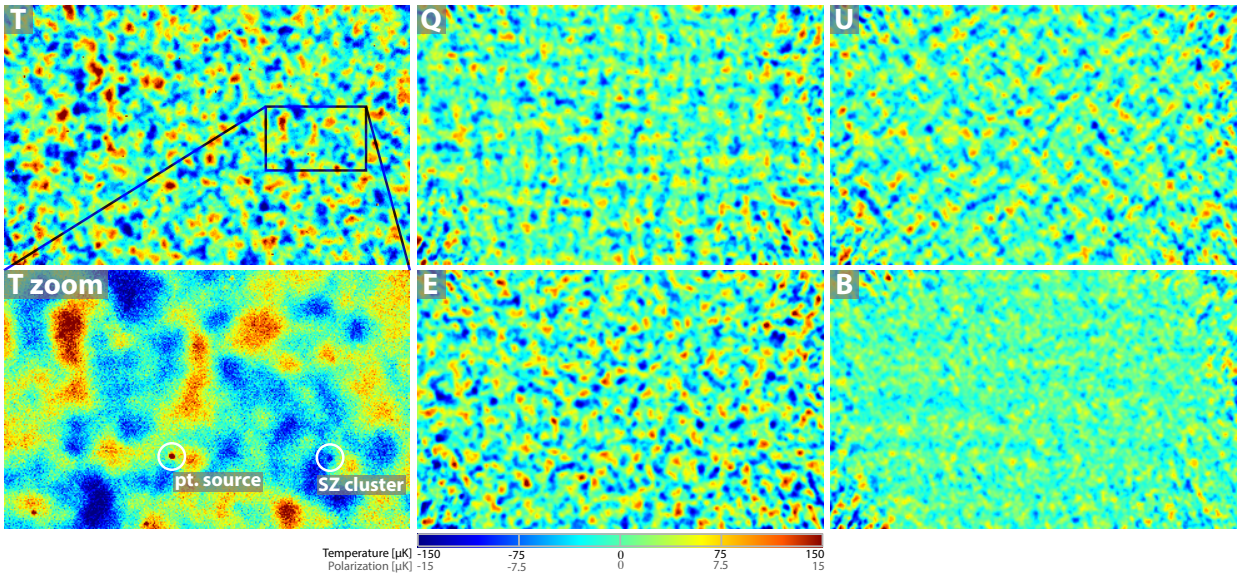

Figure 5.2: Example maps from the region $29.65° < \mathrm{RA} < 40.49°$ (horizontal), $-7.60° < \mathrm{Dec} < -0.68°$ (vertical), in the center of patch D6. Panels 1,2,3,5,6 (left to right, top to bottom) show T, Q, U, E and B respectively. Panel 4 is a zoom on a $2.79° \times 1.73°$ subregion of the T map, showing the full map resolution. The maps have been bandpass filtered to maximize signal-to-noise ($240 < \ell$ for temperature, $260 < \ell < 1370$ for polarization). The visible patterns in the Q and U maps are consistent with a sky dominated by E-mode polarization, as can be seen in the derived E and B maps. The B map is consistent with noise except for a faint $m = 0$ (constant declination) ground residual (see §5.2.4). We do not use $m = 0$ modes in the power spectrum estimation. See Figure 5.3 for an illustration of the noise properties in these filtered maps. The circled galaxy cluster candidate, ACT-CL J0205.2-0439, is within $2'$ of a CFHTLS cluster candidate with photometric redshift $z = 1.1$ (Durret et al., 2011) and three concordant galaxies with spectroscopic $z = 0.97$ found in the VIMOS Public Extragalactic Survey (Garilli et al., 2014). The circled point source may be associated with FBQS J0209-0438, a quasar at $z = 1.128$ (Véron-Cetty & Véron, 2006).

Figure 5.2 shows an example map from patch D6. For display purposes, a bandpass filter has been applied to maximize signal-to-noise. Example difference maps (odd vs. even pairs of nights) for the same region are shown in Figure 5.3.

5.2.4 Ground pickup

ACT has two levels of ground screens. One screen is fixed to the telescope and scans with it. This entire system sits inside a second 13 m high fixed ground screen. Nevertheless, we still detect a spurious signal which we interpret as ground pickup. When the telescope points to the northeast between azimuths $\sim 25° - 85°$ we observe a spurious signal with a $\sim 30°$ period in azimuth, with little

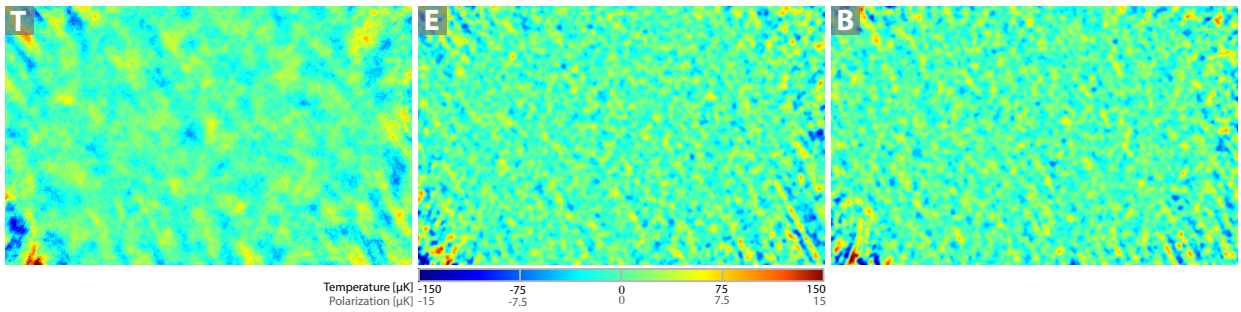

Figure 5.3: Difference maps (odd vs. even pairs of nights) for the same region as Figure 5.2, illustrating the noise properties of the map. Correlated noise is visible as diagonal stripes aligned with our dominant scanning directions (diagonally in these coordinates). These are the map-space equivalent of the correlated noise in the time-ordered data. Noise correlations are taken into account in the noise model in the power spectrum estimation.

elevation dependence, and a peak-to-peak amplitude of $\sim 200\mu$K in Q and U. This is consistent with signal from the nearby mountain Cerro Toco being diffracted over the top of the ground screen's 30° wide panels. While this signal is washed out when projected on the sky, it would still be a contaminant of $\pm 20\mu$K or more in our polarization maps if ignored.

The ground signal can be disentangled from the sky because it is constant in azimuth during a scan and does not rotate with parallactic angle like the sky. The exceptions are modes on the sky that depend only on declination, not right ascension (such as the spherical harmonics with $m = 0$). These show up as pure functions of azimuth during a constant elevation scan, and are degenerate with the ground even when observing at multiple azimuths and elevations. We remove both these and the degenerate modes by applying an azimuth filter to the time-ordered data and excluding Fourier modes with $|\ell_y| < 50$ from the power spectrum estimation.[2]

While the filters are effective at suppressing the ground pickup, they also remove some bona fide sky signal, making our maps and power spectra slightly biased. The effects of the filtering are assessed by passing simulated maps of the polarized CMB through the filtering procedure, and comparing the power spectra of the input and output maps. The main effect of the filter is to suppress, slightly, the signal in temperature (polarization) on large angular scales, with a transfer function that decreases from 0.995 (0.99) at $\ell = 500$ to 0.95 (0.9) at $\ell = 200$. Leakage from E to B is also seen, but at a level that is negligible for this analysis.

[2]Excluding $|\ell_y| < 50$ removes an approximately $4\mu\text{K}/^\circ$ residual ground gradient from the azimuth-filtered maps.

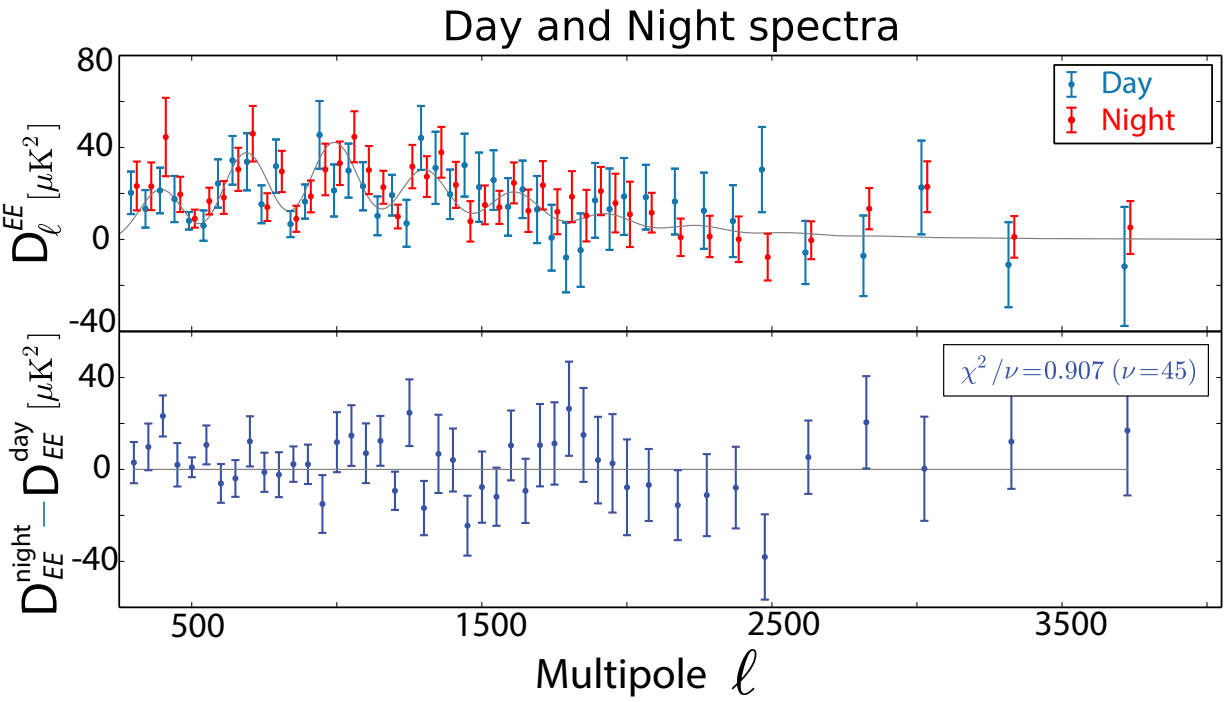

Figure 5.4: The D1 day and nighttime EE spectra (top), and their difference (bottom); they are consistent.

5.3 The power spectra and interpretation

We compute the temperature and polarization power spectra of the maps following the methods described in Chapter 4. The code was checked extensively with simulations and is able to extract an E/B mode power spectrum signal to within 0.1σ in maps with 5 μK noise in the presence of uneven weights across the maps, irregular boundaries, and cutouts for sources.

In this analysis we use $\ell_{\rm min}^{\rm TT} = 500, \ell_{\rm min}^{\rm TE,EE} = 250$, and $\ell_{\rm max}^{\rm TT,TE,EE} = 9\,000$.[3] In two-dimensional Fourier space we mask a vertical strip with $|\ell_x| < 90$ (as in Das et al., 2011a; Das et al., 2013), and a horizontal strip with $|\ell_y| < 50$, as described in §5.2.4. The maps are calibrated to the *Planck* 143 GHz temperature map (Planck Collaboration I, 2013) following the method in Chapter 3, resulting in a 2% uncertainty. The overall calibration measured by *Planck* and *WMAP* disagree (Planck Collaboration XVI, 2013), so we then multiply all maps by a factor of 1.012 to correspond to the more mature *WMAP* calibration.

[3]We use a larger value of ℓ_{min} for TT because atmosphere $1/f$ modes impact the T maps much more than polarization maps.

We test the parameter extraction and power spectrum pipeline as follows. We generate a simulated[4] sky in temperature and polarization with the WMAP9+ACT parameter set (Calabrese et al., 2013) and realistic level of unresolved point source power, extract the portion corresponding to the ACTPol coverage for each patch, and add a realization of the full inhomogeneous noise model as measured. We then take the power spectra of the maps, and from the power spectra derive cosmological parameters, marginalizing over foreground parameters. We run this process 100 times and recover the input cosmology to within 0.1σ. We use the simulations to construct the covariance matrix for the data.

In this analysis we do not account for cosmic aberration (Jeong et al., 2014), super sample lensing (Manzotti et al., 2014), or the effect of the flat-sky approximation. We have simulated these sub-dominant effects and find that they have a negligible impact on derived ΛCDM cosmological parameters; however, we are extending our pipeline to account for them in future ACTPol analysis.

5.3.1 Null tests

We perform a set of null tests similar to those done for the ACT temperature analysis (Chapter 2): compare the data with and without telescope turnaround periods incorporated, compare the results from different detector sets, and compare the maps made from the four different time-splits.

For the detector null, we split the array in half by those most likely to have a different calibration and polarization response, and make two split maps for each subset. We form the difference map between detector sets for each split and then compute their cross-spectrum. For the turnaround null we test for effects generated by the acceleration of the telescope. As in Das et al. (2013) we make four split maps with the turnaround data removed, cutting 12-13% of the data, and form a set of difference maps between splits with and without turnarounds. We apply these tests to the D5 and D6 patches, which have the deepest coverage.

We have also compared the daytime and nighttime spectra for the D1 patch, and find them to be consistent (see Figure 5.4). The null tests are summarized in Table 5.1, and Table 5.2 shows the other permutations of the null spectra for the turnaround excision and split nulls.

[4]To include the effects of our flat-sky approximationin our simulations, each simulated map is generated on the full, curved sky and then projected to our native cylindrical equal-area maps.

Table 5.1: Null tests

Test	Patch	Spectrumă	χ^2/dof	P.T.E
Detector	D5	TT	0.92	0.65
		EE	1.51	0.01
		TE	0.65	0.98
	D6	TT	1.39	0.03
		EE	0.91	0.66
		TE	1.02	0.43
Turnaround[1]	D5	TT	0.76	0.91
		EE	0.71	0.95
		TE	0.86	0.76
	D6	TT	0.92	0.65
		EE	1.18	0.17
		TE	0.76	0.91
Splits[1]	D5	TT	0.67	0.97
		EE	0.72	0.94
		TE	0.55	0.997
	D6	TT	0.94	0.60
		EE	0.77	0.89
		TE	0.77	0.89
	D1	TT	1.60	0.003
		EE	0.77	0.89
		TE	1.14	0.23
Patches	D1-D5	TT	0.89	0.70
		EE	0.89	0.70
		TE	1.24	0.11
	D1-D6	TT	0.67	0.97
		EE	0.66	0.97
		TE	1.26	0.09
	D5-D6	TT	0.94	0.60
		EE	0.94	0.60
		TE	0.96	0.56
Day-Night	$D1^N$-$D1^D$	EE	0.91	0.64

Table 5.2: Split and turnaround nulls

Patch	Combination	Spec.	χ^2/dof Splits	P.T.E	χ^2/dof Turn.[1]	P.T.E
D5	$(s_0 - s_2) \times$	TT	0.65	0.98	0.64	0.98
	$(s_1 - s_3)$	EE	0.88	0.72	0.86	0.77
		TE	0.77	0.90	0.76	0.90
	$(s_0 - s_3) \times$	TT	1.08	0.31	1.09	0.31
	$(s_1 - s_2)$	EE	0.92	0.64	0.95	0.58
		TE	1.21	0.14	1.34	0.05
D6	$(s_0 - s_2) \times$	TT	0.93	0.61	1.17	0.19
	$(s_1 - s_3)$	EE	0.60	0.99	0.75	0.92
		TE	0.72	0.94	0.79	0.87
	$(s_0 - s_3) \times$	TT	0.96	0.55	1.06	0.36
	$(s_1 - s_2)$	EE	0.74	0.92	1.06	0.35
		TE	0.91	0.67	1.01	0.46
D1	$(s_0 - s_2) \times$	TT	0.68	0.97		
	$(s_1 - s_3)$	EE	0.89	0.71		
		TE	1.16	0.20		
	$(s_0 - s_3) \times$	TT	0.92	0.65		
	$(s_1 - s_2)$	EE	0.69	0.96		
		TE	1.30	0.06		

An assessment of the consistency of the χ^2 and PTE statistics is complicated by the fact that the many tests probe the same noise realization and are thus correlated. For independent measurements, the distribution of PTE values should be consistent with a uniform distribution. Our distribution of PTE values is somewhat skewed towards values greater than 0.5. However there is no systematic failure of the χ^2 test in these results, and the most extreme values of 0.003 and 0.997 are not statistically surprising for a sample of this size. The lowest PTE is for a D1 TT split null (0.003), and the highest for a D5 TE split null (0.997), but the other permutations of these null spectra, shown in Table 5.2, do not show outlier behavior.

The different patches have different coverage, are observed at different times, have different (but low) levels of potential Galactic contamination, and are observed differently relative to the local environment. For the analysis of many systematic effects, they are effectively independent measurements, so the spectra can be compared as an additional test. Figure 5.5 shows the combined power

spectra from the three patches. For the spectra where a signal is detected (TT, TE, EE) we have subtracted the WMAP9+ACT best-fit model (reproduced from Calabrese et al., 2013, Table 5.3) and show the residuals. For reference we show the small difference between the WMAP9+ACT model and the Planck+WP+highL model for TT, TE and EE. For TB, EB, and BB we just show the data. The measured BB signal is consistent with zero as expected with the current ACTPol sensitivity. We find that the spectra are consistent among patches, with the χ^2 of their differences given in Table 5.1 for TT, TE, and EE.

5.3.2 Foreground emission

We test for foreground emission in the temperature maps by correlating the ACTPol maps with the FDS dust template map (Finkbeiner et al., 1999). The dust level in this template has been shown to be consistent with the *Planck* 353 GHz maps (Abergel et al., 2013) at the 30% level. The predicted contribution of dust to the temperature anisotropy power spectrum is measurable but small, less than 2 μK^2 at $\ell = 2000$ as shown in Figure 5.6. We do not correct for it in the maps or likelihood at this stage.

Based on the recent results from *Planck* (Ade et al., 2014a), the polarization fraction in D1, D5, and D6 is roughly 5%. We take 10% as an upper limit and thus the contribution from polarized dust emission to the power spectrum is expected to be less than 0.02 μK^2 at $\ell = 2000$. The contribution from polarized synchrotron emission is expected to be at this level or smaller. A full analysis must await the public release of the *Planck* polarization maps. However, the consistency shown in Table 5.1 between patches D1, D5, and D6, each with different foreground levels, suggests that any possible contribution is small compared to the cosmological polarization signal.

5.3.3 TT, TE, EE

Figure 5.7 shows the combined ACTPol TT and EE spectra along with independent data sets from ACT temperature measurements and *Planck*. The full TT/TE/EE set is shown in Figure 5.8. The TE spectrum is shown experiments. The bandpowers are not significantly correlated, and bandpower window functions are computed as in Das et al. (2013) to compare theory models

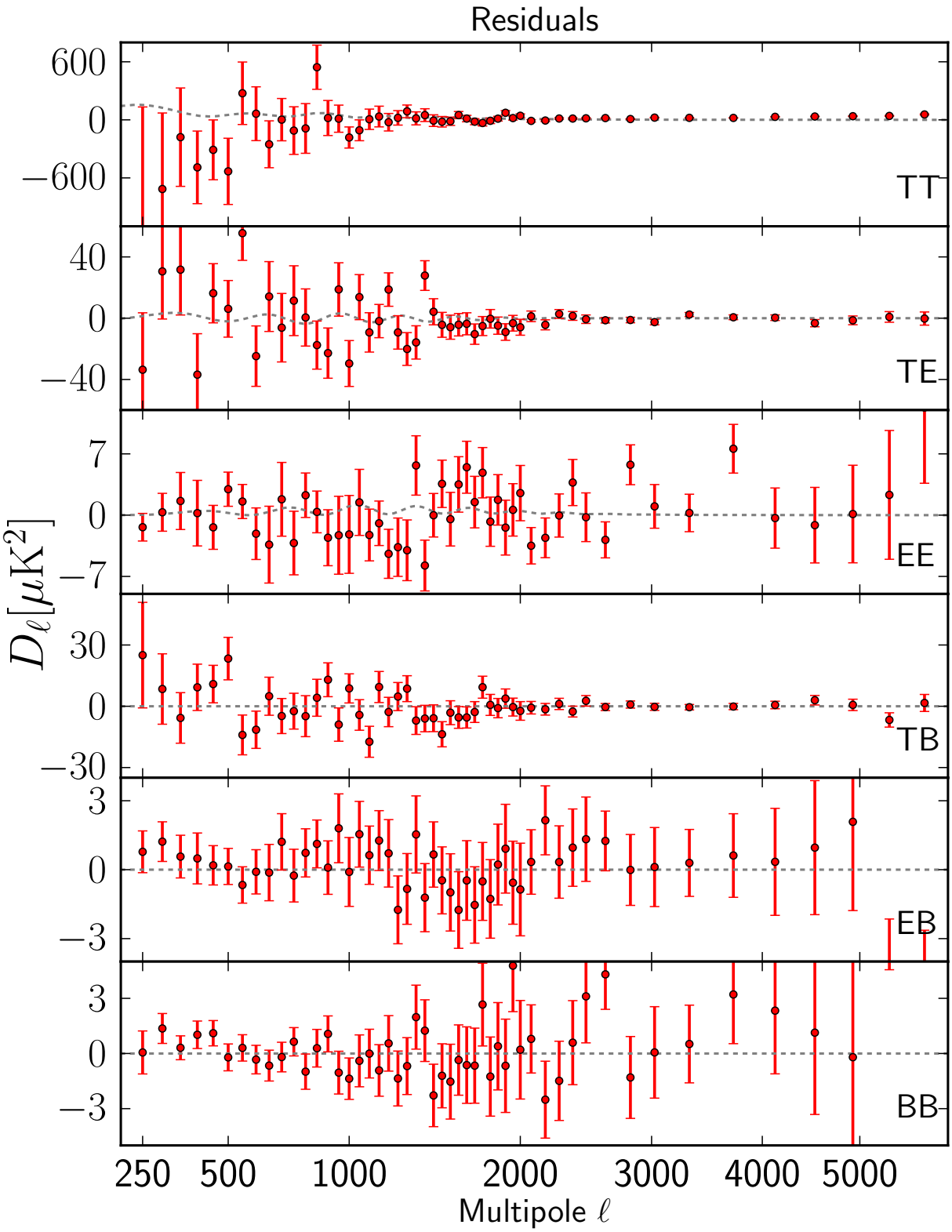

Figure 5.5: Residuals of measured power spectra relative to the WMAP9+ACT best-fit model (for which TB, EB, and BB are assumed to be zero). Dashed curve shows the small difference between the WMAP9+ACT and Planck+WP+highL best-fit models. The x-axis is scaled as $\ell^{0.5}$.

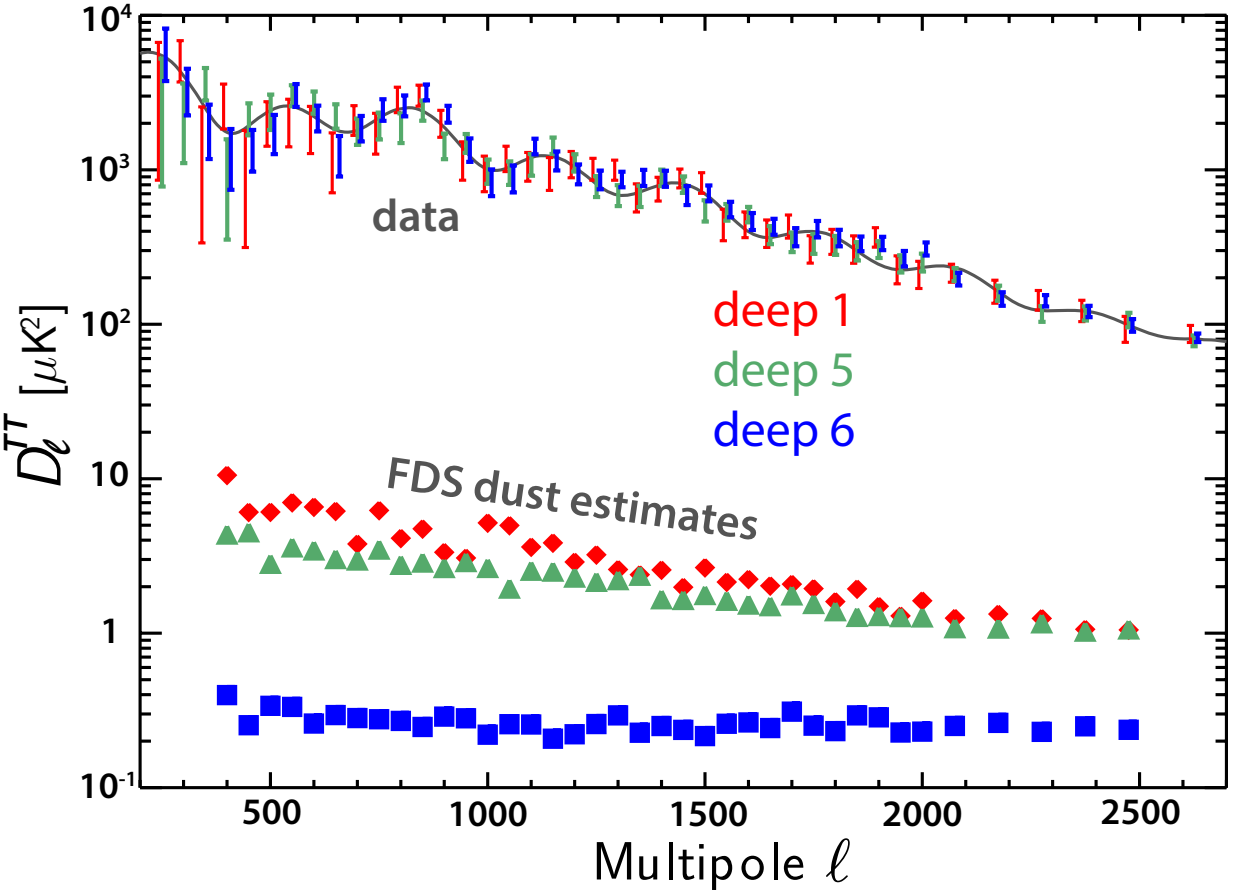

Figure 5.6: The expected temperature power spectrum of thermal dust in the ACTPol patches, estimated using the Finkbeiner et al. (1999, FDS) template, plotted below the ACTPol temperature power spectra. The dust amplitude is $\leq 2\ \mu\mathrm{K}^2$ at $\ell = 2000$ ($\sim 1\%$ of the TT spectrum amplitude, or 10% in the maps). We show that the FDS template is a good tracer of the sub-dominant dust component by correlating it with the ACTPol maps, finding a cross-correlation consistent with unity to within 1σ.

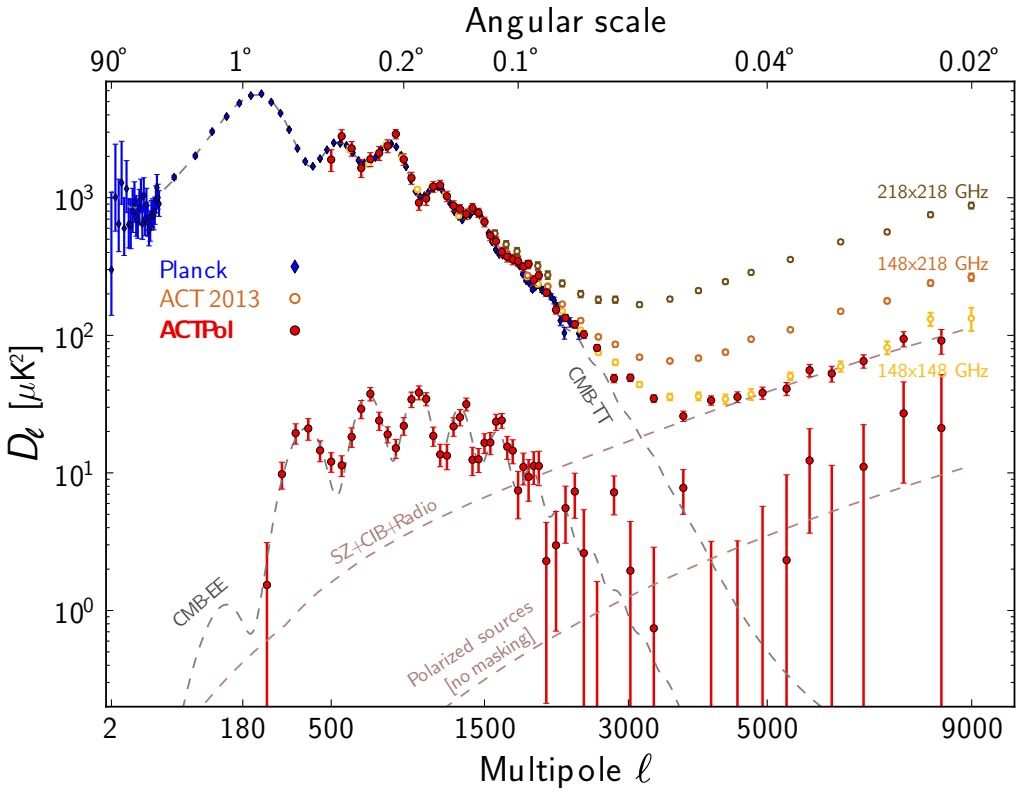

Figure 5.7: The *Planck*, ACT, and ACTPol data. Many *Planck* points for TT are obscured by the ACT data for $1000 < \ell < 2500$. The model spectra labeled CMB-TT and CMB-EE are for 'Planck+WP+highL' (Planck Collaboration XVI, 2013). It is clear that the same model is an excellent fit to the TT and EE data (see §5.3.3). Recently *WMAP* (Bennett et al., 2012) and SPT (Story et al., 2012) have also published new data on the TT spectrum in this range, which are not shown here. All measurements are broadly consistent. The best-fitting Poisson polarized source level is shown, with no sources masked. A non-zero level is preferred, but the distribution is consistent with zero at 95% confidence, with $a_p^{\rm pol} < 2.4$. The x-axis is scaled as $\ell^{0.45}$ to emphasize the mid-ℓ range.

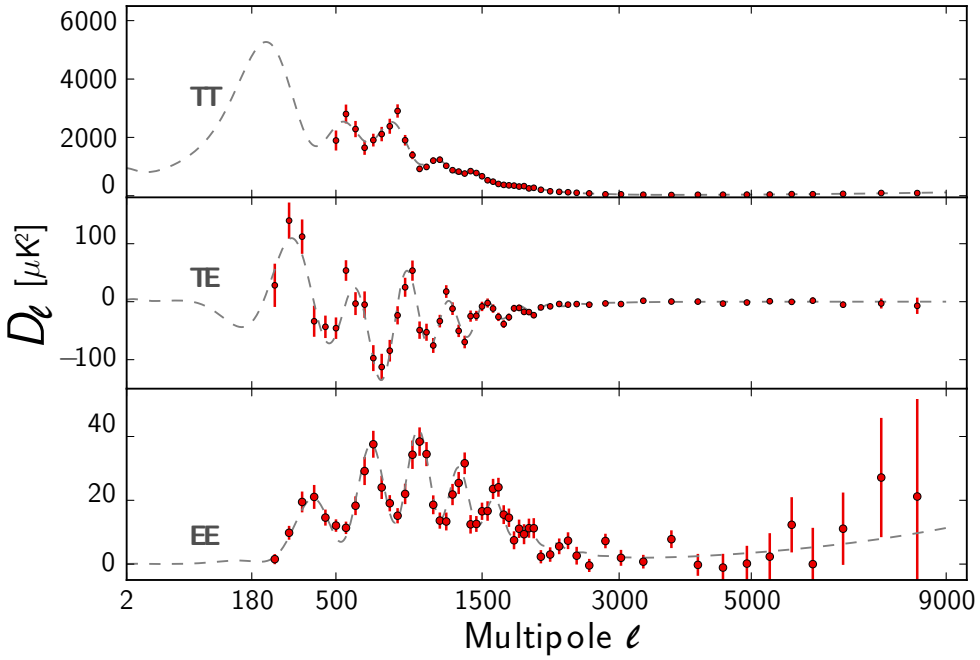

Figure 5.8: The ACTPol TT, TE, and EE power spectra, together with the best-fitting ΛCDM cosmological model and foreground components. Six acoustic peaks are seen in the E-mode polarization, out of phase with the temperature peaks and with the TE correlation pattern predicted by the standard model.

to these data. We observe six acoustic peaks in the EE power spectrum, out of phase with the TT spectrum as expected in the standard cosmological model, and six peak/troughs in the TE cross-correlation.

As a simple test, we find the χ^2 for the ACTPol EE data compared to the ΛCDM 6-parameter model using a) the WMAP9+ACT parameters (Calabrese et al., 2013), and b) the *Planck* best-fit parameters (Planck Collaboration XVI, 2013). The reduced χ^2 values for the two models are 1.09 and 1.12 respectively with 55 dof and no free parameters (with PTE of 0.30 and 0.25). For the TE data the reduced χ^2 for the two models are 1.26 and 1.24, again with 55 dof and no free parameters (PTE of 0.09 and 0.18).

ΛCDM

Another test of the standard ΛCDM cosmological model is to fit its parameters from just the ACTPol EE and TE data. In this combination, WMAP9 is used to put a prior on the optical depth

Table 5.3: Comparison of cosmological Parameters and 68% confidence intervals for different data sets.

	WMAP9+ACT[1]	Planck[2]	ACTPol TE,EE[3]
$100\Omega_b h^2$	2.247 ± 0.041	2.207 ± 0.027	2.073 ± 0.135
$\Omega_c h^2$	0.1143 ± 0.0044	0.1198 ± 0.0026	0.131 ± 0.015
$10^4\theta_A$	103.95 ± 0.19	104.132 ± 0.063	104.12 ± 0.31
$\ln(10^{10}A_s)$	3.191 ± 0.041	3.090 ± 0.025	3.140 ± 0.085
n_s	0.970 ± 0.011	0.9585 ± 0.0070	$[0.970 \pm 0.011]$
τ	0.089 ± 0.013	0.091 ± 0.0135	$[0.089 \pm 0.013]$
Derived[4]			
σ_8	0.830 ± 0.021	0.828 ± 0.012	0.933 ± 0.064
H_0	69.7 ± 2.0	67.3 ± 1.2	63.2 ± 5.5

and scalar spectral index, since ACTPol does not measure the largest angular scales. We estimate parameters using standard methods as in Sievers et al. (2013) and Calabrese et al. (2013), and marginalize over Poisson source powers for the TE and EE spectra. Other foregrounds are assumed to be unpolarized.

The results are reported in Table 5.3 and shown in Figure 5.9 for the physical baryon density, $\Omega_b h^2$, the physical cold dark matter density, $\Omega_c h^2$, the acoustic scale θ_A, and the amplitude of primordial curvature perturbations, A_s, defined at pivot scale $k_0 = 0.05$ Mpc^{-1}. The polarization data are in excellent agreement with the standard model constrained by the *Planck* temperature data (Planck Collaboration XVI, 2013). With only three months of data and a single detector array, the ΛCDM constraints of ACTPol are not competitive with the ones of *Planck*. We expect the future seasons of ACTPol (2014 with two detectors arrays, 2015 with three detectors arrays) to improve these constraints. The accurate mapping of the damping tail will also significantly improve constraints on extensions to the ΛCDM model.

We repeat the same test with just the ACTPol TT data, including the foreground model as in Dunkley et al. (2013) to account for Poisson and clustered point sources and the thermal and kinematic Sunyaev-Zel'dovich effects. The parameters are consistent with the ACTPol TE/EE results, but more weakly constrain the acoustic scale and the physical baryon and CDM densities (see Figure 5.9). This highlights the potential of the E-mode polarization signal for cosmological constraints (see e.g., Galli et al., 2014), with sharper acoustic features and less contamination from atmosphere and foregrounds. At this stage of measurement, however, the polarization data are

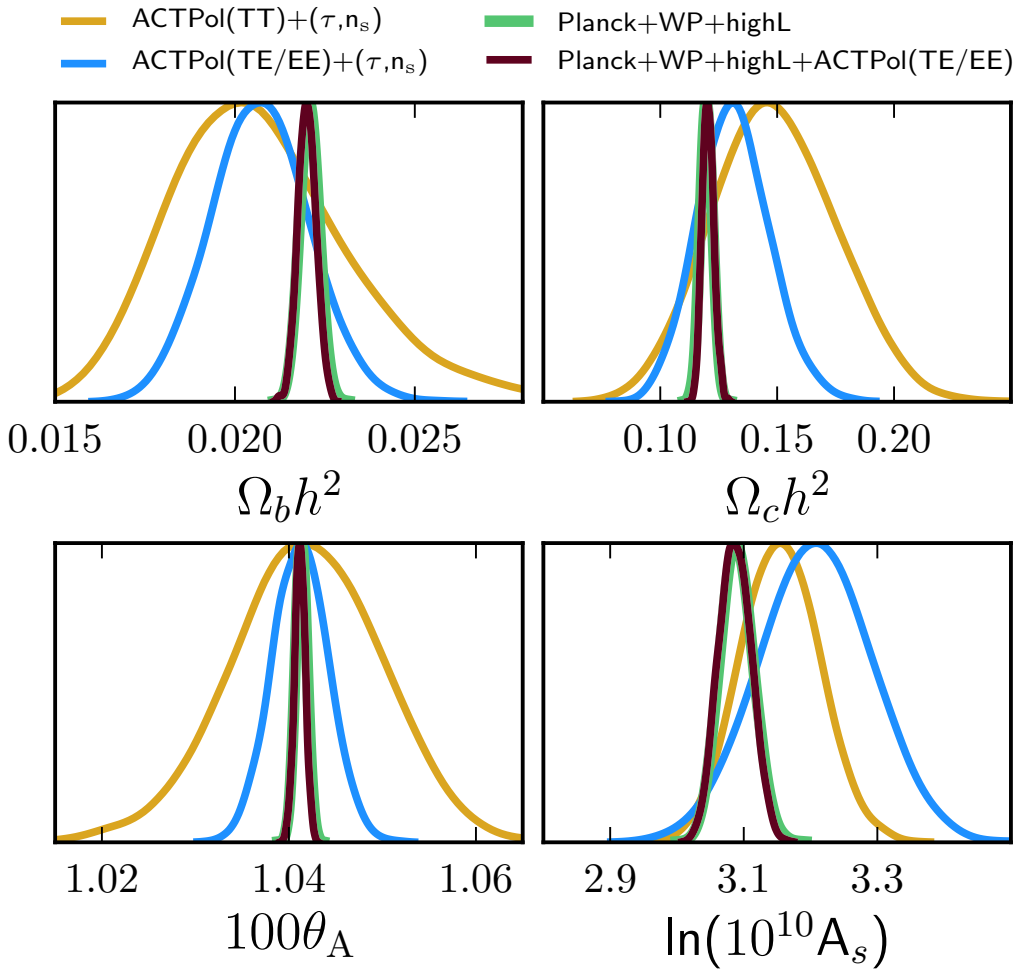

Figure 5.9: ΛCDM parameters estimated from the ACTPol TE and EE data alone(with a prior on the optical depth and spectral index from *WMAP*), and ACTPol TT alone. They are compared to the constraints from *Planck* temperature data, and combined *Planck* and ACTPol TE and EE. The temperature and polarization data give consistent results.

not as precise as the *Planck* or *WMAP* temperature data primarily because they are taken over a relatively small region of sky. Parameter constraints from ACTPol combined with *Planck* are currently dominated by the temperature data.

Polarized point sources

We do not detect significantly polarized point sources in the ACTPol maps. Six of the highest signal-to-noise sources found in the D5 and D6 patches are shown in Figure 5.10; the polarization

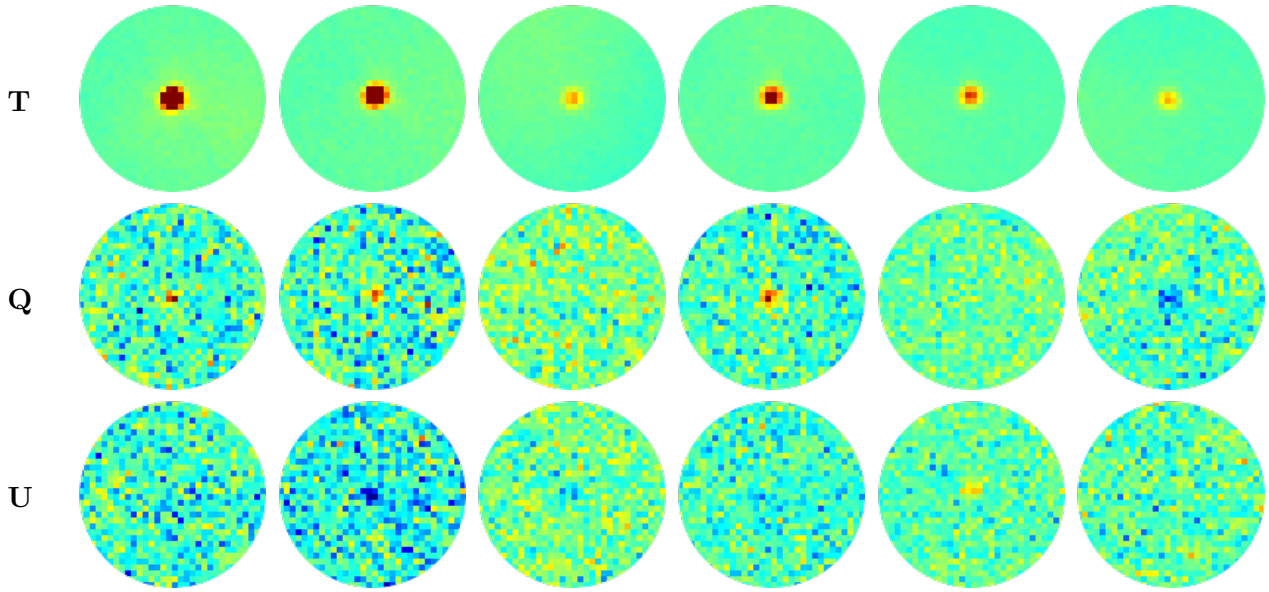

Figure 5.10: Three of the highest signal-to-noise polarized point sources from each of patch D5 (left) and D6 (right). Each disk has a radius of 8', with the value range being $\pm 2000\mu$K for T and $\pm 200\mu$K for Q and U. We do not mask polarized sources in this analysis. The sources may be associated with (from left to right) [HB89] 2332-017, [HB89] 2335-027, SDSS J001130.40+005751.7, PKS 0214-085, [HB89] 0226-038 and PKS 0205-010.

is barely detectable. For the temperature spectra, point sources above 15 mJy are masked, but no sources exceed this threshold in polarization and none are masked.

We model the Poisson tail of the temperature spectrum as

$$\mathcal{D}_\ell = (a_s + a_d)\left(\frac{\ell}{3000}\right)^2 \mu\mathrm{K}^2 \tag{5.2}$$

(Dunkley et al., 2011), where a_s is the amplitude for the residual unmasked radio/synchrotron sources and a_d is the amplitude for the pervasive dusty star forming galaxy (DSFG) or CIB component. The latter is unresolved. The two components are separated in ACT temperature measurements with two observing frequencies. In ACTPol we currently have just one frequency and so place a limit on the combined Poisson power: $a_p = a_s + a_d$. In Sievers et al. (2013) we found $a_s = 3.1 \pm 0.4$, $a_d = 7.0 \pm 0.5$, for a total of $a_p = 10.3 \pm 0.6$ for the TT data. With the ACTPol TT data we find a consistent level of $a_p = 10.9 \pm 1.5$, for the same masking threshold.

Without masking any point sources in the EE data we find $a_p^{\mathrm{pol}} = 1.5 \pm 0.6$ at 68% confidence,

or $a_p^{\rm pol} < 2.4$ at 95% confidence. In flux units this corresponds to $C_\ell = 0.15^{+0.05}_{-0.07}$ Jy^2/sr, or < 0.24 Jy^2/sr (95% CL), at 146 GHz, and puts a limit on all polarized sources before masking.

5.4 Conclusions

The polarization capabilities of ACTPol have already enabled new probes of the cosmological model. We have shown that ACT is capable of measuring polarization to high accuracy and of measuring CMB temperature and polarization during the day. With one third of the full complement of detectors observing at night over just 90 days, we have already made some of the most competitive measurements yet of CMB polarization at $\ell > 1000$. The ACTPol EE, TE, TB, and BB data obtained to date are all in agreement with the standard model of cosmology. We anticipate substantial improvements with more detectors and observing time.

Chapter 6

Conclusion

The CMB temperature power spectrum has been an invaluable source of cosmological information in the last decade. The recent measurement by the *Planck* satellite at low and intermediate ℓ combined with those of ACT and SPT at high ℓ provide a nearly complete picture of the physics of temperature anisotropies on the last scattering surface. A lot of progress in the field has been achieved during the course of this DPhil. As an example, the constraint on the number of relativistic degrees of freedom was $N_{\rm eff} = 5.3 \pm 1.3$ in 2010 (Dunkley et al. 2011); three years later it is now measured to be $N_{\rm eff} = 3.28 \pm 0.4$ by WMAP+ACT+SPT[1] (Calabrese et al. 2013). This new level of precision requires very careful analysis, because small systematics can easily be at the level of our statistical uncertainty. For this thesis, I have developed and extensively tested the power spectrum estimation pipeline for the ACT experiment (Chapter 2 and Chapter 3). I have carried out numerous tests on the maps, in order to characterize the astrophysical and instrumental contamination to the cosmological signal. The precise measurement of the CMB damping tail from the ACT experiment has been used to get new competitive constraints on extensions to the ΛCDM model. Combined with the *Planck* data, the high-resolution measurement helps to break degeneracies between the different foreground parameters[2].

The estimation of the lensing field and its power spectrum is challenging, and the lensing analysis pipeline is tested and calibrated on simulations. This has motivated the development of a fast

[1] also $N_{\rm eff} = 3.3 \pm 0.27$ by *Planck* (Planck Collaboration XVI 2013).
[2] The ones poorly constrained by *Planck* data alone.

algorithm to generate lensed simulations of the high resolution CMB sky (Chapter 4). The potential of the lensing power spectrum to precisely constrain the growth of structure at low and intermediate redshifts is yet to be used. But the 4σ detection of the ACT collaboration was already enough to rule out Universe without a cosmological constant using only CMB data (Sherwin et al. 2011). The lensing field can also be correlated with other probes of the underlying matter distribution such as galaxy count surveys or galaxy lensing surveys (Sherwin et al. 2012; Hand et al. 2013). The CMB and galaxy surveys are sensitive to different sources of instrumental systematics and astrophysical contaminations, so adding the cross correlation information is the cleanest way to extract cosmological signal.

The EE and TE power spectrum measured from ACTPol discussed in Chapter 5 is the first attempt to map the polarization of the CMB on small angular scales. Due to the low level of polarized foreground emission, an accurate measurement of the E mode damping tail will provide valuable cosmological information in the next couple of years. ACTPol, Polarbear, SPTPol, the Keck Array and their extensions are also now targeting an accurate measurement of primordial and lensed B modes. Multi frequency observations from these experiments will soon be available, allowing us to disentangle cosmological, dust, and synchrotron signals. In Chapter 4 we have presented tools to recover a nearly optimal B mode power spectrum on an incomplete sky. Using the pure B mode formalism will be of increasing importance in the future, as the experimental noise will go down. The flat sky formalism for pure B modes estimation developed in this thesis provides an important speed up compared to the full sky formalism, and can be useful for experiments targeting a small region of the sky.

High resolution and low noise CMB experiments are also useful to reveal cluster properties. The tSZ effect offers the best method for assembling a catalog of clusters at high redshift, which could be used for understanding the time evolution of both baryonic and dark matter. An accurate mapping of the kSZ effect could be of great importance as it traces the large scale velocity field of our universe over a wide range of redshift. The kinetic Sunyaev-Zel'dovich has the same frequency scaling as the primordial CMB, so multifrequency observation cannot be used alone to disentangle the two signals. But a high signal-to-noise measurement of the E modes can be used to predict the

T mode power spectrum at the last scattering surface (using their correlation $C_\ell^{TE} \neq 0$), allowing for a direct measurement of the kSZ power spectrum (Calabrese et al. 2014).

What is the future of CMB data analysis? An enormous amount of data will soon become available and will require developing new analysis tools. Without trying to be exhaustive here are some interesting challenges:

1. **Speeding up the mapmaking**: at the moment, the mapmaking equation is solved using a preconditioned conjugate gradient method, it is the most time consuming step in the data analysis pipeline. One way to speed it up is to design a good preconditioner using our knowledge of the noise properties of a given experiment (see for example: Næss & Louis 2013). Another way would be to give up on the preconditioned conjugate gradient method and instead use a multi grid method. It has been shown to be extremely efficient for a related problem: generating constrained realizations of the CMB sky (Seljebotn et al. 2014), but hasn't been successfully used for mapmaking yet.

2. **Characterizing and correcting the effect of the flat sky approximation**: ground based experiments observe only a fraction of the sky. The spherical harmonics are clearly not a good set of basis functions for an experiment observing 500 square degrees. However using the flat sky approximation could introduce a small source of errors. One way of correcting it would be to model the flat sky approximation as the effect due to a large scale deterministic lens, and to correct for it at the power spectrum level.

3. **Gibbs sampling for components separation**: the microwave sky gets contributions from a lot of different sources. In order to isolate one, for example for determining the properties of a given cluster, we need to properly marginalized over the others (primordial CMB, foregrounds). Gibbs sampling offers an interesting framework for sampling the joint probability distribution of all the component of the microwave sky. A public code exist for Gibbs sampling over the full sky (Eriksen et al. 2008), but it is computationally too expensive to be used at high resolution. We are currently developing a Gibbs sampler using the flat sky approximation, which is fast even at very high resolution. The potential of such a code is fantastic, as we could use it for example to compute the B mode power spectrum of one of the ACTPol patches

while marginalizing over the polarized dust emission constrained by the *Planck* 353 GHz map projected over the same patch of the sky.

Bibliography

Abazajian, K. N., Calabrese, E., Cooray, A., De Bernardis, F., Dodelson, S. et al., 2011. Cosmological and astrophysical neutrino mass measurements. *Astroparticle Physics*, **35**, 177–184.

Abergel, A., Ade, P. A. R., Aghanim, N., Alina, D., Alves, M. I. R., Aniano, G., Armitage-Caplan, C., Arnaud, M., Ashdown, M. & et al., 2013. Planck 2013 results. XI. All-sky model of thermal dust emission.

Addison, G. E., Dunkley, J., Hajian, A., Viero, M., Bond, J. R. et al., 2012. Power-Law Template for IR Point Source Clustering. *Astrophys.J.*, **752**, 120.

Addison, G. E., Dunkley, J. & Spergel, D. N., 2012. Modelling the correlation between the thermal Sunyaev Zel'dovich effect and the cosmic infrared background. *MNRAS*, **427**, 1741–1754.

Ade, P. A. R., Aghanim, N., Alina, D., Alves, M. I. R., Armitage-Caplan, C., Arnaud, M., Arzoumanian, D., Ashdown, M., Atrio-Barandela, F. & et al., 2014a. Planck intermediate results. XIX. An overview of the polarized thermal emission from Galactic dust.

Ade, P. A. R., Akiba, Y., Anthony, A. E., Arnold, K., Atlas, M. et al., 2014b. A Measurement of the Cosmic Microwave Background B-Mode Polarization Power Spectrum at Sub-Degree Scales with Polarbear.

Ade, P. A. R., Akiba, Y., Anthony, A. E., Arnold, K., Barron, D. et al., 2013. Gravitational Lensing of Cosmic Microwave Background Polarization.

Alexander, S., Ochoa, J. & Kosowsky, A., 2009. Generation of circular polarization of the cosmic microwave background. *PRD*, **79**(6), 063524.

Austermann, J., Aird, K., Beall, J., Becker, D., Bender, A. et al., 2012. SPTpol: an instrument for CMB polarization measurements with the South Pole Telescope. *Proc.SPIE Int.Soc.Opt.Eng.*, **8452**, 84520E.

Battaglia, N., Bond, J. R., Pfrommer, C. & Sievers, J. L., 2012. On the Cluster Physics of Sunyaev-Zel'dovich and X-Ray Surveys. II. Deconstructing the Thermal SZ Power Spectrum. *ApJ*, **758**, 75.

Becker, R. H., White, R. L. & Helfand, D. J., 1995. The FIRST Survey: Faint Images of the Radio Sky at Twenty Centimeters. *ApJ*, **450**, 559.

Bennett, C., Larson, D., Weiland, J., Jarosik, N., Hinshaw, G. et al., 2012. Nine-Year Wilkinson Microwave Anisotropy Probe (WMAP) Observations: Final Maps and Results. *arXiv. 1212.5225*.

Benoit-Levy, A., Smith, K. M. & Hu, W., 2012. Non-Gaussian structure of the lensed CMB power spectra covariance matrix. *Phys.Rev.*, **D86**, 123008.

BICEP2 Collaboration I, 2014. BICEP2 I: Detection Of B-mode Polarization at Degree Angular Scales.

Bond, J., Jaffe, A. H. & Knox, L., 1998. Estimating the power spectrum of the cosmic microwave background. *Phys.Rev.*, **D57**, 2117–2137.

BOSS, 2014. Baryon Oscillation Spectroscopic Survey. *http://www.sdss3.org/surveys/boss.php*.

Bowyer, J., Jaffe, A. H. & Novikov, D. I., 2011. MasQU: Finite Differences on Masked Irregular Stokes Q,U Grids. Astrophysics Source Code Library.

Bracco, A., Cooray, A., Veneziani, M., Amblard, A., Serra, P. et al., 2011. Herschel-ATLAS: statistical properties of Galactic cirrus in the GAMA-9 Hour Science Demonstration Phase Field. *MNRAS*, **412**, 1151–1161.

Bunn, E. F., 2011. Efficient decomposition of cosmic microwave background polarization maps into pure E, pure B, and ambiguous components. *PRD*, **83**(8), 083003.

Calabrese, E., Hložek, R., Battaglia, N., Bond, J. R., de Bernardis, F. et al., 2014. Precision Epoch of Reionization studies with next-generation CMB experiments. *ArXiv e-prints*.

Calabrese, E., Hlozek, R. A., Battaglia, N., Battistelli, E. S., Bond, J. R. et al., 2013. Cosmological parameters from pre-planck cosmic microwave background measurements. *PRD*, **87**(10), 103012.

Cao, L. & Fang, L.-Z., 2009. A Wavelet-Galerkin Algorithm of the E/B Decomposition of Cosmic Microwave Background Polarization Maps. *Astrophys.J*, **706**, 1545–1555.

Cooray, A., Melchiorri, A. & Silk, J., 2003. Is the cosmic microwave background circularly polarized? *Physics Letters B*, **554**, 1–6.

Das, S., Hajian, A. & Spergel, D. N., 2009. Efficient Power Spectrum Estimation for High Resolution CMB Maps. *Phys.Rev.*, **D79**, 083008.

Das, S., Louis, T., Nolta, M. R., Addison, G. E., Battistelli, E. S. et al., 2013. The Atacama Cosmology Telescope: Temperature and Gravitational Lensing Power Spectrum Measurements from Three Seasons of Data. *arXiv. 1301.1037*.

Das, S., Marriage, T. A., Ade, P. A. R., Aguirre, P., Amiri, M. et al., 2011a. The Atacama Cosmology Telescope: A Measurement of the Cosmic Microwave Background Power Spectrum at 148 and 218 GHz from the 2008 Southern Survey. *ApJ*, **729**, 62–+.

Das, S., Sherwin, B. D., Aguirre, P., Appel, J. W., Bond, J. R. et al., 2011b. Detection of the Power Spectrum of Cosmic Microwave Background Lensing by the Atacama Cosmology Telescope. *Physical Review Letters*, **107**(2), 021301.

de Jong, J. T. A., Verdoes Kleijn, G. A., Kuijken, K. H. & Valentijn, E. A., 2013. The Kilo-Degree Survey. *Experimental Astronomy*, **35**, 25–44.

DES, 2014. Dark Energy Survey. *https://www.darkenergysurvey.org/index.shtml*.

Dodelson, S., 2003. Modern Cosmology. URL `http://books.google.fr/books?id=3oPRxdXJexcC`.

Driver, S. P., Norberg, P., Baldry, I. K., Bamford, S. P., Hopkins, A. M. et al., 2009. GAMA: towards a physical understanding of galaxy formation. *Astronomy and Geophysics*, **50**(5), 050000–5.

Dunkley, J., Calabrese, E., Sievers, J., Addison, G. E., Battaglia, N. et al., 2013. The Atacama Cosmology Telescope: likelihood for small-scale CMB data. *JCAP*, **7**, 25.

Dunkley, J., Hlozek, R., Sievers, J., Acquaviva, V., Ade, P. A. R. et al., 2011. The Atacama Cosmology Telescope: Cosmological Parameters from the 2008 Power Spectrum. *ApJ*, **739**, 52.

Dünner, R., Hasselfield, M., Marriage, T. A., Sievers, J., Acquaviva, V. et al., 2013. The Atacama Cosmology Telescope: Data Characterization and Mapmaking. *ApJ*, **762**, 10.

Durret, F., Adami, C., Cappi, A., Maurogordato, S., Márquez, I. et al., 2011. Galaxy cluster searches based on photometric redshifts in the four CFHTLS Wide fields. *A&A*, **535**, A65.

Erben, T., Hildebrandt, H., Miller, L., van Waerbeke, L., Heymans, C. et al., 2013. CFHTLenS: the Canada-France-Hawaii Telescope Lensing Survey - imaging data and catalogue products. *MNRAS*, **433**, 2545–2563.

Eriksen, H., Jewell, J., Dickinson, C., Banday, A., Gorski, K. et al., 2008. Joint Bayesian component separation and CMB power spectrum estimation. *Astrophys.J.*, **676**, 10–32.

Finkbeiner, D. P., Davis, M. & Schlegel, D. J., 1999. Extrapolation of Galactic Dust Emission at 100 Microns to Cosmic Microwave Background Radiation Frequencies Using FIRAS. *ApJ*, **524**, 867–886.

Flauger, R., Hill, J. C. & Spergel, D. N., 2014. Toward an Understanding of Foreground Emission in the BICEP2 Region. *ArXiv e-prints*.

Fowler, J. W., Acquaviva, V., Ade, P. A. R., Aguirre, P., Amiri, M. et al., 2010. The Atacama Cosmology Telescope: A Measurement of the 600< ell < 8000 Cosmic Microwave Background Power Spectrum at 148 GHz. *ApJ*, **722**, 1148–1161.

Galli, S., Benabed, K., Bouchet, F., Cardoso, J.-F., Elsner, F., Hivon, E., Mangilli, A., Prunet, S. & Wandelt, B., 2014. CMB Polarization can constrain cosmology better than CMB temperature.

Garilli, B., Guzzo, L., Scodeggio, M., Bolzonella, M., Abbas, U. et al., 2014. The VIMOS Public Extragalactic Survey (VIPERS). First Data Release of 57 204 spectroscopic measurements. *A&A*, **562**, A23.

Górski, K. M., Hivon, E., Banday, A. J., Wandelt, B. D., Hansen, F. K., Reinecke, M. & Bartelmann, M., 2005. HEALPix: A Framework for High-Resolution Discretization and Fast Analysis of Data Distributed on the Sphere. *ApJ*, **622**, 759–771.

Grain, J., Tristram, M. & Stompor, R., 2009. Polarized CMB power spectrum estimation using the pure pseudo-cross-spectrum approach. *PRD*, **79**(12), 123515.

Grain, J., Tristram, M. & Stompor, R., 2012. CMB EB and TB cross-spectrum estimation via pseudospectrum techniques. *PRD*, **86**(7), 076005.

Hajian, A., Acquaviva, V., Ade, P. A., Aguirre, P., Amiri, M. et al., 2011. The Atacama Cosmology Telescope: Calibration with WMAP Using Cross-Correlations. *Astrophys.J.*, **740**, 86.

Hajian, A., Viero, M. P., Addison, G., Aguirre, P., Appel, J. W. et al., 2012. Correlations in the (Sub)millimeter Background from ACTxBLAST. *ApJ*, **744**, 40.

Hamaker, J. P. & Bregman, J. D., 1996. Understanding radio polarimetry. III. Interpreting the IAU/IEEE definitions of the Stokes parameters. *aaps*, **117**, 161–165.

Hand, N., Leauthaud, A., Das, S., Sherwin, B. D., Addison, G. E. et al., 2013. First Measurement of the Cross-Correlation of CMB Lensing and Galaxy Lensing. *ArXiv e-prints*.

Hasselfield, M., Moodley, K., Bond, J. R., Das, S., Devlin, M. J. et al., 2013. The Atacama Cosmology Telescope: Beam Measurements and the Microwave Brightness Temperatures of Uranus and Saturn. *The Astrophysical Journal Supplement Series*, **209**(1), 17. URL `http://stacks.iop.org/0067-0049/209/i=1/a=17`.

Hincks, A. D., Acquaviva, V., Ade, P. A. R., Aguirre, P., Amiri, M. et al., 2010. The Atacama Cosmology Telescope (ACT): Beam Profiles and First SZ Cluster Maps. *ApJS*, **191**, 423–438.

Hinshaw, G. et al., 2013. Nine-Year Wilkinson Microwave Anisotropy Probe (WMAP) Observations: Cosmological Parameter Results. *Astrophys.J.Suppl.*, **208**, 19.

Hu, W. & Dodelson, S., 2002. Cosmic Microwave Background Anisotropies. *ARA&A*, **40**, 171–216.

Hu, W., Sugiyama, N. & Silk, J., 1996. The Physics of Microwave Background Anisotropies. *ArXiv Astrophysics e-prints*.

Hu, W. & White, M., 1997a. A CMB polarization primer. *New Astronomy*, **2**, 323–344.

Hu, W. & White, M., 1997b. The Damping Tail of Cosmic Microwave Background Anisotropies. *ApJ*, **479**, 568–579.

Iliev, I. T., Pen, U.-L., Richard Bond, J., Mellema, G. & Shapiro, P. R., 2006. kSZ from patchy reionization: The view from the simulations. *New Astronomy Reviews*, **50**, 909–917.

Jarosik, N., Bennett, C. L., Dunkley, J., Gold, B., Greason, M. R. et al., 2011. Seven-year Wilkinson Microwave Anisotropy Probe (WMAP) Observations: Sky Maps, Systematic Errors, and Basic Results. *ApJS*, **192**, 14.

Jeong, D., Chluba, J., Dai, L., Kamionkowski, M. & Wang, X., 2014. Effect of aberration on partial-sky measurements of the cosmic microwave background temperature power spectrum. *PRD*, **89**(2), 023003.

Jungman, G., Kamionkowski, M., Kosowsky, A. & Spergel, D. N., 1996. Cosmological-parameter determination with microwave background maps. *PRD*, **54**, 1332–1344.

Kamionkowski, M., Kosowsky, A. & Stebbins, A., 1997. Statistics of cosmic microwave background polarization. *Phys.Rev.*, **D55**, 7368–7388.

Keating, B. G., Shimon, M. & Yadav, A. P. S., 2013. Self-calibration of Cosmic Microwave Background Polarization Experiments. *ApJ*, **762**, L23.

Keisler, R., Reichardt, C. L., Aird, K. A., Benson, B. A., Bleem, L. E. et al., 2011. A Measurement of the Damping Tail of the Cosmic Microwave Background Power Spectrum with the South Pole Telescope. *ApJ*, **743**, 28.

Kermish, Z., Ade, P., Anthony, A., Arnold, K., Arnold, K. et al., 2012. The POLARBEAR Experiment. *arXiv. 1210.7768.*.

Komatsu, E. & Seljak, U., 2002. The Sunyaev-Zel'dovich angular power spectrum as a probe of cosmological parameters. *MNRAS*, **336**, 1256–1270.

Kovac, J. M., Leitch, E. M., Pryke, C., Carlstrom, J. E., Halverson, N. W. & Holzapfel, W. L., 2002. Detection of polarization in the cosmic microwave background using DASI. *Nature*, **420**, 772–787.

Larson, D., Dunkley, J., Hinshaw, G., Komatsu, E., Nolta, M. R. et al., 2011. Seven-year Wilkinson Microwave Anisotropy Probe (WMAP) Observations: Power Spectra and WMAP-derived Parameters. *ApJS*, **192**, 16–+.

Lesgourgues, J., 2006. Inflationary Cosmology. URL `http://books.google.fr/books?id=6EXtSAAACAAJ`.

Lesgourgues, J., 2011. The Cosmic Linear Anisotropy Solving System (CLASS) I: Overview. *ArXiv e-prints*.

Lesgourgues, J. & Pastor, S., 2006. Massive neutrinos and cosmology. *Physics Reports*, **429**, 307–379.

Lewis, A., 2005. Lensed CMB simulation and parameter estimation. *Phys.Rev.*, **D71**, 083008.

Lewis, A. & Challinor, A., 2006. Weak gravitational lensing of the CMB. *Physics Reports*, **429**, 1–65.

Lewis, A., Challinor, A. & Lasenby, A., 2000. Efficient Computation of Cosmic Microwave Background Anisotropies in Closed Friedmann-Robertson-Walker Models. *ApJ*, **538**, 473–476.

Lewis, A., Challinor, A. & Turok, N., 2002. Analysis of CMB polarization on an incomplete sky. *PRD*, **65**(2), 023505.

Linde, A. D., 1982. A new inflationary universe scenario: A possible solution of the horizon, flatness, homogeneity, isotropy and primordial monopole problems. *Physics Letters B*, **108**, 389–393.

Louis, T., Addison, G. E., Hasselfield, M., Bond, J., Calabrese, E. et al., 2014. The Atacama Cosmology Telescope: Cross Correlation with Planck maps.

Manzotti, A., Hu, W. & Benoit-Lévy, A., 2014. Super-Sample CMB Lensing.

Marriage, T. A., Baptiste Juin, J., Lin, Y.-T., Marsden, D., Nolta, M. R. et al., 2011. The Atacama Cosmology Telescope: Extragalactic Sources at 148 GHz in the 2008 Survey. *ApJ*, **731**, 100.

Mather, J. C., Cheng, E. S., Cottingham, D. A., Eplee, Jr., R. E., Fixsen, D. J. et al., 1994. Measurement of the cosmic microwave background spectrum by the COBE FIRAS instrument. *ApJ*, **420**, 439–444.

Miville-Deschênes, M.-A. & Lagache, G., 2005. IRIS: A New Generation of IRAS Maps. *ApJS*, **157**, 302–323.

Miville-Deschênes, M.-A., Martin, P. G., Abergel, A., Bernard, J.-P., Boulanger, F. et al., 2010. Herschel-SPIRE observations of the Polaris flare: Structure of the diffuse interstellar medium at the sub-parsec scale. *A&A*, **518**, L104.

Mortonson, M. J. & Seljak, U., 2014. A joint analysis of Planck and BICEP2 B modes including dust polarization uncertainty. *ArXiv e-prints*.

Næss, S. & Louis, T., 2013. A fast map-making preconditioner for regular scanning patterns.

Næss, S. K. & Louis, T., 2013. Lensing simulations by Taylor expansion – not so inefficient after all. *arXiv. 1307.0719*.

Niemack, M., Ade, P., Aguirre, J., Barrientos, F., Beall, J. et al., 2010. ACTPol: A polarization-sensitive receiver for the Atacama Cosmology Telescope. *Proc.SPIE Int.Soc.Opt.Eng.*, **7741**, 77411S.

Oliver, S. J., Bock, J., Altieri, B., Amblard, A., Arumugam, V. et al., 2012. The Herschel Multi-tiered Extragalactic Survey: HerMES. *MNRAS*, **424**, 1614–1635.

Penzias, A. A. & Wilson, R. W., 1965. A Measurement of Excess Antenna Temperature at 4080 Mc/s. *ApJ*, **142**, 419–421.

Planck Collaboration, Ade, P. A. R., Aghanim, N., Arnaud, M., Ashdown, M., Aumont, J., Baccigalupi, C., Balbi, A., Banday, A. J., Barreiro, R. B. & et al., 2011. Planck early results. XIX. All-sky temperature and dust optical depth from Planck and IRAS. Constraints on the "dark gas" in our Galaxy. *A&A*, **536**, A19.

Planck Collaboration I, 2013. Planck 2013 results. I. Overview of products and scientific results. *arXiv. 1303.5062.*.

Planck Collaboration IX, 2013. Planck 2013 results. IX. HFI spectral response. *arXiv. 1303.5070*.

Planck Collaboration VII, 2013. Planck 2013 results. VII. HFI time response and beams. *arXiv. 1303.5068*.

Planck Collaboration VIII, 2013. Planck 2013 results. VIII. HFI photometric calibration and mapmaking. *arXiv. 1303.5069.*.

Planck Collaboration XI, 2013. Planck 2013 results. XI. All-sky model of thermal dust emission. *arXiv. 1312.1300*.

Planck Collaboration XVI, 2013. Planck 2013 results. XVI. Cosmological parameters. *arXiv. 1303.5076*.

Planck Collaboration XVII, 2013. Planck 2013 results. XVII. Gravitational lensing by large-scale structure. *Arxiv e-prints*.

Planck Collaboration XXIV, 2013. Planck 2013 Results. XXIV. Constraints on primordial non-Gaussianity. *ArXiv e-prints*.

Planck Collaboration XXX, 2013. Planck 2013 results. XXX. Cosmic infrared background measurements and implications for star formation. *arXiv. 1309.0382*.

Sachs, R. K. & Wolfe, A. M., 1967. Perturbations of a Cosmological Model and Angular Variations of the Microwave Background. *ApJ*, **147**, 73.

SDSS, 2014. Sloan Digital Sky Survey. *http://www.sdss.org*.

Seljak, U. & Zaldarriaga, M., 1996. A Line-of-Sight Integration Approach to Cosmic Microwave Background Anisotropies. *ApJ*, **469**, 437.

Seljebotn, D. S., Mardal, K.-A., Jewell, J. B., Eriksen, H. K. & Bull, P., 2014. A Multi-level Solver for Gaussian Constrained Cosmic Microwave Background Realizations. *ApJS*, **210**, 24.

Sherwin, B. D., Das, S., Hajian, A., Addison, G., Bond, J. R. et al., 2012. The Atacama Cosmology Telescope: Cross-correlation of cosmic microwave background lensing and quasars. *PRD*, **86**(8), 083006.

Sherwin, B. D., Dunkley, J., Das, S., Appel, J. W., Bond, J. R. et al., 2011. Evidence for Dark Energy from the Cosmic Microwave Background Alone Using the Atacama Cosmology Telescope Lensing Measurements. *Physical Review Letters*, **107**(2), 021302.

Shimon, M., Keating, B., Ponthieu, N. & Hivon, E., 2008. CMB polarization systematics due to beam asymmetry: Impact on inflationary science. *PRD*, **77**(8), 083003.

Shirokoff, E., Reichardt, C. L., Shaw, L., Millea, M., Ade, P. A. R. et al., 2011. Improved Constraints on Cosmic Microwave Background Secondary Anisotropies from the Complete 2008 South Pole Telescope Data. *ApJ*, **736**, 61.

Sievers, J. L. et al., 2013. The Atacama Cosmology Telescope: Cosmological parameters from three seasons of data. *JCAP*, **1310**, 060.

Silk, J., 1968. Cosmic Black-Body Radiation and Galaxy Formation. *ApJ*, **151**, 459.

Smith, K. M., 2006. Pseudo-c(l) estimators which do not mix e and b modes. *Phys.Rev.*, **D74**, 083002.

Smith, K. M. & Zaldarriaga, M., 2007. A general solution to the E-B mixing problem. *Phys.Rev.*, **D76**, 043001.

Smoot, G. F., Bennett, C. L., Kogut, A., Wright, E. L., Aymon, J. et al., 1992. Structure in the COBE differential microwave radiometer first-year maps. *ApJ*, **396**, L1–L5.

Story, K., Reichardt, C., Hou, Z., Keisler, R., Aird, K. et al., 2012. A Measurement of the Cosmic Microwave Background Damping Tail from the 2500-square-degree SPT-SZ survey. *arXiv. 1210.7231*.

Subaru, 2014. Subaru's Hyper Suprime-Cam. *http://www.naoj.org/Projects/HSC/*.

Sunyaev, R. A. & Zeldovich, I. B., 1980. Microwave background radiation as a probe of the contemporary structure and history of the universe. *ARA&A*, **18**, 537–560.

Swetz, D., Ade, P., Amiri, M., Appel, J., Battistelli, E. et al., 2011. Overview of the Atacama Cosmology Telescope: Receiver, instrumentation, and telescope systems. *Astrophys.J.Suppl.*, **194**, 41.

Tegmark, M. & de Oliveira-Costa, A., 1998. Removing Point Sources from Cosmic Microwave Background Maps. *ApJ*, **500**, L83.

van Engelen, A., Keisler, R., Zahn, O., Aird, K. A., Benson, B. A. et al., 2012. A Measurement of Gravitational Lensing of the Microwave Background Using South Pole Telescope Data. *ApJ*, **756**, 142.

Véron-Cetty, M.-P. & Véron, P., 2006. A catalogue of quasars and active nuclei: 12th edition. *A&A*, **455**, 773–777.

Viero, M. P., Asboth, V., Roseboom, I. G., Moncelsi, L., Marsden, G. et al., 2014. The Herschel Stripe 82 Survey (HerS): Maps and Early Catalog. *ApJS*, **210**, 22.

White, R. L., Becker, R. H., Helfand, D. J. & Gregg, M. D., 1997. the FIRST Survey (White+ 1997). *VizieR Online Data Catalog*, **8048**, 0.

XMM-XXL, 2014. XXL: The Ultimate XMM Extragalactic Survey. *http://sci.esa.int/xmm-newton/48357-xxl-the-ultimate-xmm-extragalactic-survey/*.

Zhao, W. & Baskaran, D., 2010. Separating E and B types of polarization on an incomplete sky. *PRD*, **82**(2), 023001.